Mesoscale Structure of Precipitation Regions in Northeast Winter Storms

Abstract of a thesis presented to the Faculty

of the University at Albany, State University of New York

in partial fulfillment of the requirements

for the degree of

Master of Science

College of Arts and Sciences

Department of Earth and Atmospheric Sciences

Matthew D. Greenstein

2006

ABSTRACT

While forecasters can predict likely areas of precipitation, problems remain in correctly anticipating mesoscale precipitation patterns within those areas. In northeastern United States snowstorms, precipitation takes on numerous patterns, or modes, in radar reflectivity imagery, e.g., relatively uniform, fractured, and banded. Better forecasts of these mesoscale characteristics would allow for enhanced prediction of snowfall amount and variability and for the differentiation between high-impact and low-impact snows.

Twenty "heavy snow" events in the Northeast from the winters of 2002–03 through 2004–05 are selected for analysis using several criteria based on precipitation type, snowfall, time of year, and location. High-resolution WSI Corporation NOWrad composite reflectivity radar mosaics are used to identify five main precipitation modes, or mesoscale patterns, among the cases. The NCEP North American Regional Reanalysis is used to create plan-view maps and cross sections in order to ascertain which aspects of the ingredients—lift, instability, moisture, and microphysics—can assist in distinguishing the observed precipitation modes.

Ultimately, it is shown that the frontogenesis pattern and conditional instability help to differentiate between the five modes. Some aspects of the frontogenesis pattern that accomplish this goal are its strength, steepness, and whether it is surface-based. Notably absent from a discussion of the distinguishing features is weak moist symmetric stability, which appears to be a favorable condition for heavy snow but is not a precipitation mode-distinguishing parameter. Lastly, conceptual models and a flowchart are developed that a forecaster can use operationally to improve the mesoscale forecast of these heavy snow events.

Mesoscale Structure of Precipitation Regions in Northeast Winter Storms

A thesis presented to the Faculty

of the University at Albany, State University of New York

in partial fulfillment of the requirements

for the degree of

Master of Science

College of Arts and Sciences

Department of Earth and Atmospheric Sciences

Matthew D. Greenstein
2006

ACKNOWLEDGMENTS

Without the help of numerous individuals, this research would never have been completed. First, I need to thank my advisors Lance Bosart and Dan Keyser for the opportunity to conduct research at the University at Albany and for helping me to excel by pushing me to approach research problems in multiple ways. I also want to acknowledge NOAA for financial support through the Collaborative Science and Technology Applied Research (CSTAR) program (Grant # NA04NWS4680005).

I want to thank those who helped me with programming and data issues over the past two years. Department system administrator Kevin Tyle provided much computer support over the course of my research, helping me with GEMPAK and data storage issues. Fellow graduate student Alan Srock needs to be recognized for supplying abundant GEMPAK assistance, including scripts to smooth NARR grids. Postdoctoral fellow Anantha Aiyyer deserves thanks for helping me learn how to write FORTRAN scripts to manipulate GEMPAK data files. Many thanks also go to fellow CSTAR student Keith Wagner for his input into our quasi-daily musings of frontogenesis and weak moist symmetric stability.

Thanks are due to David Ahijevych at NCAR for supplying me with the WSI NOWrad grids that were critical to this research. Also, thanks to Celeste Iovinella, Lynn Hughes, and Sharon Baumgardner for their administrative and secretarial duties at the University that allowed me to present at conferences and get paid every two weeks.

Lastly, I would be remiss without thanking my parents for their support in my meteorological interests over the years, for driving me to the ocean whenever big storms approached the Jersey Shore, and for tolerating my incessant chatter about the weather.

TABLE OF CONTENTS

Abstract ii

Acknowledgments iv

Table of Contents v

List of Tables viii

List of Figures ix

1. Introduction 1

    1.1 General Purpose 1

    1.2 Literature Review 1

        1.2.1 Ingredients-based Methodology 1

        1.2.2 Large-scale Forcing 3

        1.2.3 Instability 4

            1.2.3.1 Definition 4

            1.2.3.2 M_g–θ Relationship 5

            1.2.3.3 EPV Diagnostic 6

            1.2.3.4 Coexistence of CI and CSI 8

            1.2.3.5 The Geostrophic vs. Full Wind Debate 9

        1.2.4 Frontogenetical Forcing and Instability Together with Moisture 10

            1.2.4.1 Moisture 10

            1.2.4.2 Frontogenetical Forcing 11

            1.2.4.3 Frontal Circulations with Stability Considerations 12

            1.2.4.4 Banding 14

        1.2.5 Microphysics 15

        1.2.6 Band vs. No Band 16

            1.2.6.1 Case Studies 16

            1.2.6.2 Statistical Studies 18

        1.2.7 Thesis Concept 18

2. Data and Methodology 25

    2.1 Data 25

        2.1.1 Radar 25

        2.1.2 Reanalyses 25

2.1.3 Data for Case Selection 26
2.2 Methodologies 27
2.2.1 Case Selection 27
2.2.2 Case Classification 27
2.2.3 Radar Classification 29
2.2.4 Plan-view Analysis 30
2.2.5 Cross-section Analysis 32
3. Results 35
3.1 Case Classification 35
3.2 Radar Classification 35
3.2.1 Five Modes 35
3.2.2 Unclassifiable 37
3.3 Plan-view Analysis 39
3.4 Cross-section Analysis 40
3.4.1 Five Modes 40
3.4.1.1 Classic Band 40
3.4.1.2 Uniform 42
3.4.1.3 Transient Band 44
3.4.1.4 Bandlets 45
3.4.1.5 Fractured 48
3.4.2 Solo Light Snowbands 48
4. Discussion 87
4.1 The Modes 87
4.1.1 Classic Band 87
4.1.2 Uniform 88
4.1.3 Transient Band 90
4.1.4 Bandlets 91
4.1.5 Fractured 93
4.1.6 Solo Light Snowbands 93
4.2 Distinguishing and Nondistinguishing Features 94
4.2.1 Distinguishing Features 94

4.2.2 Nondistinguishing Features 95
4.3 EPV* vs. EPV_g^* 97
4.4 Recommendations to the Forecaster 99
5. Conclusions and Future Work 107
5.1 Conclusions 107
5.2 Future Work 110
References 112

LIST OF TABLES

TABLE I. 20 “heavy snow” cases selected using criteria in section 2.2.1.

TABLE II. Modes in each case, along with 3-h times corresponding to the NARR analyses when they are present.

TABLE III. Unclassifiable portions of cases, along with 3-h times corresponding to the NARR analyses when they are present, and brief reasons why they are unclassifiable.

TABLE IV. Solo light snowbands, along with the 3-h times corresponding to the NARR analyses when they are present.

LIST OF FIGURES

Fig. 1.1. Schematics of factors that contribute to heavy snowfall in the Northeast (a) during the initial development of the snowstorm and (b) when the snowstorm is fully developed [From Kocin and Uccellini (2004)].

Fig. 1.2. Schematic vertical cross section illustrating (a) a stable horizontal displacement, (b) a stable vertical displacement, and (c) an unstable slantwise displacement. Solid lines represent absolute momentum of the basic flow. Dashed lines represent equivalent potential temperature. Dashed arrows show the initial displacement and the double-shafted arrows show the resulting accelerations [From Sanders and Bosart (1985)].

Fig. 1.3. Vertical cross section of the idealized transverse circulation associated with large-scale confluence (double-shafted arrows) [From Sanders and Bosart (1985)].

Fig. 1.4. The cross-front circulation in physical space with no variation in symmetric or gravitational stability. The diagonal solid line represents the frontogenesis axis [From Emanuel (1985)].

Fig. 1.5. As in Fig. 1.4 but with reduced potential vorticity on the right (warm) side of the frontogenesis region [From Emanuel (1985)].

Fig. 1.6. Schematic *x–p* cross sections through a characteristic (a) single-banded and (b) nonbanded environment. The following fields are shown: frontogenesis (red shading), saturation equivalent potential temperature (thin solid), and ascent (dashed) with length of arrow relative to the magnitude of ascent and course of air parcel trajectory. Length of cross section approximately 1000 km [From Novak et al. (2004)].

Fig. 1.7. Conceptual model of synoptic and mesoscale flows associated with (a) single-banded and (b) nonbanded events. Features shown are midlevel frontogenesis (red shading), midlevel deformation zone (scalloped) and associated dilatation axes [dashed lines in (a)], midlevel streamlines (black lines), and upper-level jet cores (wide dashed arrows) [From Novak et al. (2004)].

Fig. 1.8. Conceptual model depicting midlevel frontogenesis (green shading), zone of equivalent potential vorticity reduction (pink shading), cloud shield edges (dotted), cold conveyor belt (heavy blue line), warm conveyor belt (heavy orange line), dry tongue jet (heavy gold line), and the surface low (black L). Adapted from Nicosia and Grumm (1999).

Fig. 2.1. Case selection domain; domain is bounded by 36.5°N, 50°N, 65°W, and 85°W.

Fig. 2.2. "Heavy snow" (15+ cm in 12 h) regions for the 20 cases. Cases are labeled as in Table I.

Fig. 3.1. WSI NOWrad mosaic of composite reflectivity at 1200 UTC 27 Nov 2002 (color scale to the right of the image, every 5 dBZ).

Fig. 3.2. Same as Fig. 3.1 except at 2000 UTC 7 Feb 2003.

Fig. 3.3. Same as Fig. 3.1 except at (a) 1200 UTC, (b) 1500 UTC, (c) 1800 UTC, and (d) 1915 UTC 16 Feb 2003.

Fig. 3.4. Same as Fig. 3.1 except at (a) 1500 UTC and (b) 1600 UTC 6 Dec 2003.

Fig. 3.5. Same as Fig. 3.1 except at (a) 2000 UTC and (b) 2115 UTC 14 Dec 2003.

Fig. 3.6. Same as Fig. 3.1 except at 1500 UTC 17 Feb 2003.

Fig. 3.7. Same as Fig. 3.1 except at 1500 UTC 16 Mar 2004.

Fig. 3.8. Same as Fig. 3.1 except at 1345 UTC 12 Mar 2005.

Fig. 3.9. Same as Fig. 3.1 except at 1200 UTC 16 Mar 2004.

Fig. 3.10. (a) Same as Fig. 3.1 except at 0000 UTC 26 Dec 2002, (b) 700–650 hPa layer-averaged frontogenesis [color scale to the right of the image, every 3 K (100 km)$^{-1}$ (3 h)$^{-1}$] at 0000 UTC 26 Dec 2002, and (c) NARR 3-h model-derived accumulated precipitation ending 0000 UTC 26 Dec 2002 (color scale to the right of the image, every 2 mm).

Fig. 3.11. (a) Depth of EPV* < 0.25 PVU (color scale to the right of the image, every 50 hPa) at 2100 UTC 7 Feb 2003; hatching indicates CI. (b) Same as Fig. 3.1 except at 2100 UTC 7 Feb 2003.

Fig. 3.12. (a) Upper left: same as Fig. 3.1 except at 2100 UTC 7 Feb 2003, white line indicates cross section slice; Lower right: Saturation equivalent potential temperature (thin black contours, every 3 K), EPV* (green and blue contours, every 0.25 PVU from −0.50 to 0.50 PVU), vertical velocity (red heavy dashed line, every −4 μb s^{-1} starting at −4 μb s^{-1}), −12°C and −18°C isotherms (heavy black lines), relative humidity (color scale to the lower left, every 10%), and 2D frontogenesis [color scale to the lower right, every 1 K (100 km)$^{-1}$ 3 h^{-1}] at 2100 UTC 7 Feb 2003. (b) Same as Fig. 3.12a except EPV$_g^*$ in place of EPV*.

Fig. 3.13. (a–b) Same as Fig. 3.12 except at 2100 UTC 22 Jan 2005.

Fig. 3.14. (a–b) Same as Fig. 3.12 except at 0300 UTC 9 Mar 2005.

Fig. 3.15. (a–b) Same as Fig. 3.12 except at 1200 UTC 27 Nov 2002.

Fig. 3.16. (a–b) Same as Fig. 3.12 except at 1200 UTC 7 Feb 2003.

Fig. 3.17. (a–b) Same as Fig. 3.12 except at 1500 UTC 6 Mar 2003.

Fig. 3.18. (a–b) Same as Fig. 3.12 except at 1800 UTC 6 Mar 2003.

Fig. 3.19. (a–b) Same as Fig. 3.12 except at 1500 UTC 16 Feb 2003.

Fig. 3.20. (a–b) Same as Fig. 3.12 except at 0600 UTC 23 Jan 2005.

Fig. 3.21. (a–b) Same as Fig. 3.12 except at 1500 UTC 6 Dec 2003.

Fig. 3.22. (a–b) Same as Fig. 3.12 except at 2100 UTC 14 Dec 2003.

Fig. 3.23. (a–b) Same as Fig. 3.22 except with a different cross section slice.

Fig. 3.24. (a–b) Same as Fig. 3.12 except at 0000 UTC 17 Mar 2004.

Fig. 3.25. (a–b) Same as Fig. 3.12 except at 0000 UTC 1 Mar 2005.

Fig. 3.26. (a–b) Same as Fig. 3.12 except at 1500 UTC 17 Feb 2003.

Fig. 3.27. (a–b) Same as Fig. 3.12 except at 0300 UTC 25 Feb 2005.

Fig. 3.28. Same as Fig. 3.1 except at (a) 0300 UTC and (b) 0900 UTC 25 Feb 2005

Fig. 3.29. Same as Fig. 3.1 except at (a) 0800 UTC and (b) 0900 UTC 19 Mar 2004.

Fig. 3.30. (a–b) Same as Fig. 3.12 except at 0900 UTC 19 Mar 2004.

Fig. 3.31. Same as Fig. 3.1 except at 0300 UTC 15 Dec 2003.

Fig. 3.32. (a–b) Same as Fig. 3.12 except at 0300 UTC 15 Dec 2003.

Fig. 3.33. (a–b) Same as Fig. 3.12 except at 1500 UTC 16 Mar 2004.

Fig. 3.34. (a–b) Same as Fig. 3.12 except at 0900 UTC 1 Mar 2005.

Fig. 3.35. (a–b) Same as Fig. 3.12 except at 1200 UTC 16 Mar 2004.

Fig. 3.36. (a–b) Same as Fig. 3.12 except at 0900 UTC 1 Mar 2005.

Fig. 4.1. (a–b) Same as Fig. 3.13 except with a different cross section slice.

Fig. 4.2. (a–b) Same as Fig. 3.12 except with a different cross section slice.

Fig. 4.3. Schematic of the “escalator–elevator” pattern of warm-frontal ascent. The warm conveyor belt (light gray arrows) rises over the cold conveyor belt (tubular dashed

arrow). Mesoconvective ascent (the "elevator," black arrows) and accompanying convective clouds (dark gray shading with white anvils) are shown between regions of upglide ascent (the "escalator") [From Neiman et al. (1993)].

Fig. 4.4. (a–e) Schematic cross sections in the *x–p* plane for the five modes. Fields shown are frontogenesis (green shading), ascent (dashed), EPV_g^* bull's-eyes (light blue shading), and CI (purple shading). Cross-section length is approximately 600 km. Cross-section vertical axis is 1000–300 hPa.

Fig. 4.5. Flowchart for forecasting snow modes during Northeast snowstorms.

1. Introduction

1.1 General Purpose

Cold-season frozen precipitation in the northeastern United States is manifest in a variety of spatial patterns evident on radar imagery. Although forecasters can predict likely areas of precipitation, considerable difficulty remains in properly identifying mesoscale precipitation signatures within the main precipitation shield. As viewed on a radar reflectivity image, precipitation can appear, for example, relatively uniform, fractured, or banded. The ability to forecast such mesoscale precipitation characteristics is vital in adding value to a forecast by enhancing the mesoscale prediction of snowfall amount and variability and by differentiating between high-impact and low-impact snowfalls.

Twenty "heavy snow" events in the Northeast from the winters of 2002–03 through 2004–05 are selected for analysis using several criteria based on precipitation type, snowfall, time of year, and location. A radar classification is performed, followed by an ingredients-based (lift, instability, moisture, and microphysics) analysis using cross sections and plan-view maps. The parameters that distinguish the different patterns, or modes, are discussed, along with ideas for future research.

1.2 Literature Review

1.2.1 Ingredients-based Methodology

An ingredients-based methodology (IM) has been utilized in the field of meteorology for several decades. An early example of such a methodology is McNulty's (1978) IM for forecasting severe weather, which relates its occurrence to the location of

upper-tropospheric wind maxima and troughs. A classic IM is Doswell's (1987) one for deep, moist convection, which uses moisture, conditional instability, and lift for ingredients. If one ingredient is removed, an important weather phenomenon may still occur, but it will most likely not be deep, moist convection. The author also points out that other factors, such as the vertical wind profile can affect the type of convection that forms but that only the three *ingredients* determine whether such convection forms at all. These same three ingredients for moist *upright* convection can also be applied to moist *slantwise* convection (Schultz and Schumacher 1999). The only difference is that moist *gravitational* instability is replaced with moist *symmetric* instability (to be discussed further in section 1.2.3).

Hane (1986) examines different types of rainbands and their formation using the ingredients of lift, instability, and moisture. He finds lifting mechanisms that include surface cold and warm fronts, prefrontal cold surges, and gravity waves. Instabilities include moist gravitational, moist symmetric, and wave-CISK (conditional instability of the second kind; Charney and Eliassen 1964). Microphysics also play an important role, e.g., in seeder–feeder processes.

More recently, Wetzel and Martin (2001) discuss an operational IM for forecasting midlatitude winter weather. Their five ingredients are quasi-geostrophic (QG) forcing for ascent, moisture, instability (i.e., gravitational, inertial, or slantwise), precipitation efficiency through cloud microphysics, and temperature. This IM can be used to assess a numerical model's quantitative precipitation forecast (QPF) so that it is not merely used as a "black box."

Lastly, Jurewicz and Evans (2004) examine two banded snowstorms and note that the relative proportions of lift, instability, moisture, and microphysics lead to bands despite dissimilar synoptic setups. One case has classical characteristics of a snowstorm with strong cyclogenesis and strong QG forcing, while the other has weaker QG forcing located far from the banded precipitation. Yet, both has midtropospheric frontogenesis with reduced stability. Using this IM concept, the ingredients of lift, instability, moisture, and microphysics will be discussed in the context of banded precipitation in the upcoming sections.

1.2.2 Large-scale Forcing

Of the two main types of forcing, QG and frontogenetic, the former is discussed in this section, and the latter is introduced later on. QG-derived vertical motion is diagnosed using the standard QG omega equation [e.g., Eq. (5.6.14); Bluestein 1992] and the Q-vector form of the QG omega equation [e.g., Eqs. (7) and (8); Hoskins et al. 1978]. Ignoring friction and diabatic heating, the first form has two main forcing terms: differential absolute vorticity advection and the Laplacian of thermal advection (Bluestein 1992). The Q-vector form has vertical motion forced by the divergence of $\vec{Q}$, where $\vec{Q}$ is proportional to the vector rate of change of the horizontal potential temperature gradient implied by geostrophic motion (Hoskins et al. 1978). QG-derived lift, calculated from either form of the omega equation, in the presence of sufficient moisture, results in clouds and precipitation.

Carlson (1998) discusses conveyor belts as an alternative, Lagrangian way of examining large-scale ascent. Here, precipitation is a function of the moisture content of

the planetary boundary layer at the source of the cold and warm conveyor belts. Thus, more precipitation would be expected if the warm conveyor belt originated over the Gulf of Mexico rather than over the continental United States. These synoptic-scale features, along with smaller meso-α (200–2000 km; Orlanski 1975) phenomena are summarized in Kocin and Uccellini's (2004) work on Northeast U.S. snowstorms (Fig. 1.1). This figure displays how conveyor belts and jets play an important role in providing cold air, sufficient moisture, and strong forcing in the development of a snowstorm.

Large-scale flow properties, e.g., confluence and diffluence, can also affect the structure of a midlatitude cyclone (Schultz et al. 1998). These, in turn, would be expected to affect the distribution of precipitation about a cyclone. Yet, other non-QG motions, e.g., frontal circulations, are still important in the total ascent (Wetzel and Martin 2001), and they will be discussed in section 1.2.4.

1.2.3 Instability

1.2.3.1 Definition

Schultz and Schumacher (1999) show how the equations for dry, conditional, and potential gravitational instabilities are isomorphic to those for symmetric instability, except that symmetric instabilities are calculated along constant geostrophic absolute momentum (M_g) surfaces, where $M_g = v_g + fx$ and x represents distance increasing toward warmer air. For example, conditional (upright) gravitational instability (CI) exists when $\partial \theta_e^* / \partial z < 0$, and conditional (slantwise) symmetric instability (CSI) exists when $\partial \theta_e^* / \partial z\big|_{M_g} < 0$, where θ_e^* is the saturation equivalent potential temperature. A similar relationship exists for potential gravitational instability (PI) and potential symmetric

instability (PSI), except that θ_e^* is replaced by θ_e, where θ_e is the equivalent potential temperature. It is worth nothing that the equations for the dry versions of gravitational and symmetric instabilities are also similar to that for inertial instability, defined as $\partial M_g/\partial x < 0$.

1.2.3.2 M_g–θ *Relationship*

An alternative way to view symmetric instability is by plotting *x*–*p* cross sections of M_g and θ surfaces. In regions where M_g surfaces slope less steeply than θ surfaces, dry symmetric instability exists, assuming that the region is stable to horizontal and gravitational displacements (Schultz and Schumacher 1999). As with the instability definitions, θ is once again replaced by θ_e^* and θ_e for conditional and potential symmetric instabilities, respectively. Schultz and Schumacher (1999) also observe that the M_g–θ_e relationship is commonly misused in discussions of CSI where the M_g–θ_e^* relationship would be appropriate.

Figure 1.2 demonstrates the M–θ_e relationship for symmetric instability (Sanders and Bosart 1985). (The authors do not use the geostrophic wind in this figure, and the geostrophic wind versus full wind debate will be discussed further in section 1.2.3.5.) Parcel A is given a leftward horizontal displacement, causing it to possess a larger M and θ_e than the environment. Restoring forces bring the parcel nearly back to its original location; this is a stable situation. Parcel B is given an upward displacement, leaving it with a smaller M and θ_e than the environment. Restoring forces once again bring the parcel nearly back to its original location; this is another stable situation. Parcel C, however, is given a slantwise displacement. Gravitational and inertial restoring forces

now partially cancel each other, allowing the parcel to accelerate in the slantwise direction. Thus, it can be seen why the slopes of the two surfaces are so critical.

1.2.3.3 EPV Diagnostic

A simpler way to view symmetric instability without the use of M_g and θ surfaces is through the use of the equivalent potential vorticity (EPV) diagnostic. Hoskins (1974) extends the M_g–θ relationship to three dimensions by relating it to geostrophic potential vorticity, PV_g. $PV_g = g \cdot \vec{\eta}_g \cdot \vec{\nabla}\theta$, where $\vec{\eta}_g$ is the three-dimensional absolute vorticity vector, and $\vec{\nabla}\theta$ is the three-dimensional gradient of potential temperature. For CSI and PSI, θ is again replaced with θ_e^* and θ_e, respectively. The EPV diagnostic for CSI is referred to as geostrophic saturation equivalent potential vorticity (EPV_g^*) and for PSI is referred to as geostrophic equivalent potential vorticity (EPV_g).

Loughe et al. (1995) show that the EPV diagnostic for PSI using hydrostatic pressure coordinates is

$$\text{EPV} = -g(\zeta_p + f)\frac{\partial \theta_e}{\partial p} + g\left(\frac{\partial v}{\partial p}\frac{\partial \theta_e}{\partial x} - \frac{\partial u}{\partial p}\frac{\partial \theta_e}{\partial y}\right), \quad (1)$$

where ζ_p is the vertical component of the relative vorticity of the full wind in pressure coordinates and f is the local value of the Coriolis parameter. [These authors also do not use the geostrophic wind similar to the approach taken in Sanders and Bosart (1985).] The first term contains the vertical vorticity and stability, while the second term represents the contributions of the horizontal components of the vorticity to EPV.

Moore and Lambert (1993) deduce a two-dimensional (2D) form of EPV_g by neglecting variations with respect to y and by applying the hydrostatic approximation:

$$\text{EPV} = g\left[\left(\frac{\partial M_g}{\partial p}\frac{\partial \theta_e}{\partial x}\right) - \left(\frac{\partial M_g}{\partial x}\frac{\partial \theta_e}{\partial p}\right)\right]. \quad (2)$$

Here, the first term represents the contribution to EPV from the vertical wind shear and the horizontal θ_e gradient. Assuming saturation, when θ_e increases in the x direction ($\partial\theta_e/\partial x > 0$), the wind increases with height, rendering $\partial M_g/\partial p$ less than zero. Thus, when the θ_e gradient and associated wind shear are large, $\partial M_g/\partial p$ is more negative, and M_g surfaces have shallower slopes in the x–p plane, favoring PSI. In the second term, since the absolute vorticity ($\partial M_g/\partial x$) is almost always positive, if the stability ($\partial\theta_e/\partial p$) is small, then the second term only partially counteracts the first term. If PI exists ($\partial\theta_e/\partial p > 0$), then the EPV is even more negative.

Nicosia and Grumm (1999) discuss how EPV is reduced via

$$\frac{d(EPV)}{dt} = g\frac{\vec{k}\cdot(\nabla\theta_e \times \nabla\theta)}{\rho\bar{\theta}}, \quad (3)$$

where $\bar{\theta}$ is an average value of θ in the midtroposphere and ρ is density. The EPV decreases following the motion when the moisture gradient lies in a similar direction to that of the thermal wind vector, which occurs in developing midlatitude cyclones with cold air to the north and moist air to the east. As the dry air from the west advects over the underlying moist air, θ_e surfaces steepen, reducing the EPV as observed in the second term in (2).

When Moore and Lambert (1993) explicitly show fields of EPV in x–p cross sections to demonstrate its relationship with PSI (mistakenly referred to as CSI in the paper), the M_g–θ_e relationship is satisfied in the areas of negative EPV. Nicosia and Grumm (1999) note how EPV is analogous to the stability parameter in QG-forcing

equations: the smaller the value, the more "bang for the buck," i.e., more vigorous ascent.

Lastly, McCann (1995) creates plan-view plots of EPV in order to understand the spatial extent of an instability region. He explains that plan-view maps afford the operational forecaster the opportunity to quickly and easily understand the spatial extent of the instability without spending valuable time creating numerous cross sections. Such an approach is used as part of this study.

1.2.3.4 Coexistence of CI and CSI

As previously implied, negative EPV_g implies gravitational, symmetric, and/or inertial instability. CI (PI) is a special case of CSI (PSI), in which θ_e^* (θ_e) surfaces tilt more steeply than M_g surfaces *and* are buckled (Nicosia and Grumm 1999). Additionally, inertial instability is a special case of symmetric instability (Jurewicz and Evans 2004), in which M_g surfaces not only have shallower slopes than θ surfaces but also bend toward the ground in the colder air.

When CI and CSI coexist, CI dominates CSI because of its larger growth rate and energy release (Bennetts and Sharp 1982). Similarly, when symmetric and inertial instabilities coexist, symmetric instability dominates because of its relatively larger growth rate (Bennetts and Hoskins 1979). Jascourt et al. (1988) refer to CI/CSI (PI/PSI) coexistence as "convective–symmetric instability," which takes two forms (Xu 1986). First, "upscale development" features small-scale moist upright convection leading to the release of symmetric instability as the environment stabilizes gravitationally. Second, "downscale development" features bands in a moist symmetrically unstable environment

releasing latent heat, which destabilizes the midtroposphere, leading to upright convection. Additionally, O'Handley and Bosart (1989) discuss that as CSI rolls grow, midtropospheric differential advection of wet bulb potential temperature (θ_w) produces CI.

1.2.3.5 The Geostrophic vs. Full Wind Debate

Over the past two decades, authors have offered reasons for using the geostrophic wind or the full wind in calculating EPV and in demonstrating the M–θ relationship. Following previous work on the theory of symmetric instability, Hoskins (1974) states that geostrophic balance should be assumed, and Bennets and Hoskins (1979) utilize thermal wind balance, which assumes geostrophy. Schultz and Schumacher (1999) state that using M in place of M_g is inconsistent with 2D theory and thus recommend use of the geostrophic wind. Clark et al. (2002) write that thermal wind balance implies that the background basic-state potential vorticity is geostrophic. Xu (1992) claims that EPV can only be used for EPV_g if the flow is close to geostrophy and is very symmetrically stable.

Observations have also supported use of the geostrophic wind. Persson and Warner (1995) note that M_g surfaces more accurately capture the buckling in absolute momentum surfaces that takes place as instability grows. In a snowstorm case study, Clark et al. (2002) find that a particular snowband is more aligned with the minimum in EPV_g rather than the minimum in EPV on plan-view maps. In addition, the value of the EPV_g minimum is lower than that of the EPV minimum.

On the other hand, several authors offer reasons for using the full wind instead. Novak et al. (2004) prefer the use of the full wind because it better represents curved

flow. Nonetheless, they acknowledge the uncertainty about which "wind" to use. Gray and Thorpe (2001) claim the assumption that the time scale of convection is much less than the time scale of large-scale environmental changes might not be valid for slantwise convection. As reviewed in Jurewicz and Evans (2004), the potential for slantwise convection might be better ascertained by comparing parcel accelerations to the acceleration of an evolving and *un*balanced environment described by the full wind.

In a sounding-based study of convection and symmetric instability in central Alberta, Reuter and Aktary (1995) argue that the full wind can be used to approximate the geostrophic wind because observed vertical speed shear is usually very close to its geostrophic value. In a study of overrunning precipitation bands in the Southern Plains, Byrd (1989) suggests that bands may be better aligned with the vertical wind shear than with the thermal wind, as predicted by theory, because the top branch of the ageostrophic frontogenetical circulation (to be introduced in section 1.2.4.2) alters the band orientation. Thus, the debate continues and this author will offer his thoughts later in this thesis.

1.2.4 Frontogenetical Forcing and Instability Together with Moisture

1.2.4.1 Moisture

In order for a discussion of frontogenetical forcing and instability to be worthwhile in the context of precipitation, sufficient moisture must be present. Several authors set a relative humidity (RH) criterion of at least 80% to find regions in plan-view maps and cross sections where ample forcing can lead to saturation (Schultz and Schumacher 1999; Wetzel and Martin 2001; Jurewicz and Evans 2004). Others use an

RH criterion of 70%, e.g., Novak et al. (2004). Schultz and Schumacher (1999) write that their sub-100% value is chosen to account for data errors, model inadequacies, and/or saturation with respect to ice.

After calculating relative humidity with respect to water and with respect to ice for a number of temperatures and humidities using formulae (not shown) from Borhen and Albrecht (1998), it is observed that relative humidity with respect to ice rather than water can lead to substantial changes in the relative humidity. However, these changes are seen to be inconsequential when examining the overall signals from cross sections later in this study.

1.2.4.2 Frontogenetical Forcing

Quasi-geostrophic forcing is discussed earlier as a mechanism for heavy precipitation; however, frontogenetical forcing plays an important role in the mesoscale features of heavy precipitation, as seen in the upcoming sections. Bluestein's (1993) Eq. (2.3.3) defines 2D frontogenesis, after Miller (1948), as

$$F = \frac{D}{Dt}\left(-\frac{\partial\theta}{\partial y}\right)_p = \left(\frac{\partial v}{\partial y}\right)_p \left(\frac{\partial\theta}{\partial y}\right)_p + \left(\frac{\partial\omega}{\partial y}\right)_p \frac{\partial\theta}{\partial p} - \frac{1}{C_p}\left(\frac{p_0}{p}\right)^{\frac{R}{C_p}} \left(\frac{\partial}{\partial y}\right)_p \frac{dQ}{dt}, \qquad (4)$$

where C_p is the specific heat capacity of dry air at constant pressure, R is the gas constant for dry air, and $\frac{\partial Q}{\partial t}$ is the diabatic heating rate. Collectively, the three terms of frontogenesis are confluence, tilting, and differential diabatic heating. Confluence aids frontogenesis with cold air advection on the cold side and warm air advection on the warm side of the frontal zone. Tilting aids frontogenesis through ascending air on the cold side and descending air on the warm side. Lastly, differential diabatic heating aids

frontogenesis when, for example, during the day, the skies are clear on the warm side and cloudy on the cold side.

Another form of this equation is the 2D Petterssen equation (Petterssen 1956), which is used by the General Meteorology Package (GEMPAK; desJardines et al. 1991) in this research. The equation is defined as follows:

$$F = \frac{1}{\left|\vec{\nabla}_p \theta\right|}\left[-\left(\frac{\partial \theta}{\partial x}\right)^2 \frac{\partial u}{\partial x} - \frac{\partial \theta}{\partial y}\frac{\partial \theta}{\partial x}\frac{\partial v}{\partial x} - \frac{\partial \theta}{\partial x}\frac{\partial \theta}{\partial y}\frac{\partial u}{\partial y} - \left(\frac{\partial \theta}{\partial y}\right)^2 \frac{\partial v}{\partial y}\right]. \quad (5)$$

It is based on the stretching and shearing deformation of the horizontal wind field. When the angle between the axis of dilatation and the isotherms is between 0° and 45°, the deformation is frontogenetical; and when the angle is between 45° and 90°, the deormation is frontolytical. It is interesting to note that if *y* points toward colder air and diabatic terms are ignored, (4) and (5) are mathematically equivalent.

During frontogenesis, geostrophic confluence acts to increase the horizontal temperature gradient and to decrease the vertical wind shear through advections, both of which disturb thermal wind balance. Therefore, a thermally direct transverse circulation develops to restore the balance (Sanders and Bosart 1985). Figure 1.3 shows the resulting circulation with ascent in the warm air, descent in the cold air, and ageostrophic flow connecting the vertical velocity couplet.

1.2.4.3 Frontal Circulations with Stability Considerations

When the aforementioned frontogenesis is in the presence of reduced symmetric or gravitational stability, the frontogenetical circulation is enhanced. Emanuel (1985) shows how a frontal circulation with weak moist symmetric stability (WMSS; Novak et

al. 2006) on the warm side develops a strong, concentrated sloping updraft ahead of the region of maximum geostrophic frontogenetical forcing. Figures 1.4 and 1.5 show the circulation without and with the reduced stability on the warm side, respectively. Using rawinsonde data, Sanders and Bosart (1985) confirm Emanuel's work through an investigation of a snowband during the Megalopolitan Snowstorm of 1983. They connect the snowband to the frontogenetically-induced thermally direct ageostrophic circulation that is enhanced by WMSS in the warm air. Thorpe and Emanuel (1985) also show that frontogenesis proceeds at a much faster rate with WMSS, along with the contraction of the horizontal scale of the ascent in the warm air.

With the aid of *x*–*p* cross sections of EPV and frontogenesis, Nicosia and Grumm (1999) demonstrate the synergistic relationship between frontogenesis and reduced EPV and explain this feedback mechanism as follows: 1) frontogenesis increases $\nabla\theta$, which leads to a decrease in EPV according to (3), 2) frontogenesis enhances differential moisture advection, which increases $\nabla\theta_e$ and leads to a decrease in EPV according to (3), 3) reduced EPV enhances the thermally direct circulation and ageostrophic advections, and 4) these advections strengthen the frontogenesis, and the process continues.

The frontal circulation can also interact with symmetric and gravitational instability in a different manner. The circulation can lift parcels to the level of free slantwise convection (LFSC), which is analogous to the level of free convection (LFC) for upright convection. This act allows the release of moist symmetric instability through the slantwise acceleration of the rising air parcels (Schultz and Schumacher 1999). Likewise, frontal circulations can lift parcels to areas of CI, which can be located within

regions of CSI (Nicosia and Grumm 1999). Colman (1990) presents an example where air, after being lifted over a frontal inversion to its LFSC at 750 hPa, accelerates slantwise to its LFC at 700 hPa and then accelerates vertically. An example of PI, Martin (1998) discusses a case where frontal lifting of an observed environmental stratification leads to free convection. Thus, there are multiple ways in which frontal circulations and types of instability can interact, as will be seen throughout this thesis.

1.2.4.4 Banding

Assuming sufficient moisture, a single rainband (or snowband) can evolve from a frontal circulation in the presence of WMSS (Emanuel 1985; Thorpe and Emanuel 1985). Without the frontal circulation, a pure CSI band can form, but it will not last as long as one associated with a frontogenetical circulation (Xu 1992). Still, a band of heavy snow can form without instability due to forced frontal or orographic ascent.

In a case study of a narrow, heavy snowband with thunder and lightning in the central United States, Martin (1998) finds that it is forced by the vertical circulation associated with lower-tropospheric frontogenesis that is continuously supplied with high-θ_e Gulf of Mexico air. Furthermore, he states that the across-front difference in gravitational stability leads to its narrow width and strength. However, he states that the resolution of the model fields used in the study is not high enough to determine if CSI plays a role in the band.

For bands that do form from frontal circulations in the presence of reduced stability or instability, Nicosia and Grumm (1999) offer an explanation for their ultimate demise. As the cyclone becomes vertically stacked, differential moisture advection

decreases and saturation exists through a deep layer; thus, $\vec{k} \cdot (\nabla \theta_e \times \nabla \theta) \approx 0$. By (3), EPV can no longer be reduced, and so any CSI, CI, or WMSS present is lost as the atmosphere returns to a stable state. It is also possible that the region of negative or reduced EPV is advected away. In addition, the lifting mechanism is reduced or eliminated in a vertically stacked cyclone.

1.2.5 Microphysics

The last ingredient in the banded precipitation recipe is cloud microphysics. Wetzel and Martin (2001) first assess the likelihood of ice nucleation by examining cloud top temperatures to see if they are below −10°C. Second, they look for strong ascent around −15°C for maximum depositional growth of snow crystals. Research by Power et al. (1964) shows that low-density dendritic snow crystals are favored when the temperature is between −18°C and −12°C (the dendritic growth zone) but that crystal density increases when falling through layers rich in supercooled liquid water, i.e., where temperatures are between −10°C and −5°C. Furthermore, the density is lowered when flakes aggregate, or stick together, with temperatures between −4°C and 0°C (Roebber et al. 2003). Thus, the temperatures of the layers where the crystals form and fall through are important in both the efficiency of precipitation production and in the ultimate snow-to-liquid ratio.

Not only can microphysical processes directly lead to increased snowfall but they can also indirectly lead to heavier snowfall through enhanced frontogenesis. If there is greater precipitation production, then more latent heat is released during deposition, which leads to enhanced frontogenesis through the differential diabatic heating term of

(4). More intense frontogenesis either makes a band more likely to form or makes an existing one stronger.

Lastly, these microphysical ideas can be applied to actual snowstorms, as done by Jurewicz and Evans (2004). For one case, they find that a thin dendritic growth zone and a deep aggregation zone yield snow-to-liquid ratios of 10:1 to 15:1, which is average for the area in this study. For the other case, they find that a 2700-m deep dendritic growth zone between 850 hPa and 600 hPa, a shallow riming layer, and light winds yield snow-to-liquid ratios of up to 45:1! Thus, microphysics accounts for increased precipitation efficiency, higher snow-to-liquid ratios, and possibly increased ascent through more vigorous frontogenetical circulations.

1.2.6 Band vs. No Band

The ingredients mentioned thus far, while important for band production, do not guarantee that a band will form. So, case studies and statistical studies have been performed over the years to attempt to find factors that discriminate between banded and nonbanded events. The case studies examine each event individually, looking at all of the features as a whole to find similarities between events, whereas, for statistical studies, one parameter is isolated from each event and studied across all the cases.

1.2.6.1 Case Studies

Novak et al. (2004) perform a climatology and composites of banded precipitation cases in the northeastern United States cold season. Their results are summarized through conceptual models. Figure 1.6 shows that nonbanded cases have shallower

frontal slopes than banded cases, implying greater conditional stability within the frontal zone. Nonbanded cases also have weaker frontogenesis that is not as vertically aligned as for banded cases. Ascent is consequentially weaker and broader as predicted by the Sawyer–Eliassen equation [e.g., Eq. (2.5.53); Bluestein 1993]. Relative humidities are lower for nonbanded cases, as well. Yet, banded and nonbanded cases both have WMSS on the warm side of the frontogenesis region, which makes this instability hard to use as a distinguishing factor.

Figure 1.7 shows that banded cases can have a double-jet structure, a closed midlevel low with deformation and frontogenesis to its northwest, and diffluence ahead of a midlevel disturbance. This configuration is consistent with Schultz et al. (1998), who found that cyclones in diffluent flow are inclined to have frontogenesis in their northwest quadrants. Meanwhile, nonbanded cases have just one upper-level jet, a weak surface low, a weak midlevel trough, and deformation and frontogenesis only to the cyclone's northeast. This pattern, too, is consistent with Schultz et al. (1998), who found that cyclones in confluent flow are inclined to have frontogenesis in their northeast quadrants.

Several years earlier prior to Novak et al. (2004), Nicosia and Grumm (1999) perform case studies of three major Northeastern snowstorms. They also develop a conceptual model (Fig. 1.8) with which the work of Novak et al. (2004) agrees. The additional information presented in this figure is that near the midlevel frontogenesis region, the cold conveyor belt is juxtaposed with the dry tongue jet, causing a reduction in EPV according to (3) on the warm side of the frontogenesis region. The authors then offer some forecast implications based on their research. They claim a snowband is

possible if models indicate a vertically deep layer of very negative EPV in conjunction with strong midlevel frontogenesis. Additionally, they assert that finer-resolution models can simulate the meso-α environment conducive to a band without explicitly forecasting the band itself, and, therefore, a forecaster should be able to anticipate a band after noting the proper environment.

1.2.6.2 Statistical Studies

In a sounding-based study of banded versus nonbanded precipitation in the absence of frontal regions, Seltzer et al. (1985) finds that more-strongly banded cases have greater maximum vertical speed shear: 13–20 m s^{-1} km^{-1} for strongly banded cases versus 7–12 m s^{-1} km^{-1} for weakly banded to nonbanded cases. This difference is to be expected with stronger horizontal temperature gradients. In an analysis of winter season overrunning bands in the Southern Plains of the United States, Byrd (1989) finds no significant CAPE (convective available potential energy) or SCAPE (slantwise convective available potential energy) differences between banded and nonbanded cases. (SCAPE is CAPE calculated along an M_g surface during slantwise convection.) However, he does find that 700–500 hPa band-parallel shear is significantly higher for strongly banded cases than for weakly banded and nonbanded cases, as again expected with larger temperature gradients in frontal regions.

1.2.7 Thesis Concept

Schultz and Schumacher (1999) suggest that just as moist upright convection takes a number of forms, e.g., supercells, mesoscale convective complexes, and squall

lines, slantwise convection may behave similarly. Furthermore, they suggest that convective–symmetric instability may play a role and that the coincidence of upright and slantwise convection may manifest itself differently based on stability, lift, and moisture, for example. Weisman and Klemp (1982) have related "modes" of convection to CAPE and vertical wind shear; likewise, the purpose of this research is to explore what parameters lead to the appearance of different patterns, or "modes," of precipitation during Northeast winter storms. This goal will be achieved by examining the role of synoptic-scale and mesoscale forcings, gravitational and symmetric instabilities, moisture, and microphysics to determine the mesoscale structure and evolution of precipitation regions in these storms.

The reminder of this thesis is organized as follows: Chapter 2 discusses the data and methodology, including case selection, radar classification, plan-view analysis, and cross section analysis. Chapter 3 contains results of the various methodologies, while Chapter 4 offers further discussion on the modes and the distinguishing features. Lastly, Chapter 5 features concluding remarks and suggestions for future work.

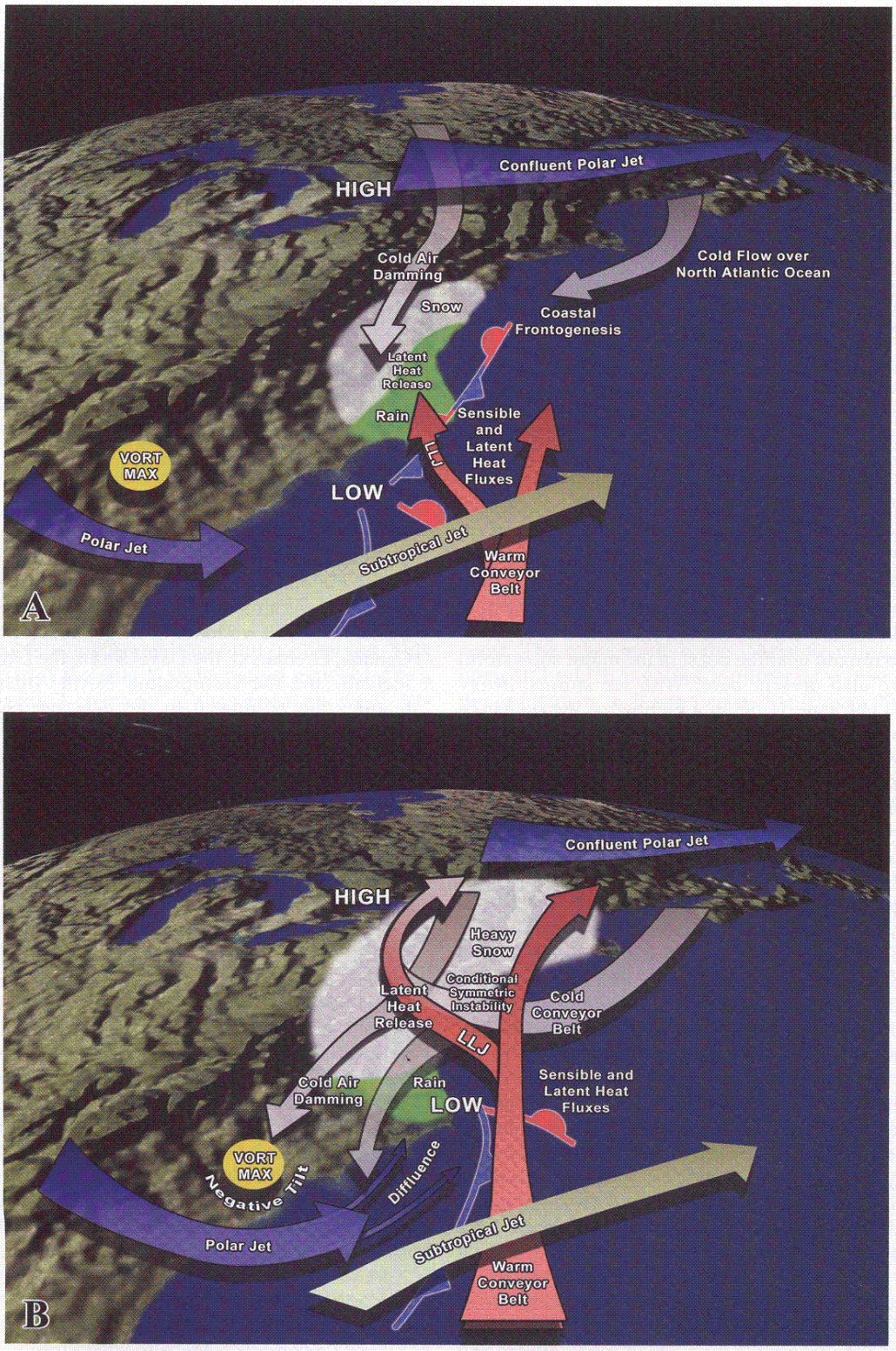

Fig. 1.1. Schematics of factors that contribute to heavy snowfall in the Northeast (a) during the initial development of the snowstorm and (b) when the snowstorm is fully developed [From Kocin and Uccellini (2004)].

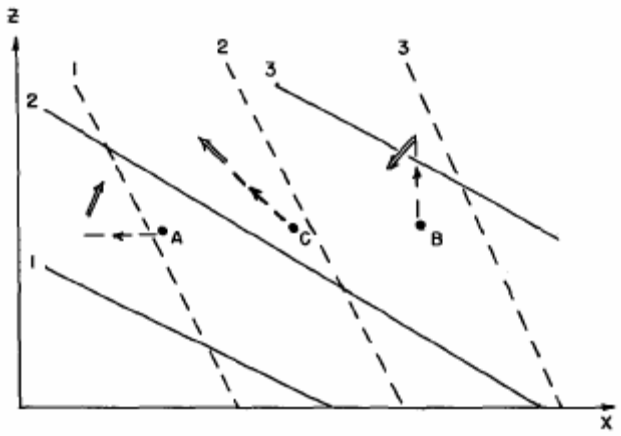

Fig. 1.2. Schematic vertical cross section illustrating (a) a stable horizontal displacement, (b) a stable vertical displacement, and (c) an unstable slantwise displacement. Solid lines represent absolute momentum of the basic flow. Dashed lines represent equivalent potential temperature. Dashed arrows show the initial displacement and the double-shafted arrows show the resulting accelerations [From Sanders and Bosart (1985)].

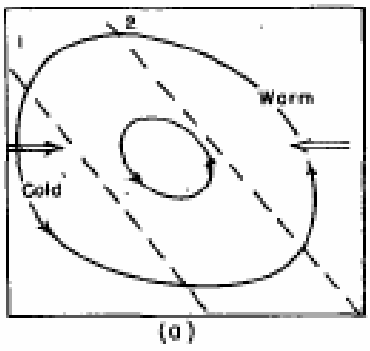

Fig. 1.3. Vertical cross section of the idealized transverse circulation associated with large-scale confluence (double-shafted arrows) [From Sanders and Bosart (1985)].

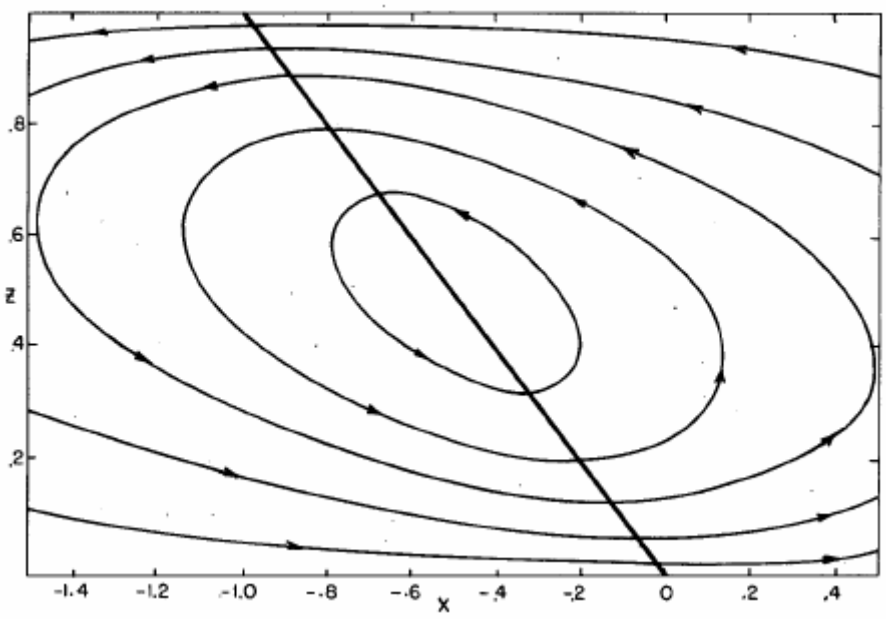

Fig. 1.4. The cross-front circulation in physical space with no variation in symmetric or gravitational stability. The diagonal solid line represents the frontogenesis axis [From Emanuel (1985)].

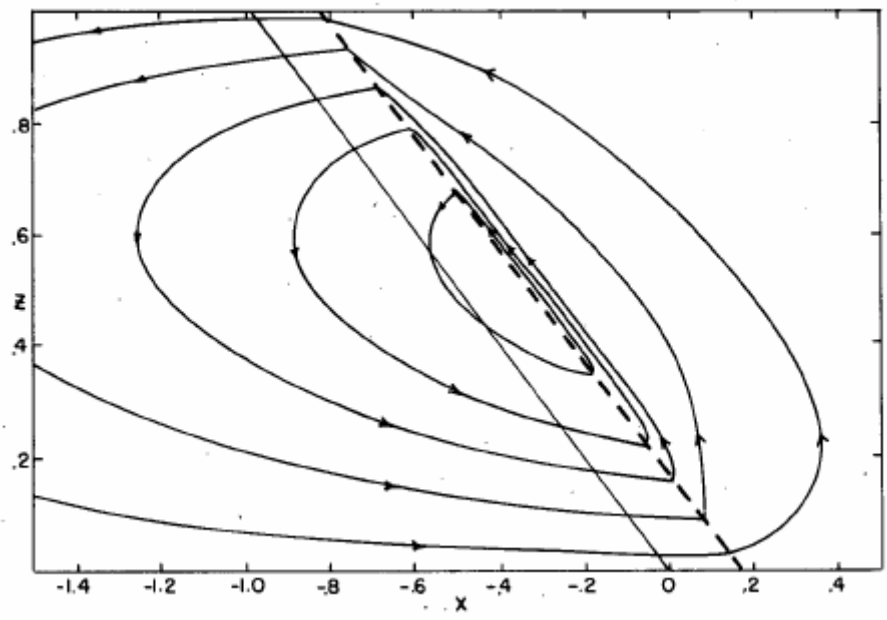

Fig. 1.5. As in Fig. 1.4 but with reduced potential vorticity on the right (warm) side of the frontogenesis region [From Emanuel (1985)].

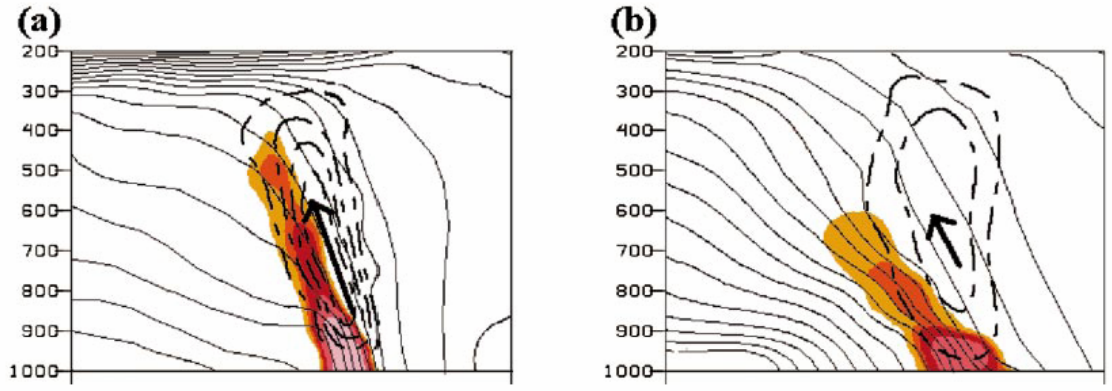

Fig. 1.6. Schematic *x–p* cross sections through a characteristic (a) single-banded and (b) nonbanded environment. The following fields are shown: frontogenesis (red shading), saturation equivalent potential temperature (thin solid), and ascent (dashed) with length of arrow relative to the magnitude of ascent and course of air parcel trajectory. Length of cross section approximately 1000 km [From Novak et al. (2004)].

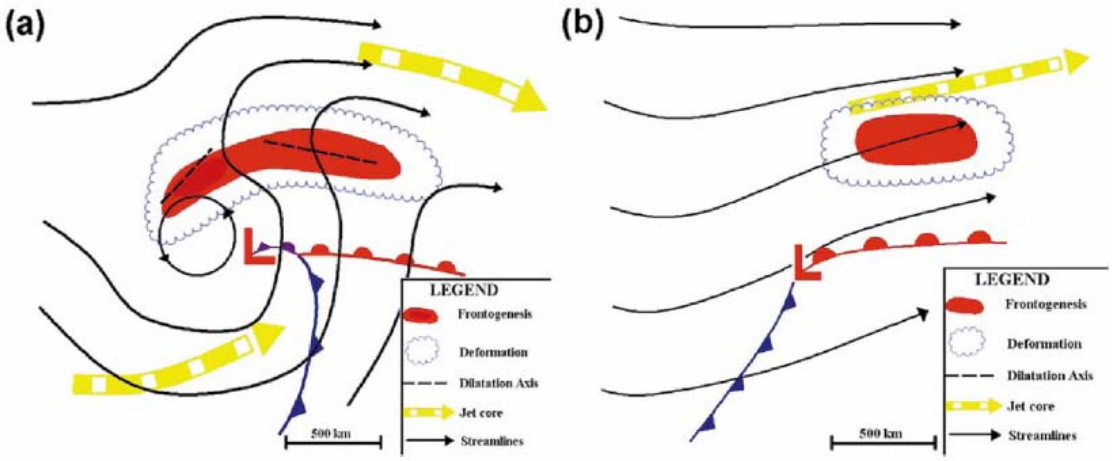

Fig. 1.7. Conceptual model of synoptic and mesoscale flows associated with (a) single-banded and (b) nonbanded events. Features shown are midlevel frontogenesis (red shading), midlevel deformation zone (scalloped) and associated dilatation axes [dashed lines in (a)], midlevel streamlines (black lines), and upper-level jet cores (wide dashed arrows) [From Novak et al. (2004)].

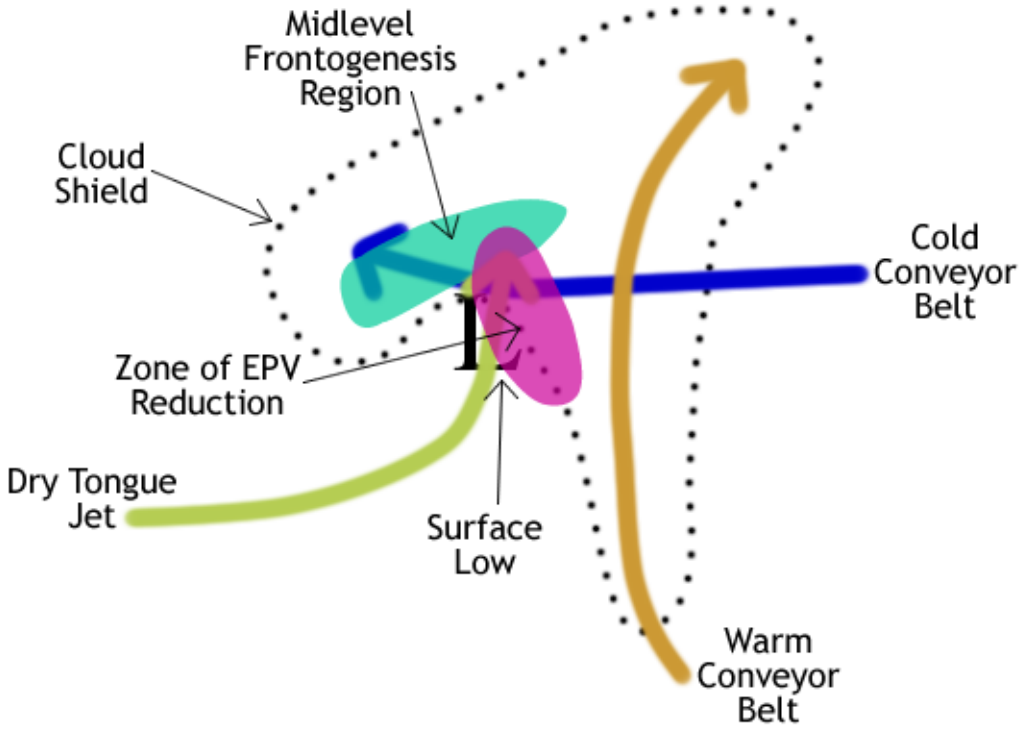

Fig. 1.8. Conceptual model depicting midlevel frontogenesis (green shading), zone of equivalent potential vorticity reduction (pink shading), cloud shield edges (dotted), cold conveyor belt (heavy blue line), warm conveyor belt (heavy orange line), dry tongue jet (heavy gold line), and the surface low (black L). Adapted from Nicosia and Grumm (1999).

2. Data and Methodology

2.1 Data

2.1.1 Radar

The radar product used for classifying the different precipitation modes in this study is the WSI Corporation NOWrad. Carbone et al. (2002) establishes its research worthiness in a radar-based climatology of warm-season precipitation episodes. They state that while inadequate for some research purposes, NOWrad is the only practical means to access the complete spatial and temporal coverage of the high-resolution WSR-88D (Weather Surveillance Radar-1988 Doppler) network. With 15-min resolution, this ~2-km latitude–longitude gridded dataset contains 16 levels of radar reflectivity factor data [10 log Z (mm^6 m^{-3})] at 5-dBZ intervals. While the exact algorithm for producing this thrice quality controlled product is proprietary to the WSI Corporation, it is best described as the maximum value of dBZ at any height in the column at each grid point. The radar grids are available online at the University Corporation for Atmospheric Research (UCAR) Mesoscale and Microscale Meteorology Division (MMM) website (http://locust. mmm.ucar.edu/WSI). In addition, NOWrad national mosaics can be viewed at another UCAR MMM website (http://locust.mmm.ucar.edu/case-selection).

2.1.2 Reanalyses

The two sets of reanalyses used in this study are the National Centers for Environmental Prediction–National Center for Atmospheric Research (NCEP–NCAR) Reanalysis (Kalnay et al. 1996; Kistler et al. 2001) and the North American Regional Reanalysis (NARR; Mesinger et al. 2006). Both sets of reanalysis grids are obtained

from the NOAA National Operational Model Archive and Distribution System (NOMADS) website (http://nomads.ncdc.noaa.gov). The NCEP–NCAR Reanalysis is a 6-h dataset with 2.5° latitude–longitude resolution on 17 standard pressure levels. The NARR is a 3-h dataset with 32-km resolution at its lowest latitude (12.2°N) on 29 pressure levels. The vertical resolution is 25 hPa from 1000 hPa to 700 hPa and from 275 to 100 hPa. Between 650 hPa and 300 hPa, the resolution is 50 hPa.

2.1.3 Data for Case Selection

National Climatic Data Center (NCDC) Next Generation Weather Radar (NEXRAD) national hourly mosaic reflectivity images are obtained from the NCDC website (http://www4.ncdc.noaa.gov/cgi-win/wwcgi.dll?WWNEXRAD~Images2). Public Information Statements (PNS) containing snowfall reports, plots of snowfall reports, and Northeast River Forecast Center snowfall maps are obtained from National Weather Service Weather Forecast Offices in the Northeast (http://www.erh.noaa. gov). These snowfall reports are supplemented with ones from NCDC's U.S. Storm Events Database (http://www4.ncdc.noaa.gov/cgi-win/wwcgi.dll?wwEvent~Storms). Lastly, Automated Surface Observing System (ASOS) reports, station plots, and surface maps are obtained from the Plymouth State Weather Center website (http://vortex. plymouth.edu/u-make.html).

2.2 Methodologies

2.2.1 Case Selection

In order to choose cases for this study, a number of selection criteria are established. Cases must occur in an area bounded by 36.5°N, 50°N, 65°W, and 85°W (Fig. 2.1) within U.S. radar coverage during the cool season, defined as 1 October–30 April, following Novak et al. (2004). Only non-warm sector precipitation is analyzed, and the precipitation must be predominantly in the form of snow in order to avoid bright banding and melting effects in the radar imagery and also to allow for some mixed precipitation near the coast and early in the event. "Heavy snow" is defined as 15+ cm (6+ in) of snow in 12 h over an area at least the size of Connecticut (~12,500 km^2). Areas of lake effect or lake-enhanced snows are not considered. Lastly, cases must occur during the three winters 2002–03, 2003–04, and 2004–05 due to the availability of the NOWrad dataset. Table I contains the resultant 20 cases, and Fig. 2.2 displays the "heavy snow" regions for each case.

2.2.2 Case Classification

Three methods are employed to classify the cases synoptically before the high-resolution radar imagery is analyzed for mesoscale precipitation characteristics. Because this author has observed that precipitation regions northwest and northeast of the surface cyclone take somewhat different forms, the first method subjectively classifies the cases into "overrunning," "wraparound," and "mixed" varieties using NOWrad national mosaics and surface maps. Cases where the "heavy snow" is primarily ahead of the surface low are designated "overrunning"; cases where the "heavy snow" is primarily to

the northwest of the surface low are designated "wraparound"; and cases where the "heavy snow" has considerable overlap between the two regions are designated "mixed."

Because more-jagged areas of precipitation have been observed in association with primarily differential cyclonic vorticity advection-driven events rather than with primarily warm air advection-driven events (D. Nicosia 2005, personal communication), the second method classifies the forcing for the "heavy snow" in each case. The classifications are primarily warm air advection (WAA), primarily differential cyclonic vorticity advection (DCVA), and a blend of the two. This technique is first performed with the NCEP–NCAR Reanalysis and then with the NARR by creating plots of WAA and DCVA with the General Meteorological Package (GEMPAK; desJardines et al. 1991). WAA is represented by the Laplacian of the advection of 1000–500 hPa thickness by the 700 hPa wind. DCVA is represented two ways: by both the 1000–500 hPa and 700–300 hPa differences in absolute vorticity advection divided by the appropriate pressure differential. Plots of WAA and DCVA are then compared to perform the classification.

The full wind is used rather than the geostrophic wind in calculating the advections, as this author has noticed that the geostrophic wind adds additional noise to the plots because of noisy geopotential height fields. Similarly, Shutts (1990) finds the geostrophic wind to be noisier than the full wind when working with the United Kingdom Meteorological Office's fine-mesh model.

As with all NARR plots in this research, GEMPAK's Gaussian filter with a weight of 6 is applied to the raw fields in the gddiag application with GFUNC= GWFS(…,6). This smoothing is performed because when the NARR model was

projected from its native model grid onto the NCEP Grid 221, a high level of ` was generated. To ameliorate that problem, the aforementioned Gaussian smoother has been found to provide the best balance of smooth fields and an acceptable loss of small-scale structures. For additional discussion, the reader is referred to the website of the Mesoscale Research Group of McGill University and the University at Albany (http://www.atmos.albany.edu/facstaff/rmctc/narr).

The third method classifies the cases by the position of the surface low relative to the 500 hPa geopotential height and 1000–500 hPa thickness patterns. This technique attempts to account for the primary QG forcing over the precipitation region, since DCVA is expected to dominate when the surface low is near the trough axis and WAA is expected to dominate as the surface low is approaching the ridge axis. For this scheme, the trough-to-ridge pattern is divided into quarters, where each quarter is one-eighth of the wavelength of the thickness or geopotential height pattern. Then, it is subjectively determined into which quarter the surface low is located at each time step during the "heavy snow" event. Lastly, this classification is correlated with the WAA/DCVA classification.

2.2.3 Radar Classification

In this stage of the research, northeast U.S. NOWrad mosaics generated in GEMPAK are examined. Various patterns and common signatures between cases are noted, along with the shape of stronger and weaker dB*Z* regions. Interesting features evident for a very brief time or over a tiny area are not considered. A problem arises of how much inhomogeneity in the data is enough to distinguish a uniform precipitation

shield from one with embedded patterns. Additionally, some patterns are unclassifiable, e.g., hybrid patterns, ones with only one or two examples of its kind in this case sample, squall lines, and gravity waves. There are also isolated cases where the NARR is unacceptable for analysis due to obvious errors. For example, for the 25–26 Dec 2002 snowstorm, the NARR barely has any frontogenesis in the vicinity of the intense snowband in New York. In addition, the NARR 3-h model-derived accumulated precipitation field has values near zero where the band is located. Thus, for parts of cases where the NARR is unacceptable, the radar pattern is not examined since the NARR would not be able to be accurately analyzed in sections 2.2.4–2.2.5. Regardless of these complications, the five resultant precipitation patterns, or modes, are "uniform," "classic band," "transient band," "bandlets," and "fractured," and will be discussed in detail in Chapter 3.

2.2.4 Plan-view Analysis

The following four methods are carried out in order to find correlations with the modes. Because most cases fit into the 'blend' category in the second case classification method (see sections 2.2.2 and 3.1), the ratio of DCVA to the sum of DCVA and WAA is plotted. As in section 2.2.2, WAA is calculated using the Laplacian of the advection of 1000–500 hPa thickness by the 700 hPa wind, and DCVA is calculated two ways: by both the 1000–500 hPa and 700–300 hPa differences in absolute vorticity advection divided by the appropriate pressure differential. To create smooth plots of these ratios, the NARR raw fields are smoothed with the Gaussian filter weight set to 20 (instead of 6). Additionally, when the ratio is plotted with the GEMPAK gdcntr application, every

other grid point is plotted with IJSKIP=1, and a 9-point smoother is applied with GFUNC=sm9s(…).

Second, the depths of EPV* layers satisfying various criteria are examined to see what affect the depth has on the precipitation mode. This method is inspired by the EPV depth charts produced by the Canadian Meteorological Centre (http://deved.meted.ucar.edu/norlat/slant/epv). FORTRAN scripts are developed to count layers meeting EPV* criteria that also have RH ≥ 70% and ascent and to identify layers of CI, where $\partial\theta_e^*/\partial p > 0$. The EPV* criteria include EPV* ≤ 0 PVU, EPV* ≤ 0.25 PVU, EPV* ≤ −0.25 PVU, and 0 ≤ EPV* ≤ 0.25 PVU. Plots of these depths are generated in GEMPAK, along with overlays of CI areas. The plots are created with both the geostrophic wind and full wind formulations of EPV*. FORTRAN scripts are also developed to ascertain if CSI, CI, or WMSS is the dominant stability feature at each grid point, and then GEMPAK plots are produced based on this information.

Third, because Seltzer et al. (1985) finds that strongly banded cases have greater maximum vertical speed shear than weakly banded and nonbanded cases, FORTRAN scripts are developed to find the 25 or 50 hPa layer with the greatest vertical speed shear at each grid point. From these data, GEMPAK plots of maximum vertical speed shear are produced. In addition, the 850–500 hPa speed shear is also plotted.

Lastly, horizontal maps are produced of 300, 500, 700, and 850 hPa geopotential heights in order to estimate height pattern–mode correlations.

2.2.5 Cross-section Analysis

Cross sections in the *x–p* plane are produced in GEMPAK that contain 2D Petterssen frontogenesis, RH, θ_e^*, EPV* (both geostrophic wind and full wind formulations), vertical motion, and the −12°C and −18°C isotherms. Cross sections are generated for multiple angles and lengths of slices at numerous times for each case. Representative cross sections are then selected for each mode in each case, and qualitative and quantitative observations are made of the following selected parameters: frontogenesis slope and magnitude; whether or not the frontogenesis is surface-based; whether or not the frontogenesis is vertically aligned; patterns and values of EPV* and EPV_g^*; CSI (using both EPV* and EPV_g^*); CI; ascent magnitude and tilt; whether or not the vertical velocity maximum intersects the dendritic growth zone, the minimum in EPV*, or an area of CI; the depth of the dendritic growth zone; and the RH values and patterns.

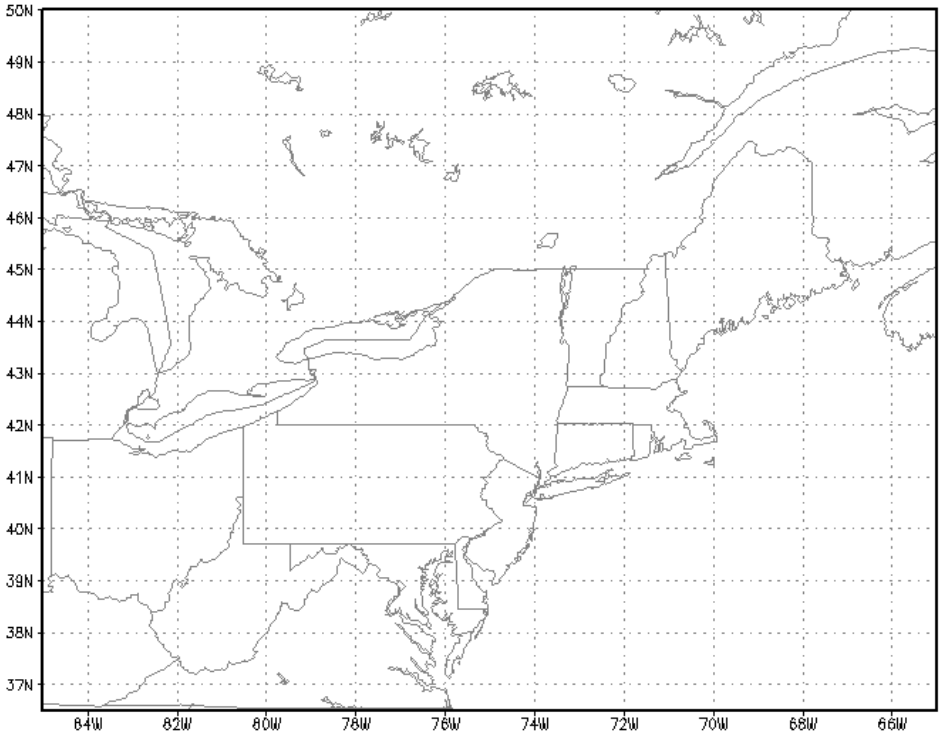

Fig. 2.1. Case selection domain; domain is bounded by 36.5°N, 50°N, 65°W, and 85°W.

TABLE I. 20 "heavy snow" cases selected using criteria in section 2.2.1.

Case	**Dates**	**Case**	**Dates**
1	26–27 Nov 2002	11	27–28 Jan 2004
2	4–6 Dec 2002	12	16–17 Mar 2004
3	25–26 Dec 2002	13	18–19 Mar 2004
4	2–5 Jan 2003	14	19–20 Jan 2005
5	6–7 Feb 2003	15	22–23 Jan 2005
6	15–18 Feb 2003	16	24–25 Feb 2005
7	6 Mar 2003	17	28 Feb–2 Mar 2005
8	5–8 Dec 2003	18	8–9 Mar 2005
9	13–15 Dec 2003	19	11–13 Mar 2005
10	14–15 Jan 2004	20	23–24 Mar 2005

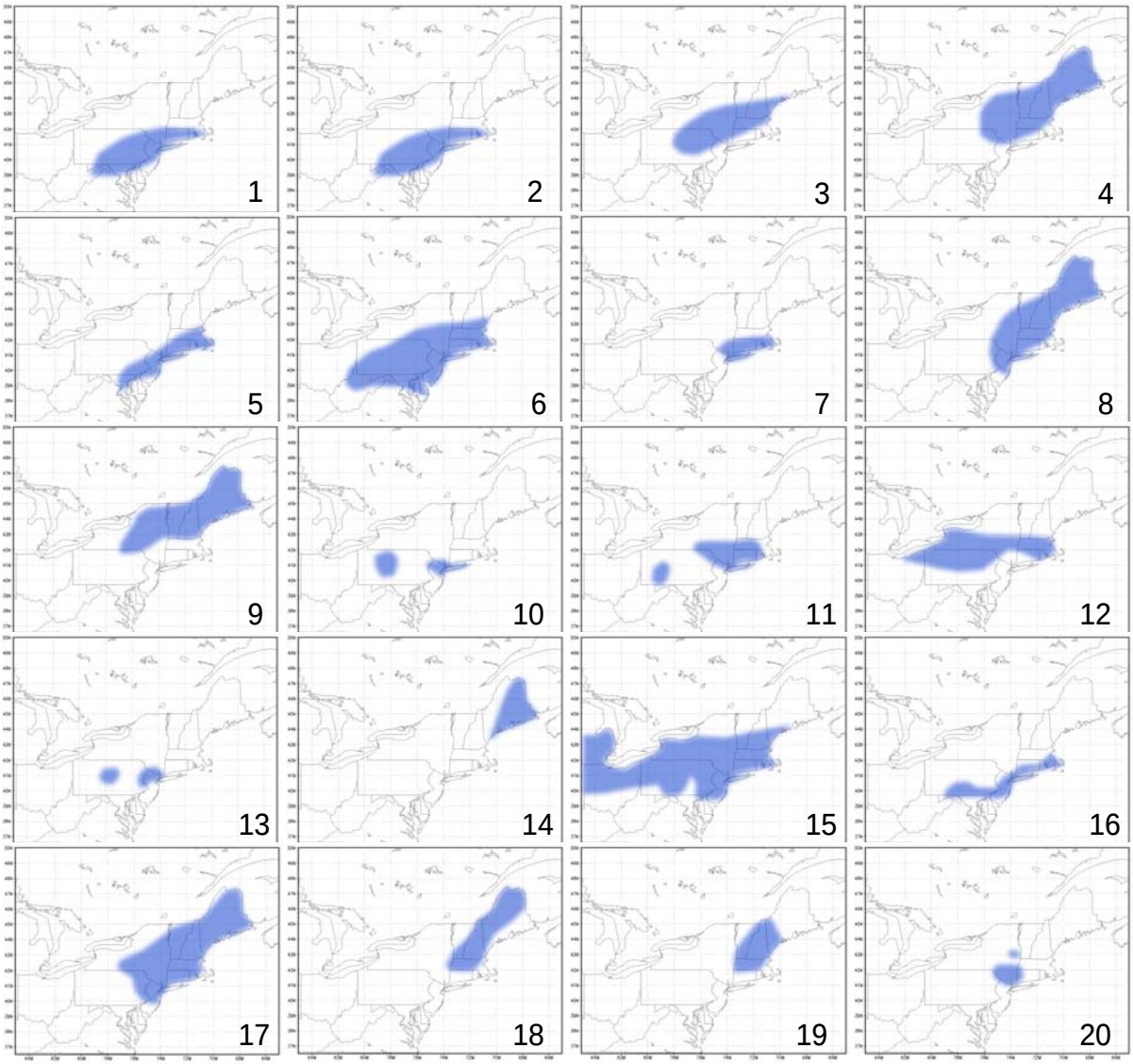

Fig. 2.2. "Heavy snow" (15+ cm in 12 h) regions for the 20 cases. Cases are labeled as in Table I.

3. Results

3.1 Case Classification

The first two attempts to synoptically classify the cases (section 2.2.2) yield very inconclusive results. For the overrunning/wraparound/mixed classification, most cases fall into the mixed category, rendering that classification scheme worthless. For the DCVA/WAA/blend classification, 18 of the 20 cases have a blend at some point during their heavy snowfall. Furthermore, it appears that the blends span the entire DCVA–WAA spectrum, which is why the ratio of DCVA to the sum of DCVA and WAA is calculated later on. In addition, these two classifications do not correlate well to each other, e.g., wraparound precipitation is not just DCVA-driven.

To attempt to account for these blends, the third method classifies the cases by the position of the surface low relative to the 500 hPa geopotential height and 1000–500 hPa thickness patterns. However, the low locations do not correlate well with the relative amount of DCVA. Thus, a radar classification should be and is performed first before NARR analyses are examined for synoptic and mesoscale information.

3.2 Radar Classification

3.2.1 Five Modes

The analysis of northeast U.S. NOWrad mosaics yield five precipitation patterns, or modes: "uniform," "classic band," "transient band," "bandlets," and "fractured." In this section, descriptions and sample imagery for each mode are offered. In addition, Table II presents the modes in each case, along with the 3-h times corresponding to the NARR analyses when they are present.

The "uniform" mode refers to a steady, moderate-to-heavy snow, e.g., Case 1 at 1200 UTC 27 Nov 2002 (Fig. 3.1). This mode is composed of a homogeneous precipitation shield of usually 20–25, although occasionally as high as 30, dB*Z* echoes. The only inhomogeneities present in the precipitation shield are differences of ±5 dB*Z* at a few pixels in the radar image and gentle reflectivity gradients toward the edges of the shield.

The "classic band" mode refers to a linear area of 30–35 dB*Z* echoes within an otherwise uniform precipitation shield, e.g., Case 5 at 2000 UTC 7 Feb 2003 (Fig. 3.2). This linear area of enhanced reflectivity also has high temporal coherency, distinguishing it from the next mode.

The "transient band" mode appears in three varieties: "evolving band," "broken band," and "messy band." The "evolving band" is a smaller-sized band than the "classic band" and does not have good temporal coherency. As viewed on a radar loop, it appears to disappear, redevelop, and take on a somewhat different appearance over time. Figures 3.3a–d show the evolution of an "evolving band" in southern New Jersey from Case 6 at 1200, 1500, 1800, and 1915 UTC 16 Feb 2003. The "broken band" is composed of linearly organized 25–35 dB*Z* segments that have < 20 dB*Z* breaks along the band. The echoes move together as a band, but breaks develop and close up as the band moves. Figures 3.4a–b show such a band in the Hudson Valley and New Jersey from Case 8 at 1500 and 1600 UTC 6 Dec 2003. Lastly, a "messy band" is an enhanced quasi-linear area of reflectivity with a grainy appearance and abundant 35 dB*Z* echoes that move together even though the resultant band is not nearly as smooth-looking as a "classic

band." Figures 3.5a–b from Case 9 at 2000 and 2115 UTC 14 Dec 2003 show such a band progressing northeastward in Upstate New York.

The "bandlets" mode refers to short segments or elliptical pieces of reflectivity 5–10 dB*Z* greater than that of the background precipitation shield. In Case 6 at 1500 UTC 17 Feb 2003 (Fig. 3.6), these enhanced areas of reflectivity are found in southern New York, northeastern Pennsylvania, and northern New Jersey. The segments and elliptical pieces appear to have no organization linear or otherwise, differentiating this mode from the broken and messy bands in the "transient bands" mode. In addition, these "bandlets" form in a manner unrelated to "classic bands" (to be mentioned in section 3.4.1.4).

The "fractured" mode refers to broken precipitation shields where areas of 20–30 dB*Z* are juxtaposed with areas of 5–15 dB*Z*. Case 12 at 1500 UTC 16 Mar 2004 (Fig. 3.7) features this mode in New York and northern Pennsylvania. The snow associated with this mode is a low-impact snow, i.e., 15+ cm falls in 6 h but the breaks in the precipitation allow for roads to be cleared and other precautions to be taken before moderate-to-heavy snow begins again.

3.2.2 Unclassifiable

As with any classification scheme, there are cases that do not fit into any category, and these cases are presented in this section. Table III shows the ten portions of cases that do not fit into one of the five aforementioned modes and brief reasons why they are unclassifiable. Such patterns include, hybrid patterns, unorganized grainy echoes, squall lines, and gravity waves. While these patterns are best revealed by

examining loops of radar mosaics, a single image of a grainy pattern over New England is presented in Fig. 3.8 from Case 19 at 1345 UTC 12 Mar 2005.

There are also three examples of precipitation patterns that are referred to as "solo light snowbands" (Table IV) in this thesis. While these snowbands seem to have their own category, these bands do not contribute to the heavy snow of a snowstorm. Solo light snowbands are surrounded by very light, i.e., 0–5 dB*Z*, areas of reflectivity, although they may be attached to the main precipitation shield by a finger of higher reflectivity as seen in Case 12 at 1200 UTC 16 Mar 2004 (Fig. 3.9). Here, the snowband is located in southern New York and is connected to the precipitation shield farther south by an area of snow in western Pennsylvania. So, even though these bands have the temporal coherency of classic bands, they do not contribute to the overall heavy snow and, thus, fall into this unclassifiable bin.

Lastly, as discussed in section 2.2.3, there are a few isolated cases where the NARR is unacceptable for analysis due to obvious errors. A great example is in Case 3 from the 25–26 Dec 2002 snowstorm. While an intense snowband is located over New York at 0000 UTC 26 Dec 2002 (Fig. 3.10a), the main frontogenesis region in the NARR is over the Gulf of Maine (Fig. 3.10b). Furthermore, the NARR 3-h model-derived accumulated precipitation field (Fig. 3.10c) has values near zero where the band is located and has its largest values over the Gulf of Maine, corresponding to the inferred misplacement of the band. Thus, a NARR examination would not be able to be accurately performed after classifying this radar pattern as a "classic band." So instead of officially classifying it and placing it in Table II, it is deemed unclassifiable and discussed in this section. There is also an example of unacceptable NARR in Case 15

around 1200 UTC 22 Jan 2005, where it is obvious that the upper-level low, an important feature in this case, is misplaced after a simple examination of radar imagery and soundings is performed (not shown). Lastly, Case 20 features a band from 0600–0900 UTC 24 Mar 2005 for which the NARR contains no forcing or instability in its vicinity (not shown).

3.3 Plan-view Analysis

The plan-view methodologies introduced in section 2.2.4 for the most part do not provide much help in distinguishing the five snow modes. No correlation is found between the DCVA/(DCVA+WAA) ratio and the mode, highlighted by examples of modes in individual cases that span the full spectrum of ratios at one time or over consecutive 3-h analyses. For example, the bandlets in Case 8 span ratios from 0 to 1 (not shown).

The EPV* depth methodology produces no relationships between the depths of EPV* satisfying any of the four EPV* criteria (see section 2.2.4) and the mode. It does appear that bands are located on EPV* depth gradients, e.g., the snowband over southern New England in Case 5 at 2100 UTC 7 Feb 2003 (Fig. 3.11). These gradients seem reasonable for band formation with WMSS and negative EPV* on the warm side of a frontal zone. In addition, Martin (1998) notes that an across-front difference in effective static stability is necessary to produce narrow bands of precipitation in frontal regions. However, these gradients are also found to exist with other modes, e.g., "uniform." The CI overlay on these plots reveals that "uniform" cases do not posses CI and that almost

all “bandlets” and “fractured” cases do have CI. Lastly, no link is found between the CSI/CI/WMSS classification and the mode, except for the CI relationship just mentioned.

No correlation is found between the mode and both the maximum vertical speed shear and the 850–500 hPa speed shear. Similar to the ratio plots, the shear varies greatly across modes in individual cases, and there are also similar values for different modes. Finally, the only relationship observed in the horizontal maps is that fractured cases all have weak 700-hPa closed or almost closed lows.

3.4 Cross-section analysis

3.4.1 Five Modes

In the following sections, representative cross sections in the *x*–*p* plane for each of the five modes are presented. For each example, a pair of cross sections made with both the full wind and geostrophic wind formulations of EPV* are shown. Because mixing in the boundary layer reduces EPV* significantly, EPV* in the boundary layer will be ignored in the text.

3.4.1.1 Classic Band

The “classic band” mode is found in Cases 5, 7, and 8 (Table II) and also in Case 3 that has the inadequate NARR. This mode contains strong [> 10 K (100 km)$^{-1}$ (3 h)$^{-1}$], steep frontogenesis with corresponding strong, slantwise ascent ≤ −16 μb s^{-1}, e.g., Case 5 at 2100 UTC 7 Feb 2003 (Fig. 3.12). For this mode, the frontogenesis appears to be surface-based, has its highest values near the ground, and has values of 5–8 K (100 km)$^{-1}$

$(3\ \mathrm{h})^{-1}$ above the boundary layer. The maximum values of ascent also extend downward toward the boundary layer.

The EPV* field for Case 5 shows a region of WMSS (0–0.25 PVU) above the frontogenesis. The other two "classic band" cases have a thin negative EPV* layer, corresponding to CI ($\partial \theta_e^* / \partial p > 0$) well above the northern part of the frontogenesis near the edge of the ascent region that is probably not realized. Schultz et al. (2000) state on the basis of their operational experience that a separation of 100–200 hPa between a region of frontogenesis and the location of the negative EPV* layer implies that a strong frontogenetical circulation is required to access the instability. The geostrophic EPV* field for these cases shows more expansive WMSS and negative EPV* regions each with a closed, minimum, quasi-circular EPV_g^* contour, or "bull's-eye," of −0.50 PVU through or above the frontal zone and co-located with the surface position of the band. So, while EPV* suggests minimal CSI involvement, EPV_g^* indicates deep regions of CSI.

The diagonal tilt of the vertical velocity fields in these cases indicates that non-CI motions dominate. If CI plays a role, then the vertical velocity fields would be expected to be more upright (as seen with "bandlets" later on). Thus, either frontogenesis alone (for the full wind EPV* calculation) or frontogenesis and CSI (for the geostrophic wind EPV* calculation) modulates the circulations causing precipitation in these cases. Lastly, the maximum ascent intersects the dendritic growth zone within a region of > 90% relative humidity.

3.4.1.2 Uniform

The "uniform" mode is found in Cases 1, 5, 6, 7, 8, 10, 15, 16, and 18 (Table II) and its cross sections can be divided into two categories: those with weak, flat, or no frontogenesis (Cases 1, 8, 10, 15, 16, and 18) and those with cross sections similar to "classic band" ones (Case 5, 6, and 7). To examine the first category of "uniform" precipitation, Case 15 at 2100 UTC 22 Jan 2005 (Fig. 3.13) and Case 18 at 0300 UTC 9 Mar 2005 (Fig. 3.14) are presented here.

Case 15 has weak [$\leq$ 4 K (100 km)$^{-1}$ (3 h)$^{-1}$], flat frontogenesis, and Case 18 has strong [>10 K (100 km)$^{-1}$ (3 h)$^{-1}$] frontogenesis above the boundary layer, but it is barely tilted above the horizontal. A look at all the cases in this type of "uniform" mode reveals that even though frontogenesis varies between 0 and 10 K (100 km)$^{-1}$ (3 h)$^{-1}$ above the boundary layer, it is either 1) weak and flat, 2) sloping but < 4 K (100 km)$^{-1}$ (3 h)$^{-1}$ above the boundary layer, or 3) strong but flat. So, either the frontogenesis is not steep, not strong, or not either, distinguishing a "uniform" frontogenesis cross section from a "classic band" one. In addition, the frontogenesis is surface-based in every case except for one (Case 8 at 0900 UTC 6 Dec 2003; not shown) that has very weak [< 2 K 100 km^{-1} (3 h)$^{-1}$] frontogenesis above the boundary layer.

Case 15 has the strongest ascent (< −24 μb s^{-1}) of any case in the entire study, while Case 18 has weaker ascent (~ −8 μb s^{-1}). A look at all the cases in this type of "uniform" mode reveals that maximum ascent varies between −4 and −24 μb s^{-1} and that five of the six examples of this type do not have ascent noticeably tilted in the plane of the cross section, as indicated by the vertical velocity contours.

Just like the ascent, the stability patterns vary greatly for this first type of "uniform" mode. Case 18, the most stable of this group, just has a thin, elevated WMSS layer, while Case 15 has WMSS and negative EPV* in both the upper and lower parts of the troposphere, indicating CSI (because $\partial \theta_e^* / \partial p < 0$ everywhere in the cross section). For this group of cases, WMSS layers vary from 50-hPa deep ones to ones spanning the entire depth of the troposphere, e.g., Case 1 at 1200 UTC 27 Nov 2002 (Fig. 3.15), which also has almost no frontogenesis. Additionally, half of these examples have CSI layers, as well. The EPV_g^* field in Case 15 is similar to that of the EPV* field, while for Case 18, the EPV_g^* has an added small negative region in the upper troposphere. Similar differences are noted in the other cases. Furthermore, none of these cases have realizable CI, i.e., there is no CI in the cross section except in areas clearly not involved in the formation of precipitation. Lastly, for most cases, the maximum ascent intersects the dendritic growth zone within a region of 80–90+% relative humidity.

As for the second type of "uniform" mode cross section, Case 5 at 1200 UTC 7 Feb 2003 (Fig. 3.16) is a representative example. Its cross section looks similar to that of the "classic band" with the strong, steep frontogenesis and slantwise vertical motion, but the slope and the vertical velocities are not quite as strong as for "classic bands" (cf. Fig. 3.12). Note that Fig. 3.16 evolves into Fig. 3.12 over 9 h, as the uniform area of precipitation tightens into band. During this time, the frontogenesis steepens and the ascent increases, but there is little change in the EPV* values for both formulations. Case 7 also shows a similar occurrence. A sloped area of frontogenesis with −12 μb s^{-1} ascent at 1500 UTC 6 Mar 2003 (Fig. 3.17) becomes a steeper, more intense area of frontogenesis with −16 μb s^{-1} ascent at 1800 UTC the same day (Fig. 3.18). Again, there

is little change in EPV* for both formulations, except that the negative values of EPV* diminish between 1500 and 1800 UTC.

3.4.1.3 Transient Band

The "transient band" mode is found in Cases 6, 8, 9, 11, 12, and 15 (Table II) and, as discussed in section 3.2.1, appears in three varieties: "evolving band" (Cases 6, 12, and 15), "broken band" (Cases 8 and 11), and "messy band" (Case 9).

The "evolving band" type of "transient band" is discussed in the context of Case 6 at 1500 UTC 16 Feb 2003 (Fig. 3.19). Here, the frontogenesis is weak [$\leq$ 2 K (100 km)$^{-1}$ (3 h)$^{-1}$], barely sloping, and decoupled from the surface. There is a similar setup for the other two "evolving bands," although the one in Case 15 at 0600 UTC 23 Jan 2005 (Fig. 3.20) has its relevant area of frontogenesis loosely connected to a much more intense area of frontogenesis to the south that is associated with a different, mixed-precipitation pattern over southern New England and adjacent waters. For these "evolving bands," the ascent is sloped with the frontogenesis but is not associated with boundary layer-based convergence (cf. Fig. 3.12). The EPV* field indicates WMSS above the frontal zone and some CSI near its northern edge. Case 12 (not shown) also has a thin layer of CI embedded within the WMSS, further altering the precipitation pattern. The EPV_g^* field, as seen with the other modes, exhibits a larger negative (CSI) region than does the EPV* field. Lastly, the maximum ascent intersects the dendritic growth zone within a region of 80–90+% relative humidity.

Next, the "broken band" type of "transient band" is discussed in the context of Case 8 at 1500 UTC 6 Dec 2003 (Fig. 3.21). For both "broken band" cases (8 and 11),

the frontogenesis region is weak [≤ 2 K (100 km)$^{-1}$ (3 h)$^{-1}$] and decoupled from the surface. The vertical velocity pattern displays no obvious slope due to CI effects. The EPV* field shows a layer of WMSS with embedded CI above the frontal zone, while the EPV_g^* field shows stacked EPV_g^* minima, or "bull's-eyes," co-located with the surface position of the band. The lower "bull's-eye" is a proxy for CSI, while the upper "bull's-eye" is a proxy for CI; and these "bull's-eyes" are separated by a region of > 0.50 PVU. Lastly, the maximum ascent intersects the dendritic growth zone within a region of 80+% relative humidity.

Finally, the "messy band" type of "transient band" is discussed in the context of Case 9 at 2100 UTC 14 Dec 2003 (Fig. 3.22). Once again, there is a decoupled area of weak (≤ 2 K (100 km)$^{-1}$ (3 h)$^{-1}$) frontogenesis with barely-tilted ascent. For both EPV* formulations, there is a deep WMSS and negative EPV* region with a "bull's-eye" co-located with the band's surface position. Also, the geostrophic formulation yields a much larger, much more negative area of EPV*. CI may play a role, as evident by the slightly overturned θ_e^* contours. In addition, an along-band cross section at 2100 UTC 14 Dec 2003 (Fig. 3.23) shows along-band stability variations, indicating that this band is not two-dimensional. Lastly, once again, the maximum ascent intersects the dendritic growth zone within a region of 80–90+% relative humidity.

3.4.1.4 Bandlets

The "bandlets" mode is found in Cases 2, 6, 7, 8, 9, 11, 12, 13, 15, 16, 17, and 20 (Table II), and CI plays an important role in almost all of the examples. Regardless, Cases 2, 8, and 16 have a "classic band"-like cross section where CI may not play a role,

and Cases 9 and 13 have "broken-band"-like cross sections. These exceptions will be discussed at the end of this section.

The "bandlets" examples exhibit widely varying frontogenesis, ascent, and EPV* patterns. However, all but one (Case 15) have CI, which distinguishes these cases from "uniform" ones, where the stability is varied but the frontogenesis is a clue to the mode. Some "bandlets" cases have thin, weak frontogenesis, while others have ~ 4 K $(100\ km)^{-1}$ $(3\ h)^{-1}$ of more moderately sloping frontogenesis. Yet, the frontogenesis is almost always surface-based, and it is the CI that distinguishes the cross-section pattern from that of a "uniform" one.

Four of these cases clearly exhibit a form of "downscale development" (Xu 1986) known as the "escalator–elevator" pattern (Neiman et al. 1993), e.g., Case 12 at 0000 UTC 17 Mar 2004 (Fig. 3.24) and Case 17 at 0000 UTC 1 Mar 2005 (Fig. 3.25). Here, forced slantwise ascent (the "escalator"), denoted by the tilted ascent contours, puts air parcels in place for upright ascent (the "elevator") in association with midlevel-based upright convection in an area of CI. In other words, the "escalator" (frontogenetical circulation) raises parcels up to the level of free convection (LFC) of the "elevator" (upright convection).

Other cases do not explicitly show the "escalator–elevator" pattern but its existence may be inferred. For example, in Case 6 at 1500 UTC 17 Feb 2003 (Fig. 3.26) the "escalator–elevator" pattern may be occurring but because the frontal circulation and associated ascent is weak, it may not be as noticeable and pronounced as in Figs. 3.24 and 3.25. It is also observed that cross sections with deeper CI regions have messier patterns of "bandlets" with more elliptical components to the pattern. Lastly, the

maximum ascent again intersects the dendritic growth zone within a region of 80–90+% relative humidity in these cases.

For the cases where the cross sections resemble those of "classic bands," the only differences between them are that the ascent values are ≥ -16 μb s^{-1} (instead of ≤ -16 μb s^{-1}) and the frontogenesis is ≤ 5 K $(100\text{ km})^{-1}$ $(3\text{ h})^{-1}$ [instead of 5–8 K $(100\text{ km})^{-1}$ $(3\text{ h})^{-1}$] above the boundary layer. However, these "classic band"-like cross sections still have "bull's-eyes." Similar to the "classic band"-like "uniform" cross sections, the "bandlets" shield in Case 16 develops into a band once the precipitation shield moves offshore (and so it is not officially classified). Figure 3.27 shows the "bandlets" cross section for Case 16 at 0300 UTC 25 Feb 2005, while Figs. 3.28a–b show the radar for the "bandlets" at 0300 UTC 25 Feb 2005 and for the offshore band at 0900 UTC that day.

Case 13 briefly contains a "broken band" at 0800 UTC 19 Mar 2004 (Fig. 3.29a) before it devolves into "bandlets" (Fig. 3.29b) at the time of the 0900 UTC 19 Mar 2004 cross section (Fig. 3.30). The difference between this cross section and that of a "broken band" is that here the frontogenesis is surface-based. Case 9 also exhibits this type of mode 6 h after the "messy band" observed in Fig. 3.22. At 0300 UTC 15 Dec 2003, the radar (Fig. 3.31) reveals a messy bandlets pattern over New York State, while the cross section (Fig. 3.32) contains a deep layer of CI within the stacked "bull's-eyes." Here, the frontogenesis pattern is a blend of "transient band" and "bandlets" ones: while the frontogenesis is surface-based, the two main areas are not vertically aligned, i.e., the upper, more important frontogenesis region is practically decoupled from the surface.

3.4.1.5 Fractured

The "fractured" mode is found in Cases 4, 12, 16, and 17 (Table II). It features weak [$\leq$ 2 K (100 km)$^{-1}$ (3 h)$^{-1}$], fragmented areas of frontogenesis decoupled from the surface, e.g., Case 12 at 1500 UTC 16 Mar 2004 (Fig. 3.33). The one exception is Case 17 at 0900 UTC 1 Mar 2005 (Fig. 3.34), which has no detectable frontogenesis at all. Like Case 12, "fractured" cases have WMSS with areas of negative EPV* associated with either CSI or CI above their frontal zones, and, similar to previous modes, EPV^{*}_{g} features more negative stability values. In addition, stability appears to be reduced in the vicinity of the frontogenesis fragments. Once again, ascent intersects the dendritic growth zone, but its maximum values are where the relative humidity is closer to 70–80+%, which is less than for the other modes.

3.4.2 Solo Light Snowbands

These snowbands (Table IV), while included in the unclassifiable bin, have their own unique cross-section signatures. The solo snowbands in Cases 2 and 12 are associated with weak, localized frontogenesis in the middle and upper troposphere, e.g., Case 12 at 1200 UTC 16 Mar 2004 (Fig. 3.35). These cases have WMSS and negative EPV* for both formulations. The ascent is weak (> -8 μb s^{-1}), and while it does intersect the dendritic growth zone, its maximum values are in a region of 70–80+% relative humidity. For Case 17 at 0900 UTC 1 Mar 2005 (Fig. 3.36), the solo band is not in advance of a main precipitation shield; rather, it is to the rear of one. Here, an elevated layer of CSI and CI co-located with -8 μb s^{-1} ascent may indicate some sort of instability

roll, or the NARR model may not have properly resolved a small area of frontogenesis in the region of the snowband.

TABLE II. Modes in each case, along with 3-h times corresponding to the NARR analyses when they are present.

Case	Mode	Time & Date
1	Uniform	0900–1500 UTC 27 Nov 2002
2	Bandlets	2100 UTC 5 Dec 2002
4	Fractured	1500 UTC 3 Jan–0900 UTC 4 Jan 2003
5	Uniform	1200–1500 UTC 7 Feb 2003
	Classic Band	1800–2100 UTC 7 Feb 2003
6	Transient Band	1200–2100 UTC 16 Feb 2003
	Uniform	0600 UTC 17 Feb 2003
	Bandlets	1500–2100 UTC 17 Feb 2003
7	Uniform	1500 UTC 6 Mar 2003
	Classic Band	1800 UTC 6 Mar 2003
	Bandlets	1800 UTC 6 Mar 2003
8	Bandlets	1800 UTC 5 Dec–0000 UTC 6 Dec 2003 1800 UTC 6 Dec–0000 UTC 7 Dec 2003
	Uniform	0900 UTC 6 Dec 2003
	Transient Band	1500–1800 UTC 6 Dec 2003
	Classic Band	0300 UTC 7 Dec 2003
9	Transient Band	2100 UTC 14 Dec 2003
	Bandlets	0000–0900 UTC 15 Dec 2003
10	Uniform	0000–0900 UTC 15 Jan 2004
11	Transient Band	0300 UTC 28 Jan 2004
	Bandlets	0600 UTC 28 Jan 2004
12	Fractured	1500–2100 UTC 16 Mar 2004
	Transient Band	2100 UTC 16 Mar–0300 UTC 17 Mar 2004
	Bandlets	0000 UTC 17 Mar 2004
13	Bandlets	0600–1200 UTC 19 Mar 2004
15	Bandlets	1500–2100 UTC 22 Jan 2005
	Transient Band	0300–0600 UTC 23 Jan 2005
	Uniform	1800–2100 UTC 22 Jan 2005
16	Fractured	1800 UTC 24 Feb 2005
	Uniform	1800–2100 UTC 24 Feb 2005
	Bandlets	0300–0600 UTC 25 Feb 2005
17	Bandlets	2100 UTC 28 Feb–0000 UTC 1 Mar 2005
	Fractured	0300–1500 UTC 1 Mar 2005
18	Uniform	2100 UTC 8 Mar–0600 UTC 9 Mar 2005
20	Bandlets	0000–0600 UTC 24 Mar 2005

TABLE III. Unclassifiable portions of cases, along with 3-h times corresponding to the NARR analyses when they are present, and brief reasons why they are unclassifiable.

Case	Time & Date	Reason for no classification
2	1500–1800 UTC 5 Dec 2002	Blobs
4	0900–1500 UTC 4 Jan 2003	Hybrid: Evolving band/ Bandlets/Fractured?
6	0900–1200 UTC 17 Feb 2003	Bright banding?
	1200 UTC 17 Feb 2003	Grainy
9	1200 UTC 15 Dec 2003	Hybrid band: Transient/Classic?
11	1800–2100 UTC 27 Jan 2004	Squall line
14	Entire case: 0000–2000 UTC 20 Jan 2005	Grainy
15	0000–0900 UTC 23 Jan 2005	Gravity waves?
	1200–1500 UTC 23 Jan 2005	What type of band? Fractured?
19	Entire case: 0600 UTC 12 Mar–0600 UTC 13 Mar 2005	Grainy

TABLE IV. Solo light snowbands, along with the 3-h times corresponding to the NARR analyses when they are present.

Case	Time/Date
2	1200–1500 UTC 5 Dec 2002
12	0900–1200 UTC 16 Mar 2004
17	0900 UTC 1 Mar 2005

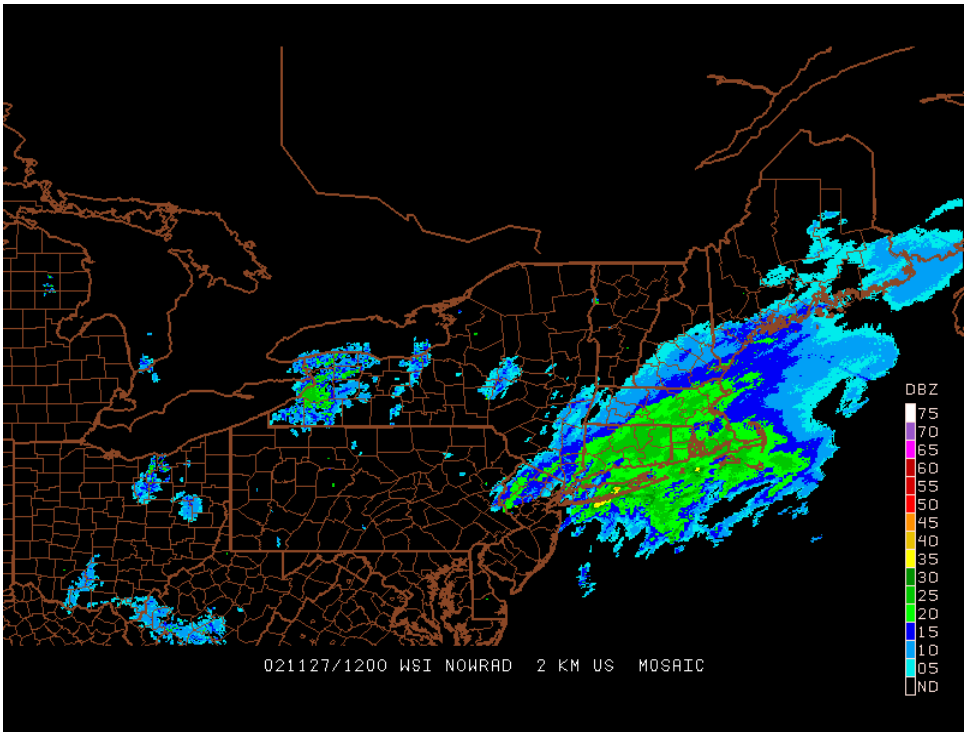

Fig. 3.1. WSI NOWrad mosaic of composite reflectivity at 1200 UTC 27 Nov 2002 (color scale to the right of the image, every 5 dB*Z*).

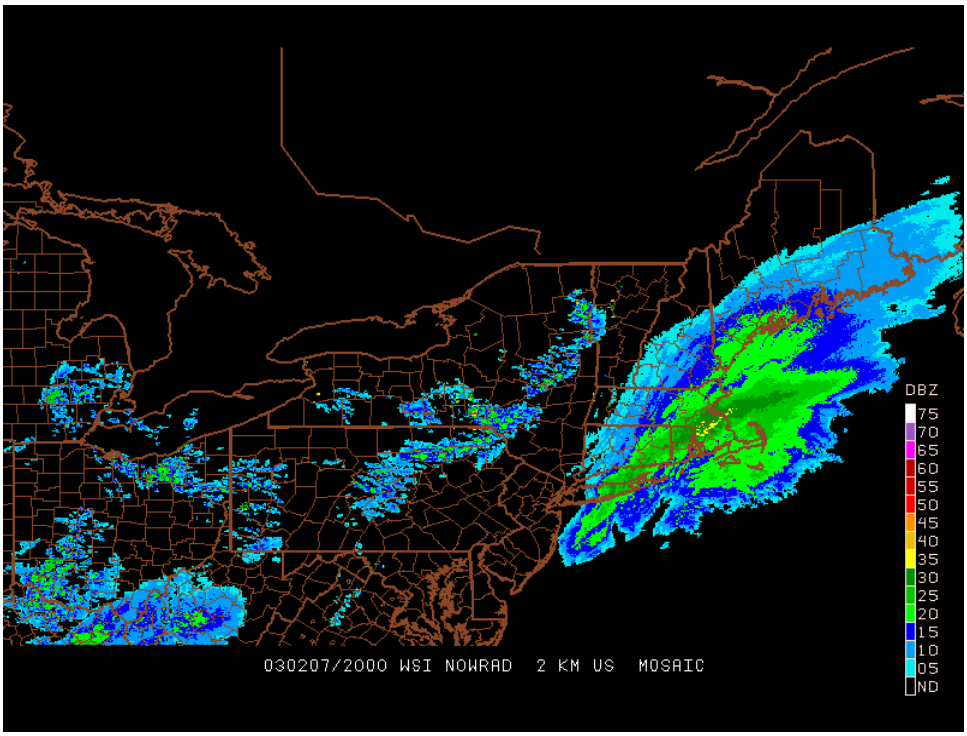

Fig. 3.2. Same as Fig. 3.1 except at 2000 UTC 7 Feb 2003.

(a)

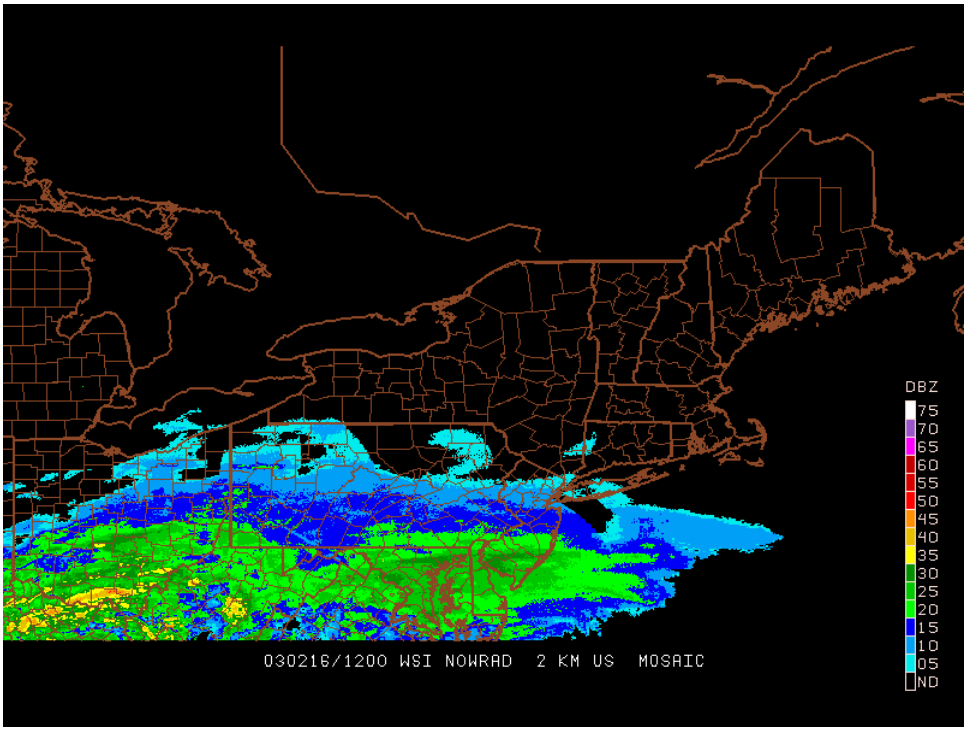

(b)

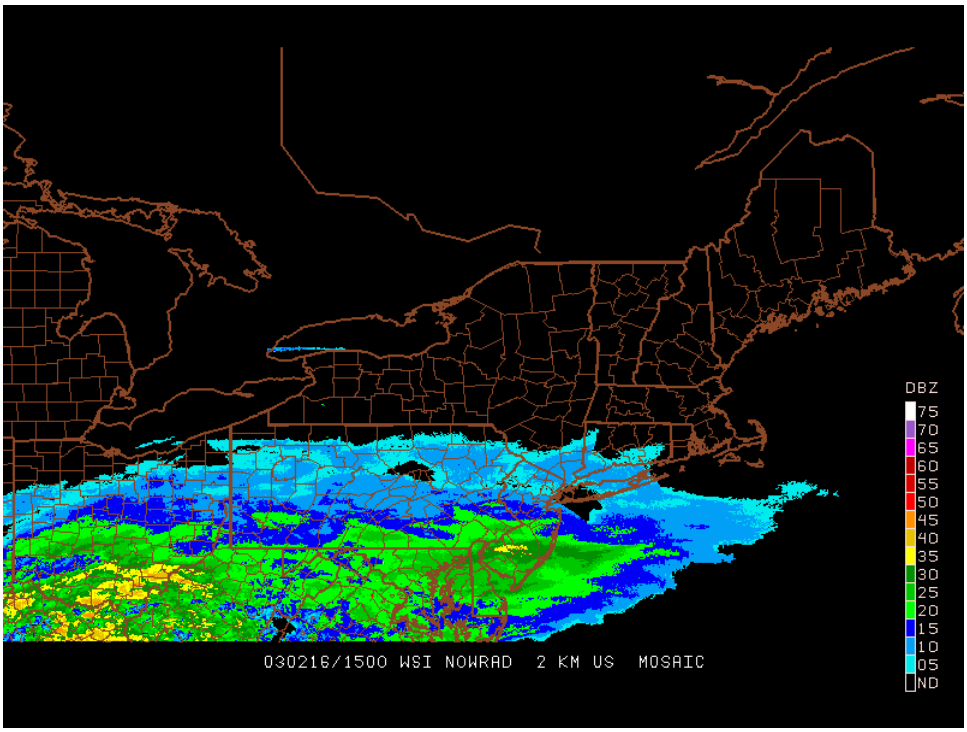

Fig. 3.3. Same as Fig. 3.1 except at (a) 1200 UTC, (b) 1500 UTC, (c) 1800 UTC, and (d) 1915 UTC 16 Feb 2003.

(c)

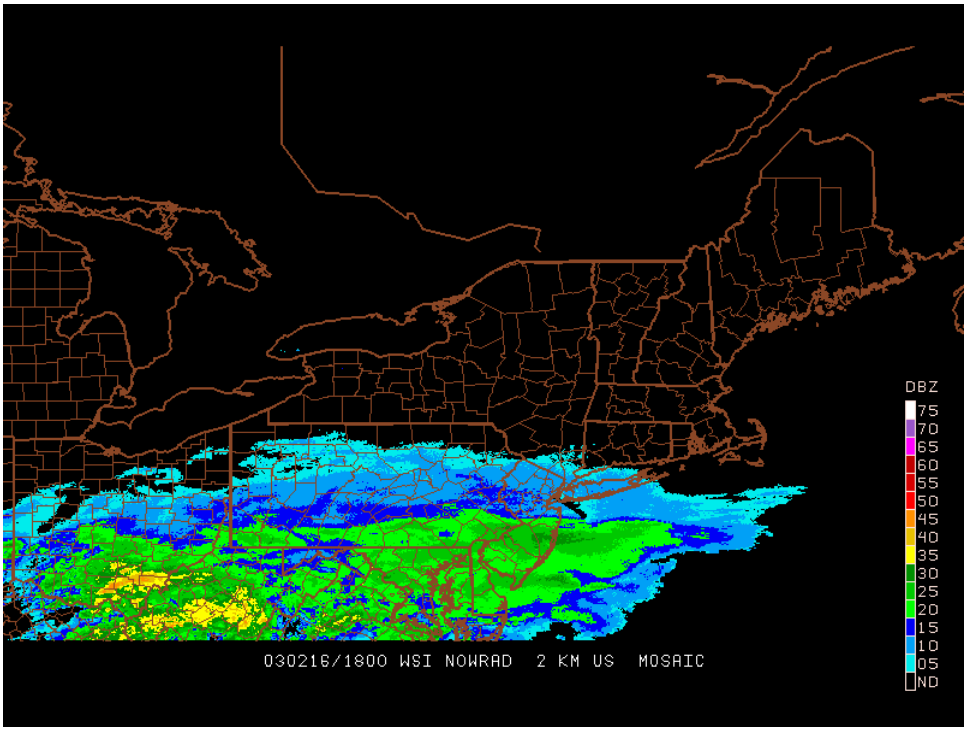

(d)

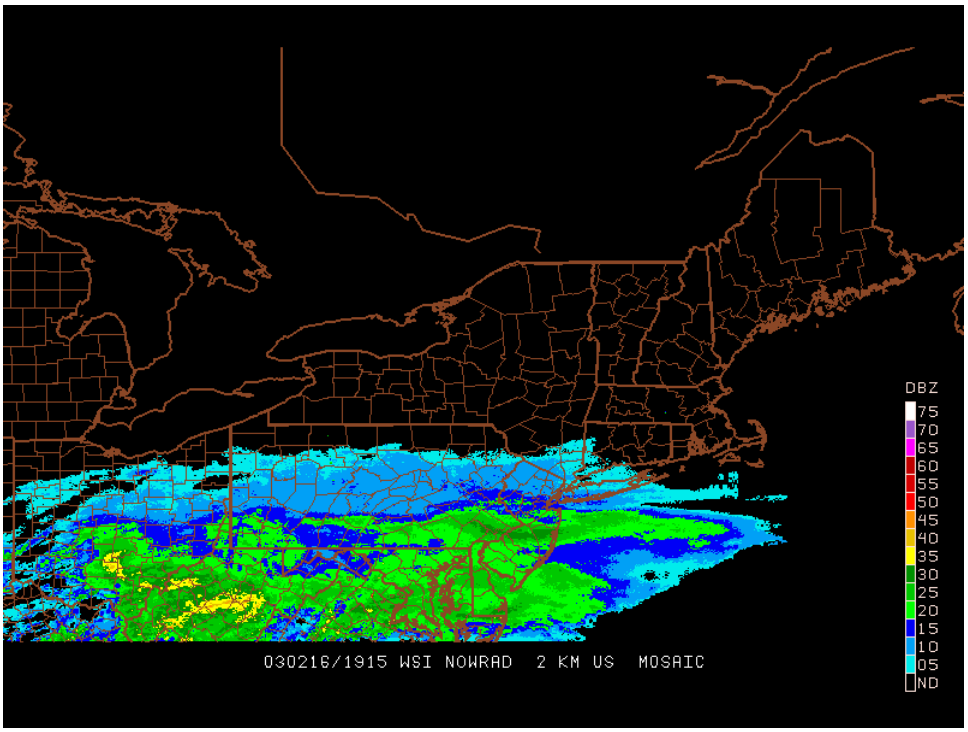

Fig. 3.3. (*Continued*)

(a)

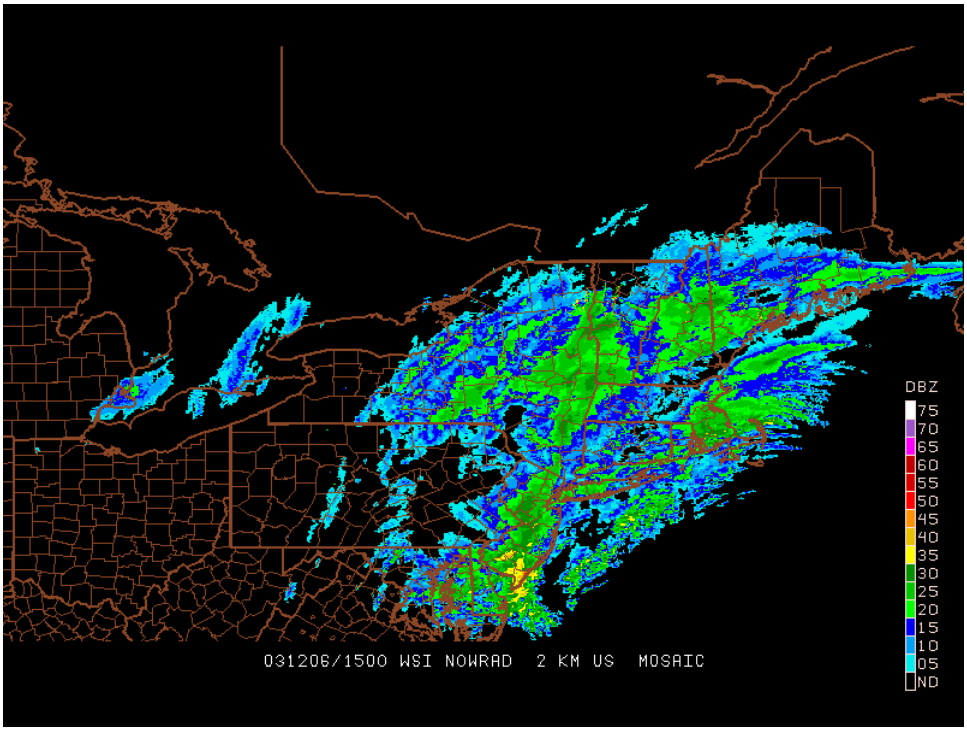

(b)

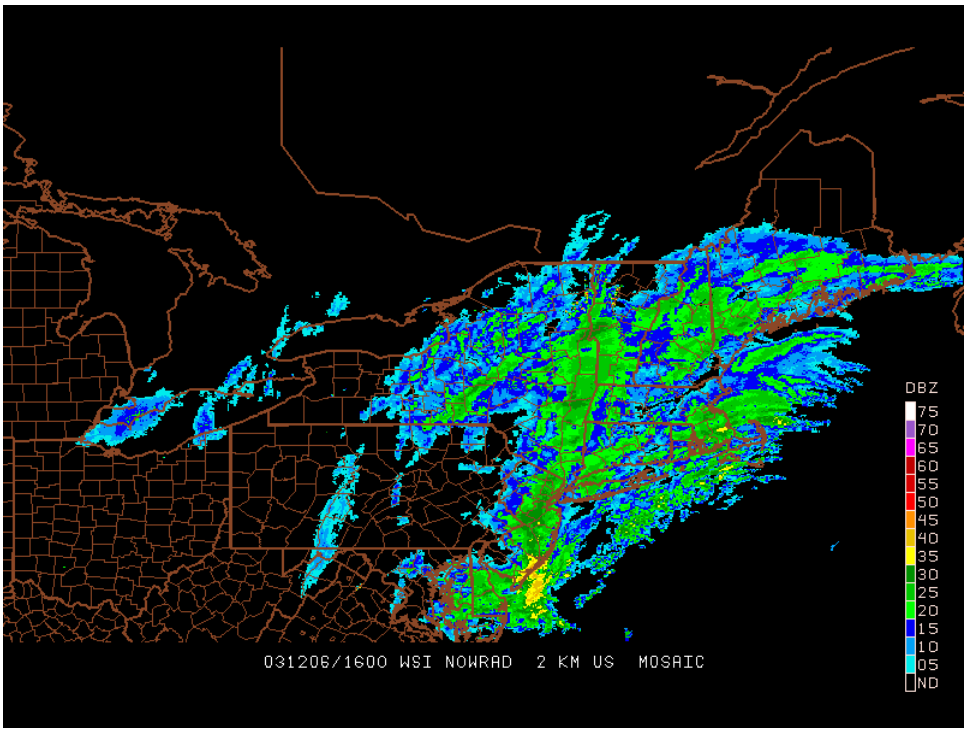

Fig. 3.4. Same as Fig. 3.1 except at (a) 1500 UTC and (b) 1600 UTC 6 Dec 2003.

(a)

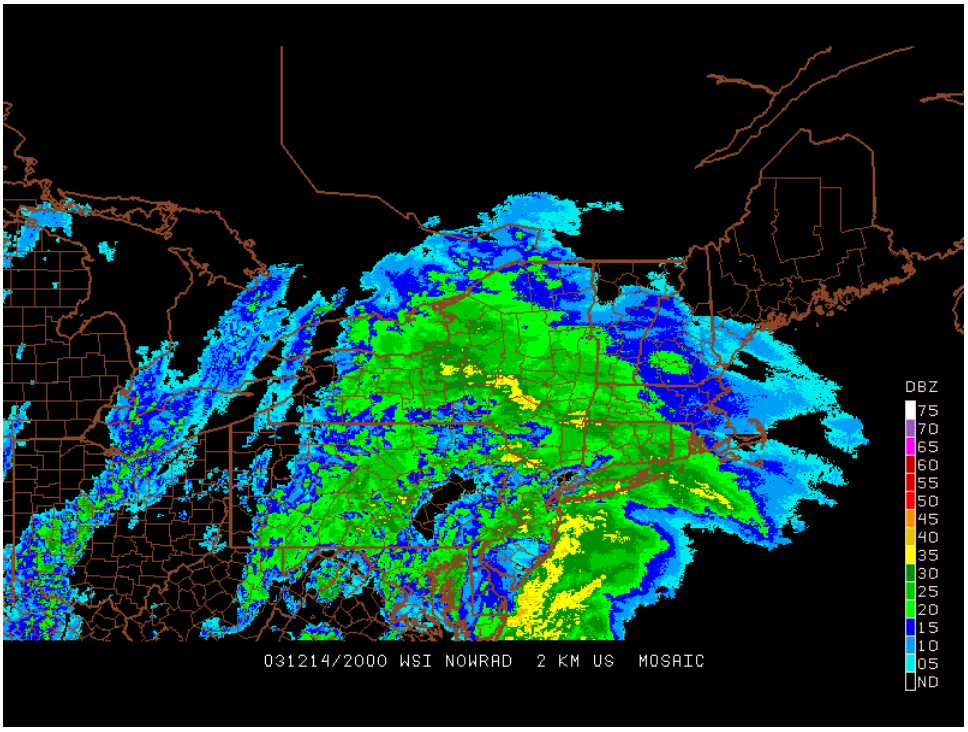

(b)

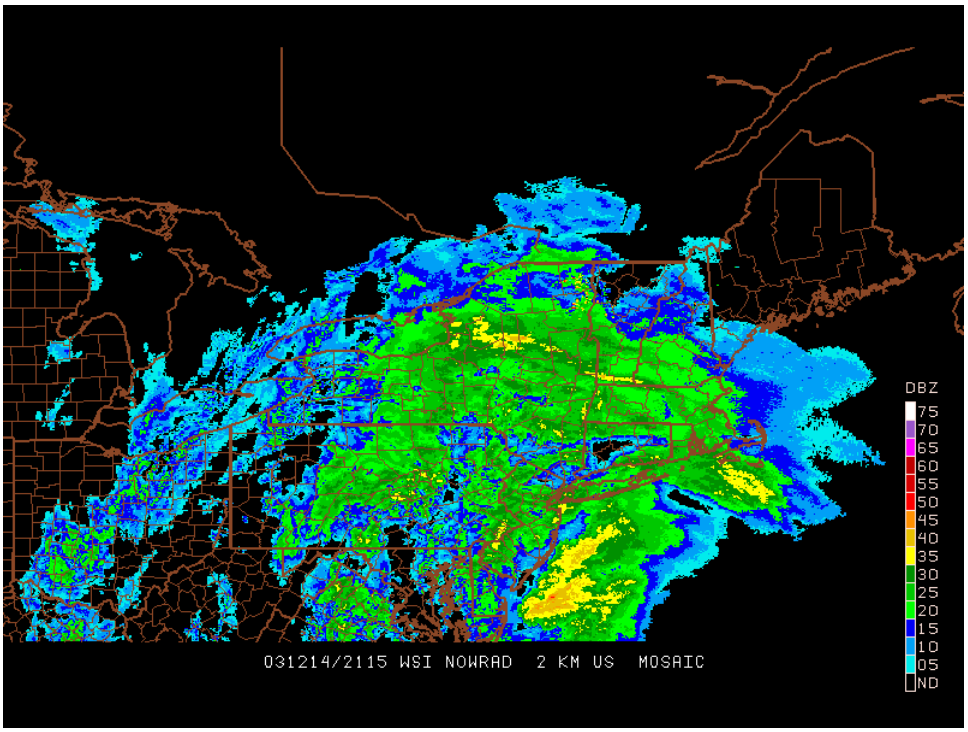

Fig. 3.5. Same as Fig. 3.1 except at (a) 2000 UTC and (b) 2115 UTC 14 Dec 2003.

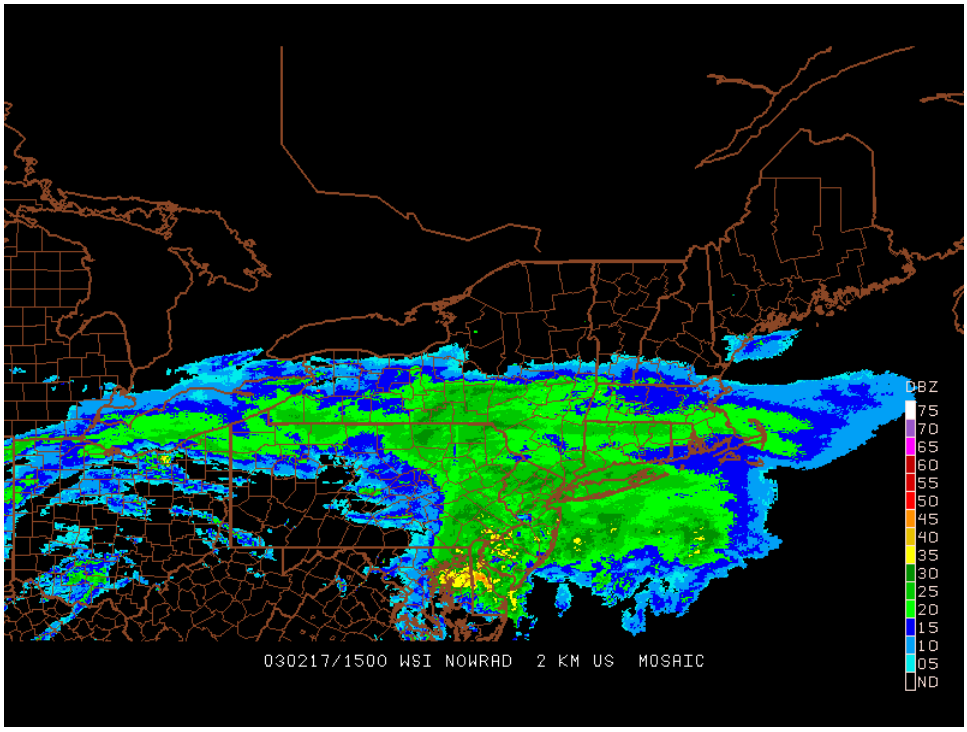

Fig. 3.6. Same as Fig. 3.1 except at 1500 UTC 17 Feb 2003.

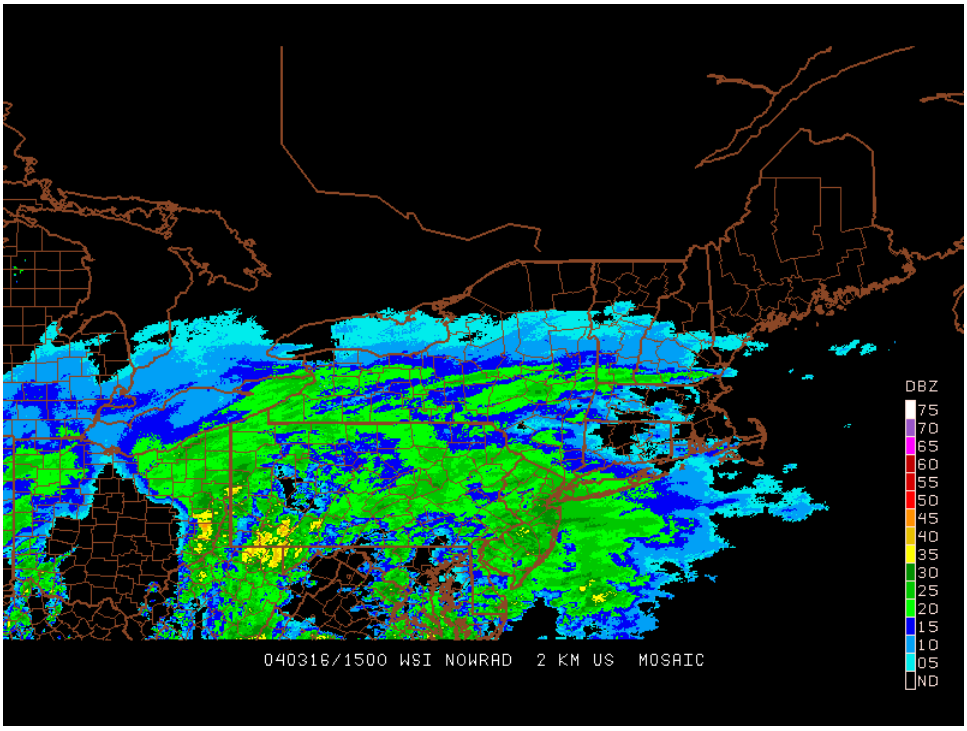

Fig. 3.7. Same as Fig. 3.1 except at 1500 UTC 16 Mar 2004.

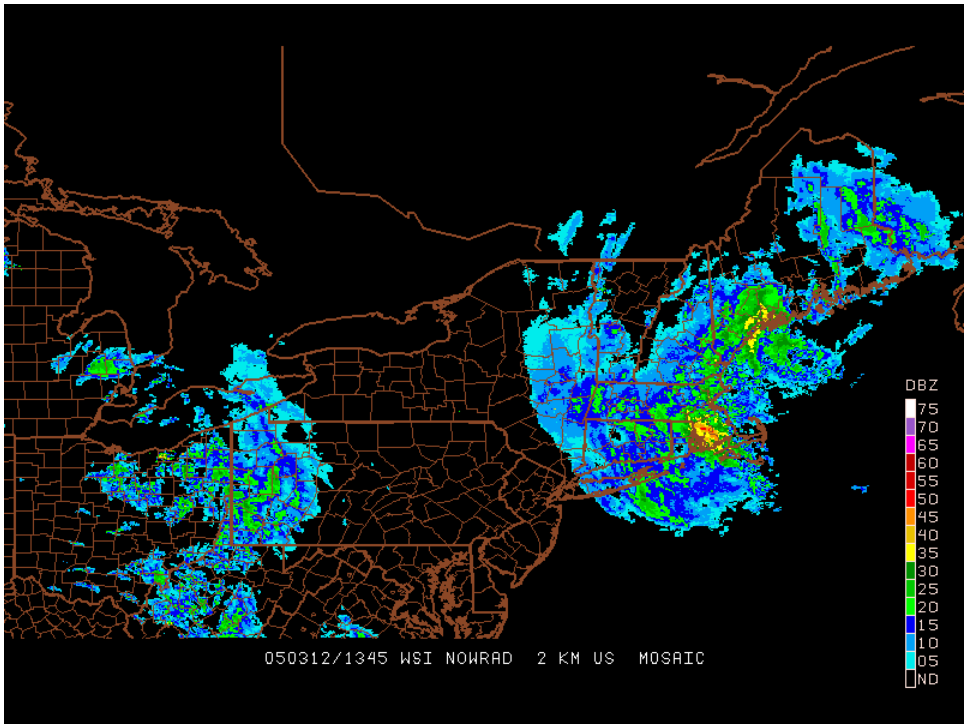

Fig. 3.8. Same as Fig. 3.1 except at 1345 UTC 12 Mar 2005.

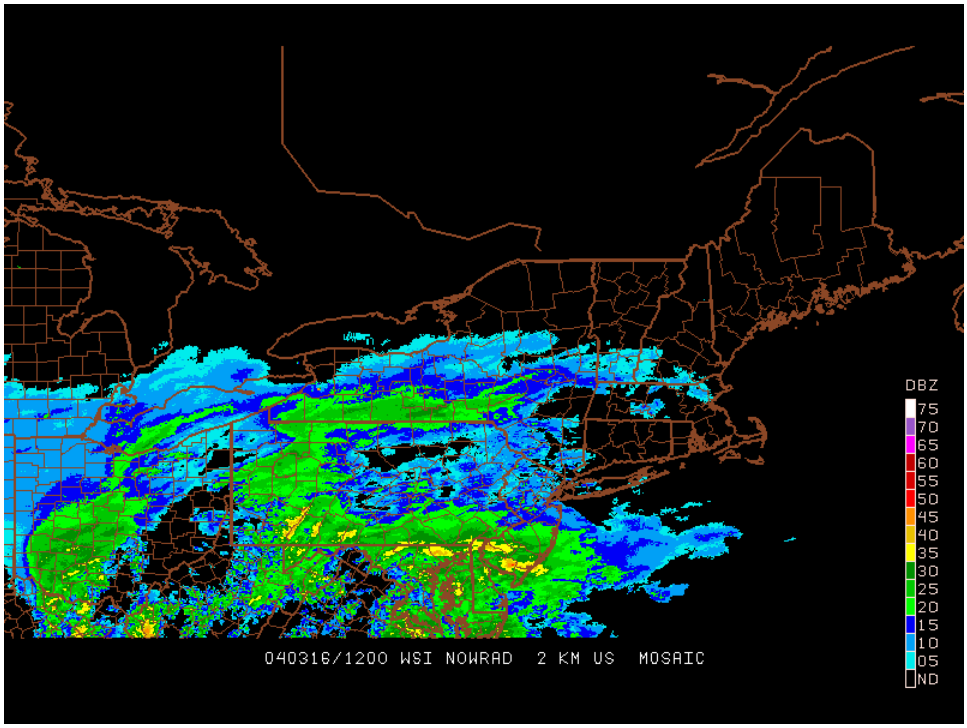

Fig. 3.9. Same as Fig. 3.1 except at 1200 UTC 16 Mar 2004.

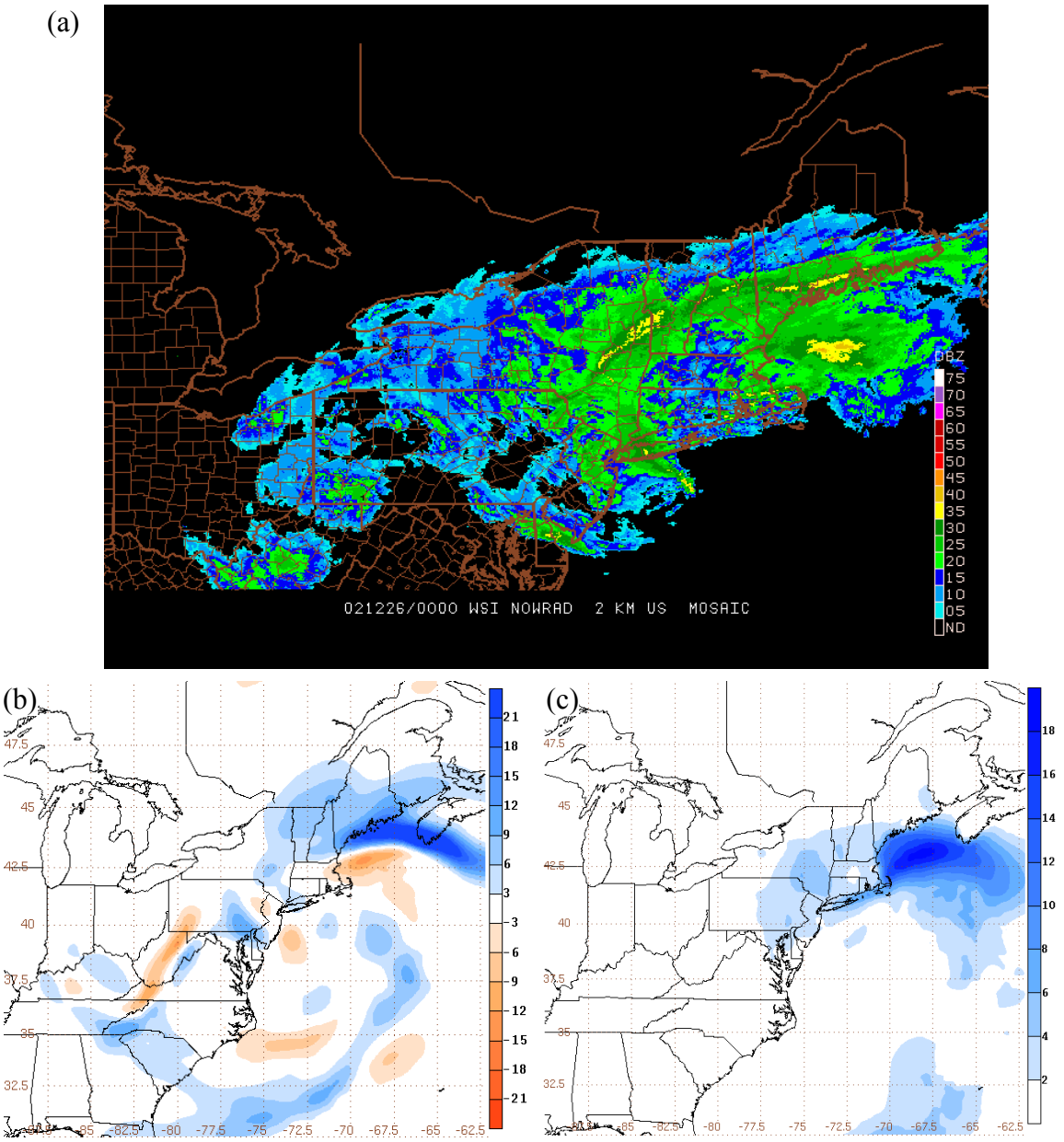

Fig. 3.10. (a) Same as Fig. 3.1 except at 0000 UTC 26 Dec 2002, (b) 700–650 hPa layer-averaged frontogenesis [color scale to the right of the image, every 3 K (100 km)$^{-1}$ (3 h)$^{-1}$] at 0000 UTC 26 Dec 2002, and (c) NARR 3-h model-derived accumulated precipitation ending 0000 UTC 26 Dec 2002 (color scale to the right of the image, every 2 mm).

(a)

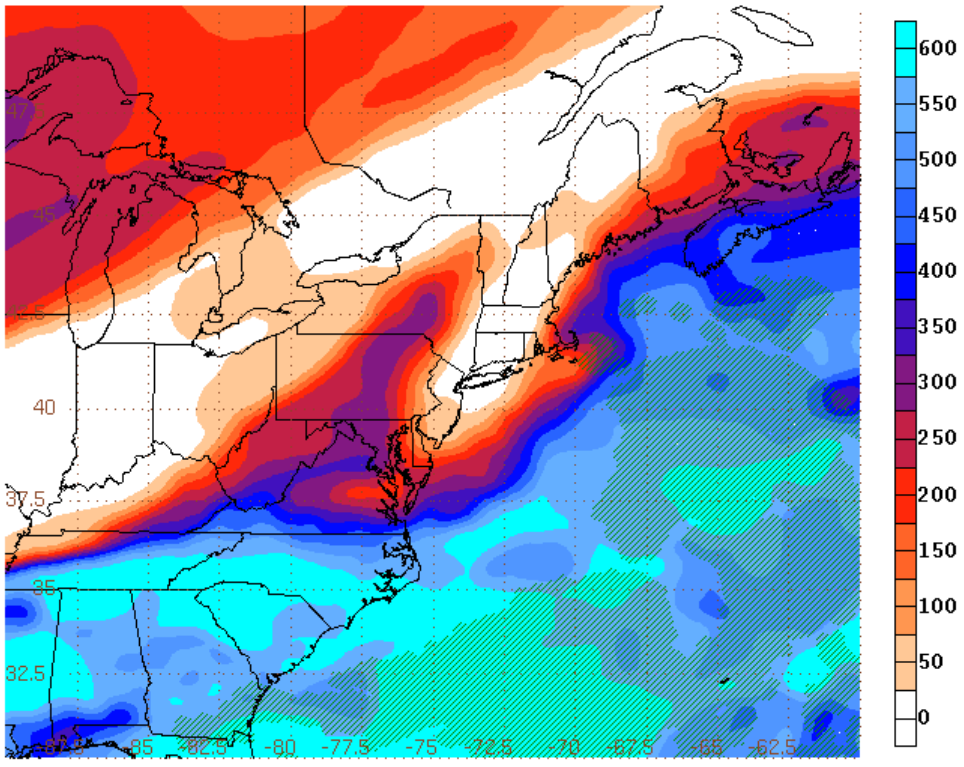

(b)

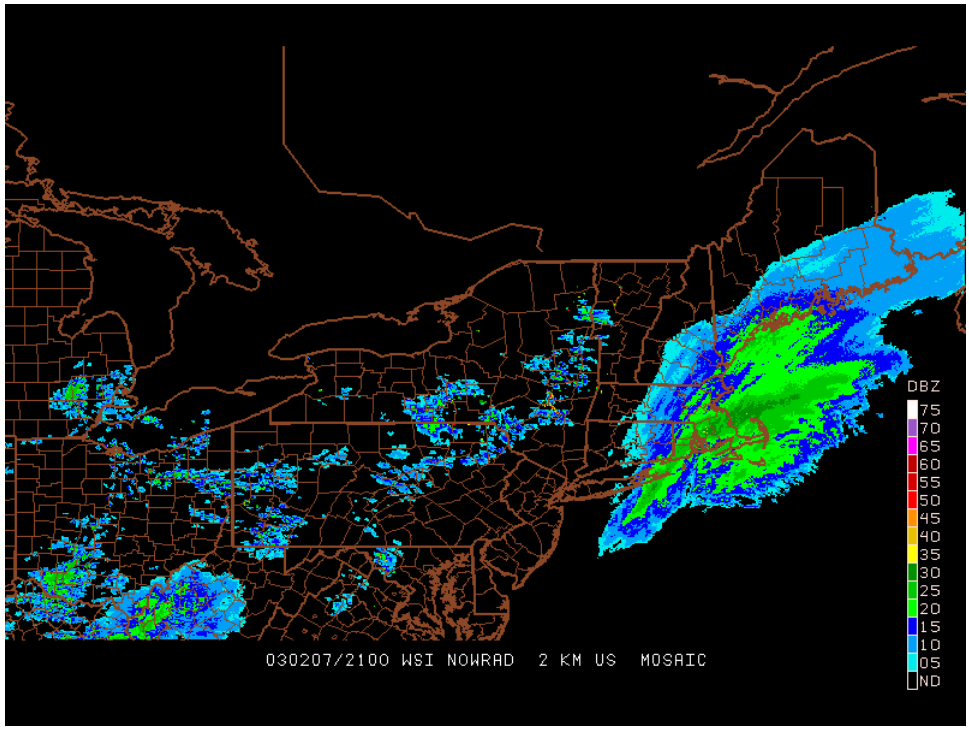

Fig. 3.11. (a) Depth of EPV* < 0.25 PVU (color scale to the right of the image, every 50 hPa) at 2100 UTC 7 Feb 2003; hatching indicates CI. (b) Same as Fig. 3.1 except at 2100 UTC 7 Feb 2003.

(a)

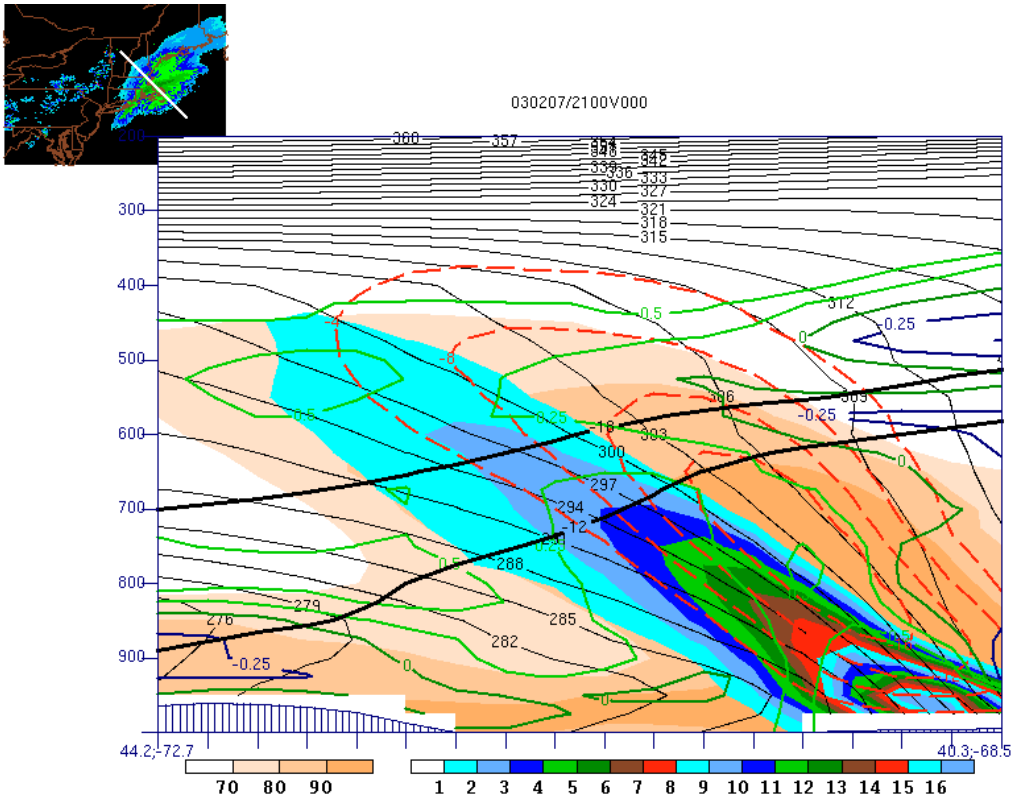
030207/2100V000
44.2,-72.7
40.3,-68.5
70 80 90
1 2 3 4 5 6 7 8 9 10 11 12 13 14 15 16

(b)

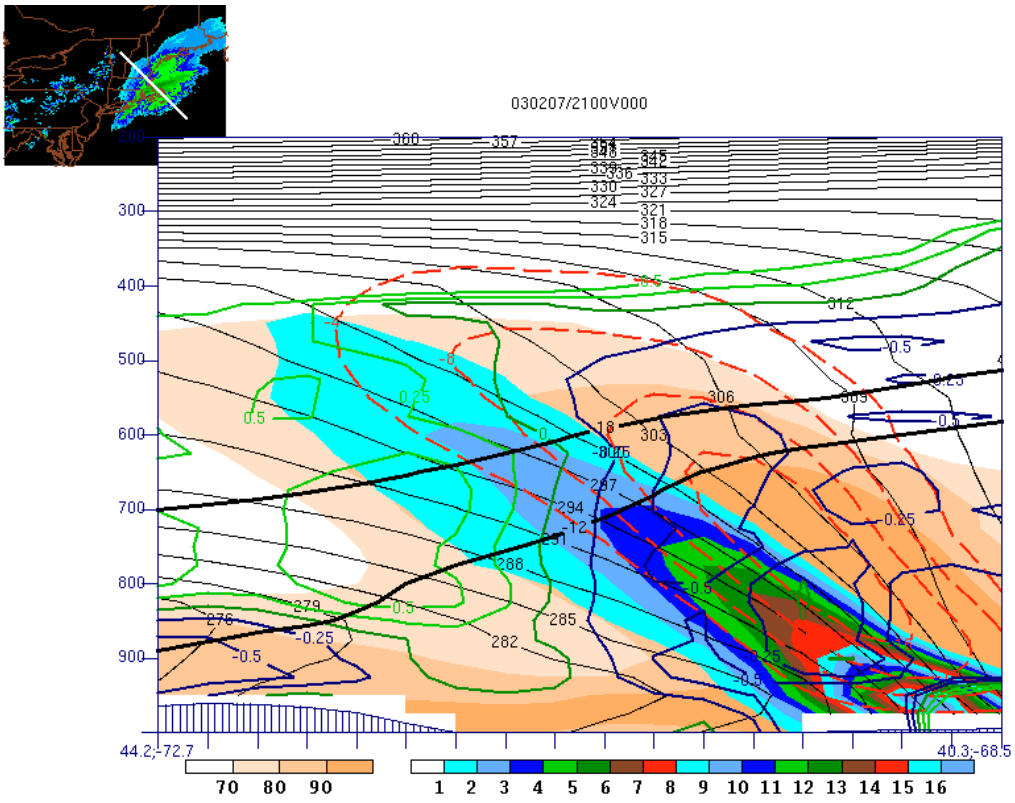
030207/2100V000
44.2,-72.7
40.3,-68.5
70 80 90
1 2 3 4 5 6 7 8 9 10 11 12 13 14 15 16

Fig. 3.12. (a) Upper left: same as Fig. 3.1 except at 2100 UTC 7 Feb 2003, white line indicates cross section slice; Lower right: Saturation equivalent potential temperature (thin black contours, every 3 K), EPV* (green and blue contours, every 0.25 PVU from −0.50 to 0.50 PVU), vertical velocity (red heavy dashed line, every −4 μb s^{-1} starting at −4 μb s^{-1}), −12°C and −18°C isotherms (heavy black lines), relative humidity (color scale to the lower left, every 10%), and 2D frontogenesis [color scale to the lower right, every 1 K $(100\ km)^{-1}$ 3 h^{-1}] at 2100 UTC 7 Feb 2003. (b) Same as Fig. 3.12a except EPV_g^* in place of EPV*.

(a)

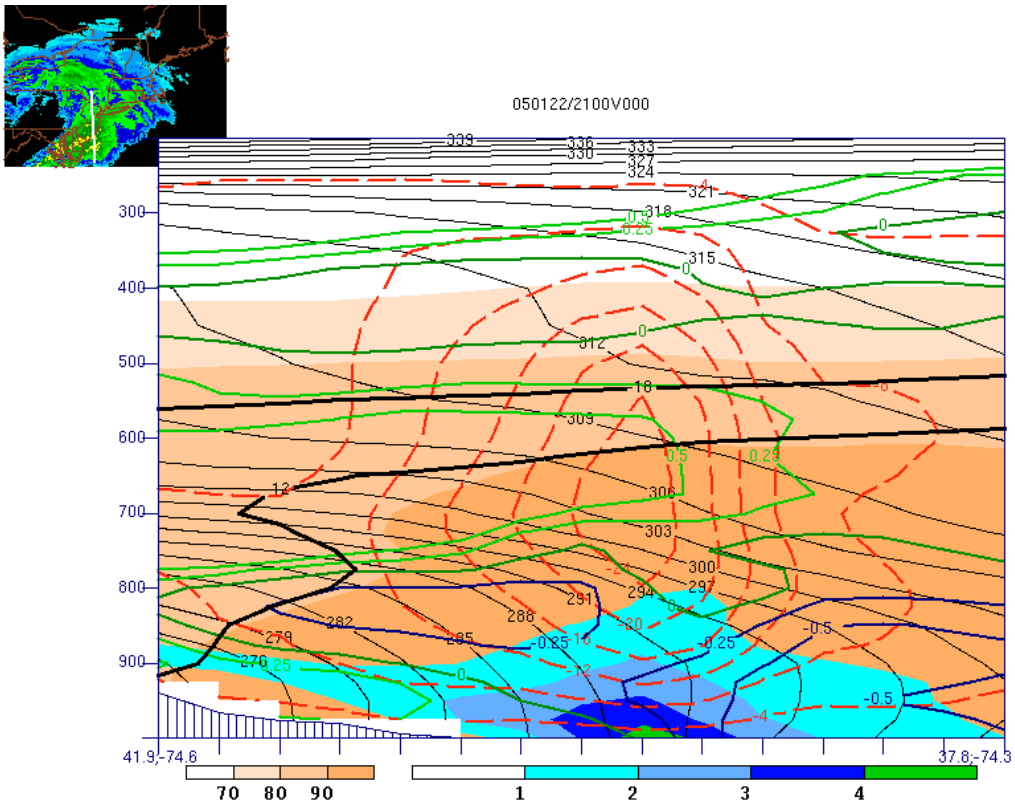

(b)

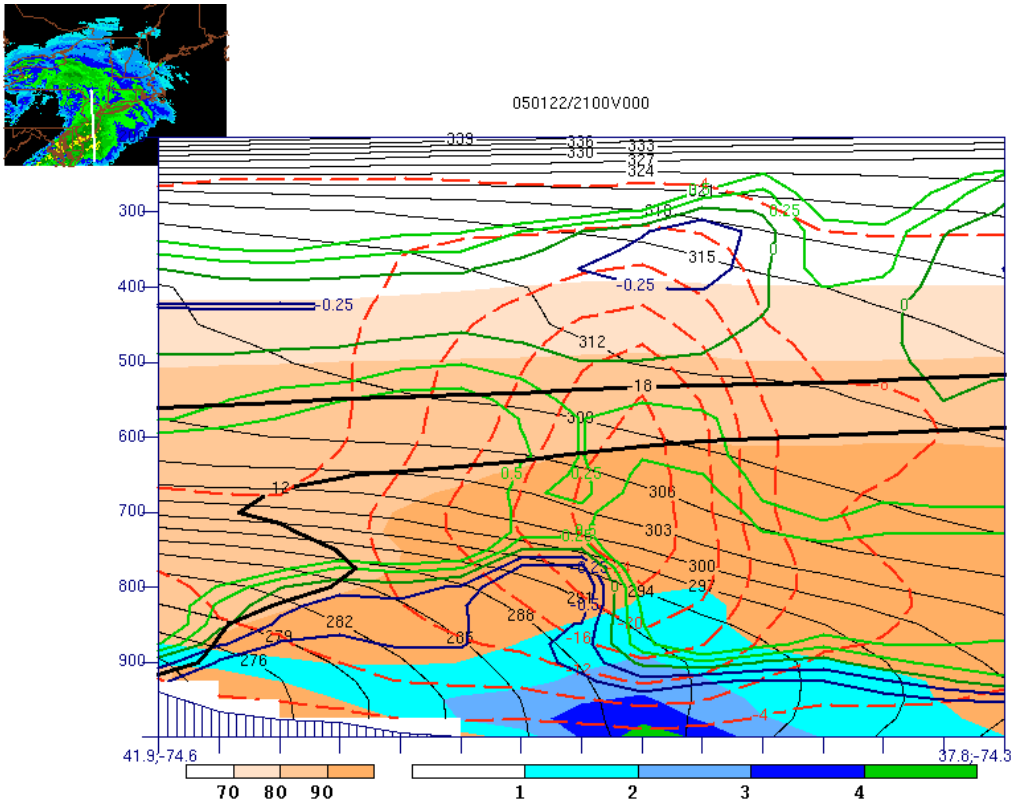

Fig. 3.13. (a–b) Same as Fig. 3.12 except at 2100 UTC 22 Jan 2005.

(a)

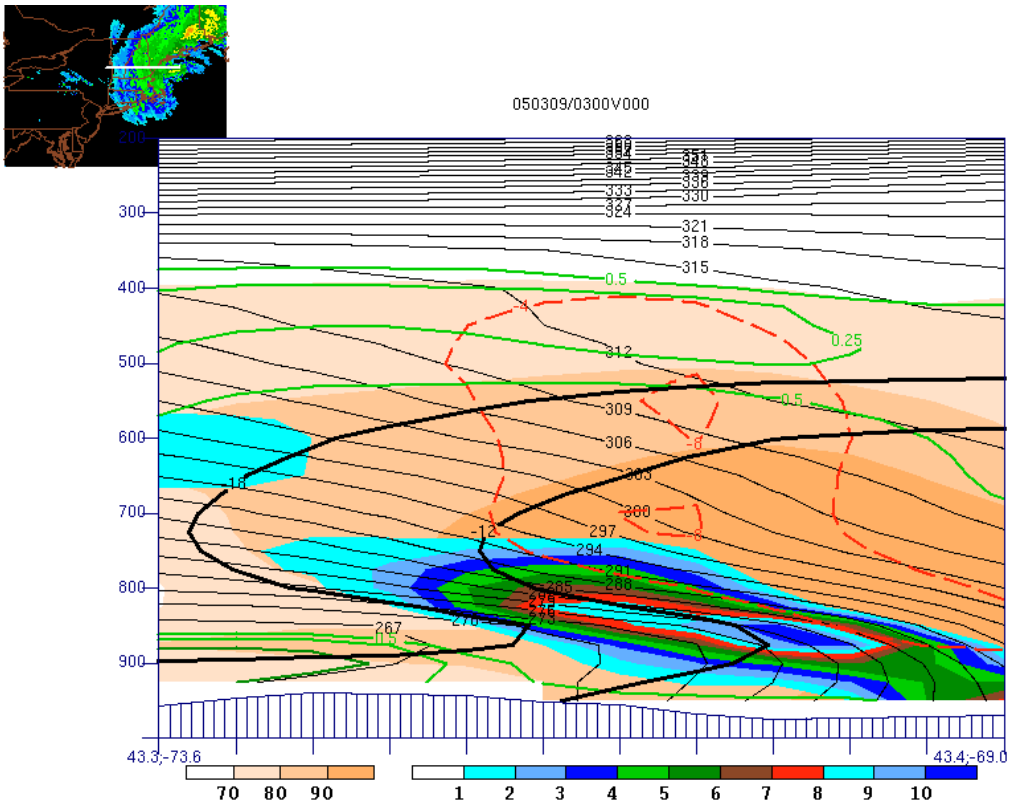

(b)

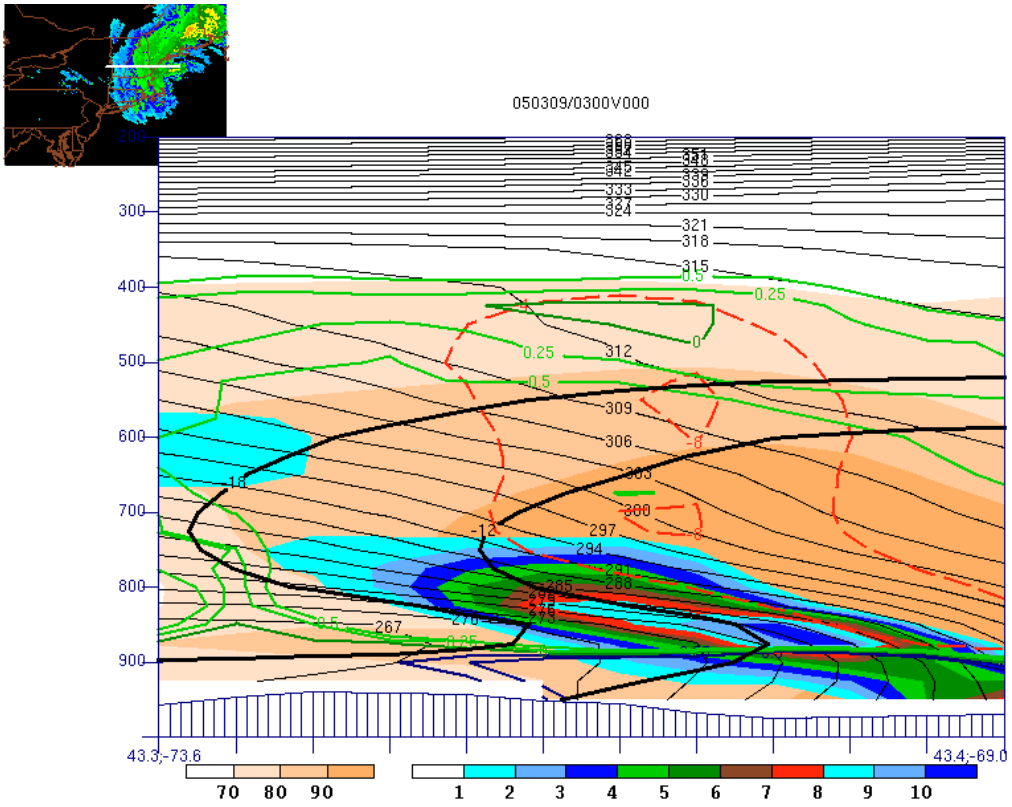

Fig. 3.14. (a–b) Same as Fig. 3.12 except at 0300 UTC 9 Mar 2005.

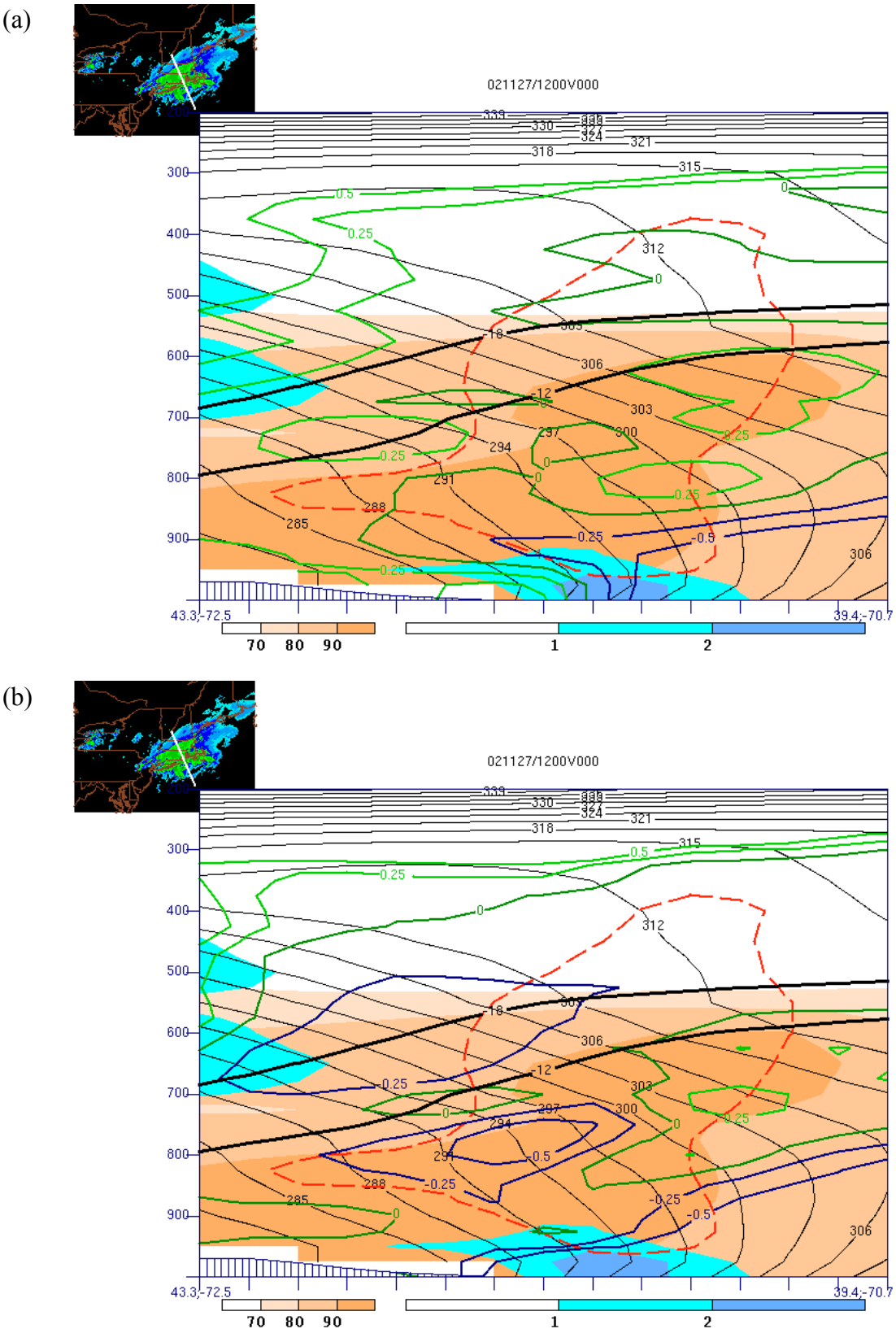

Fig. 3.15. (a–b) Same as Fig. 3.12 except at 1200 UTC 27 Nov 2002.

(a)

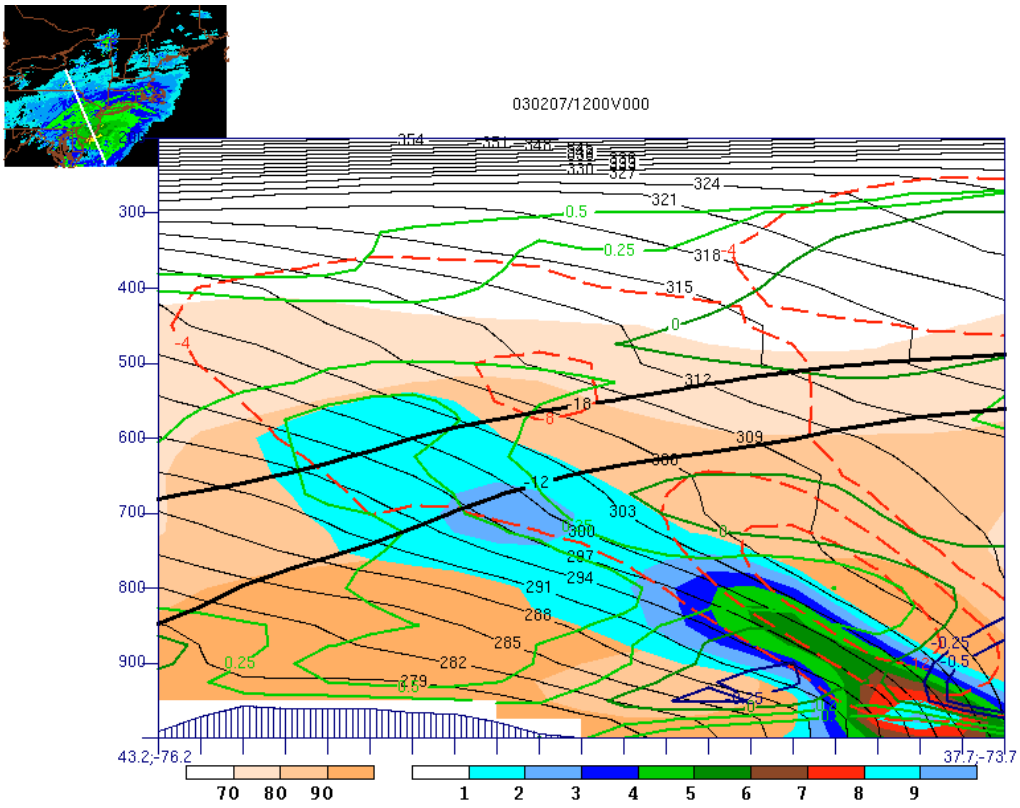

(b)

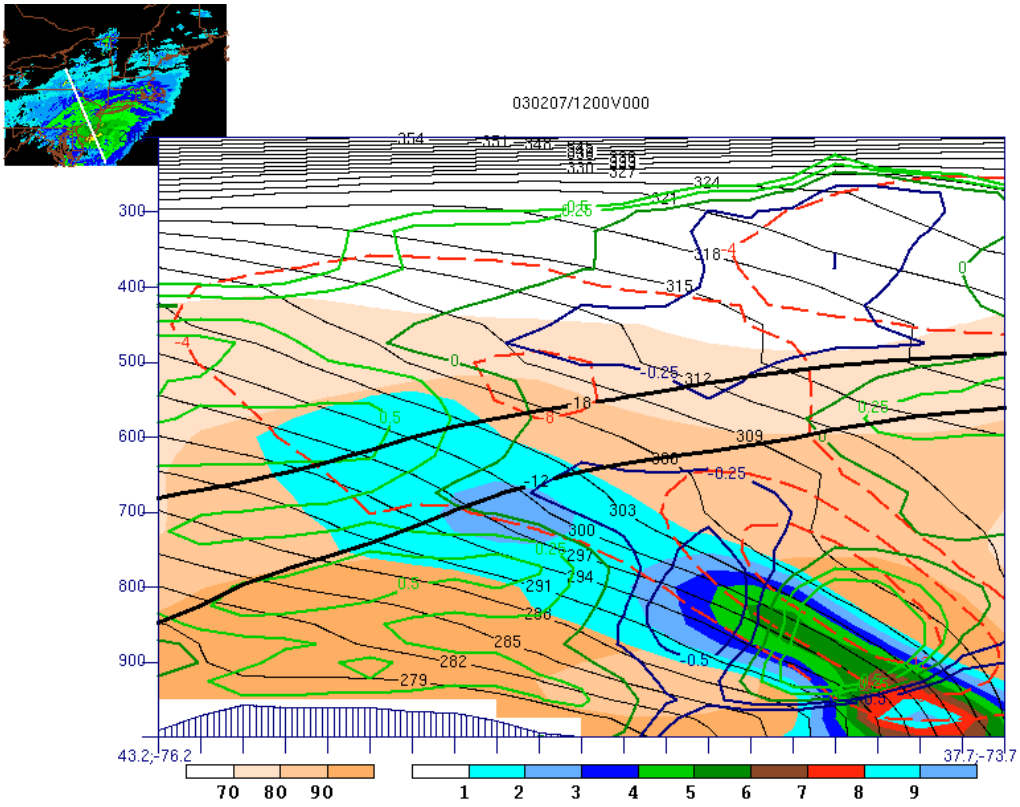

Fig. 3.16. (a–b) Same as Fig. 3.12 except at 1200 UTC 7 Feb 2003.

(a)

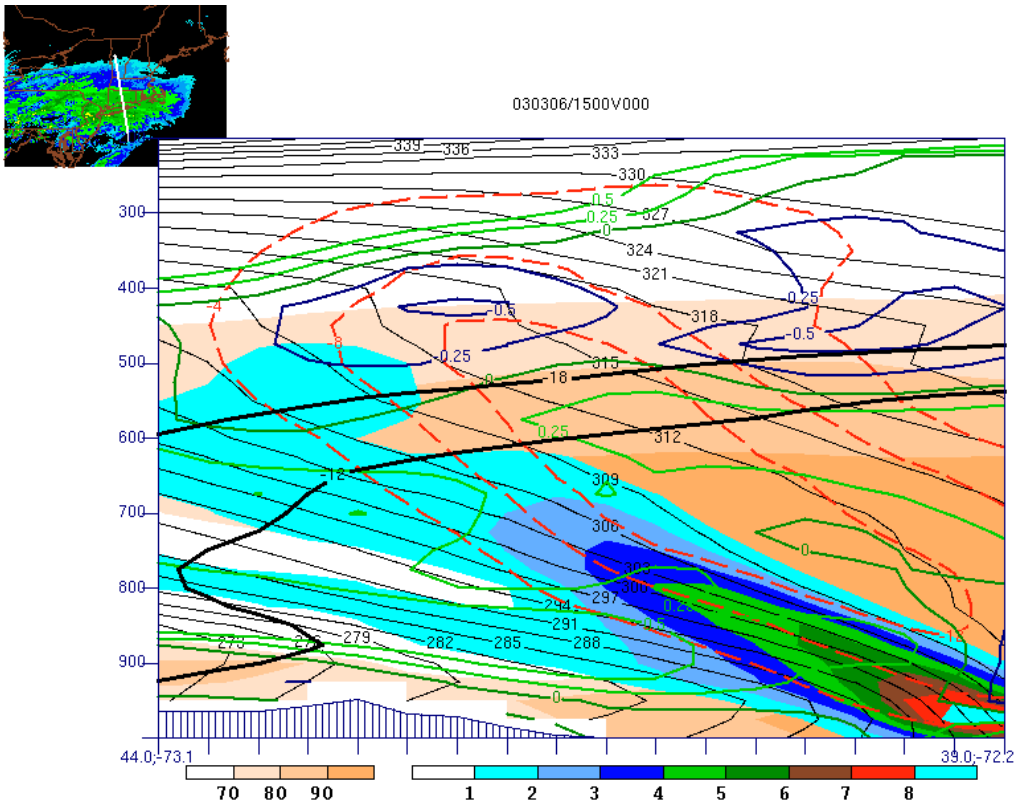

(b)

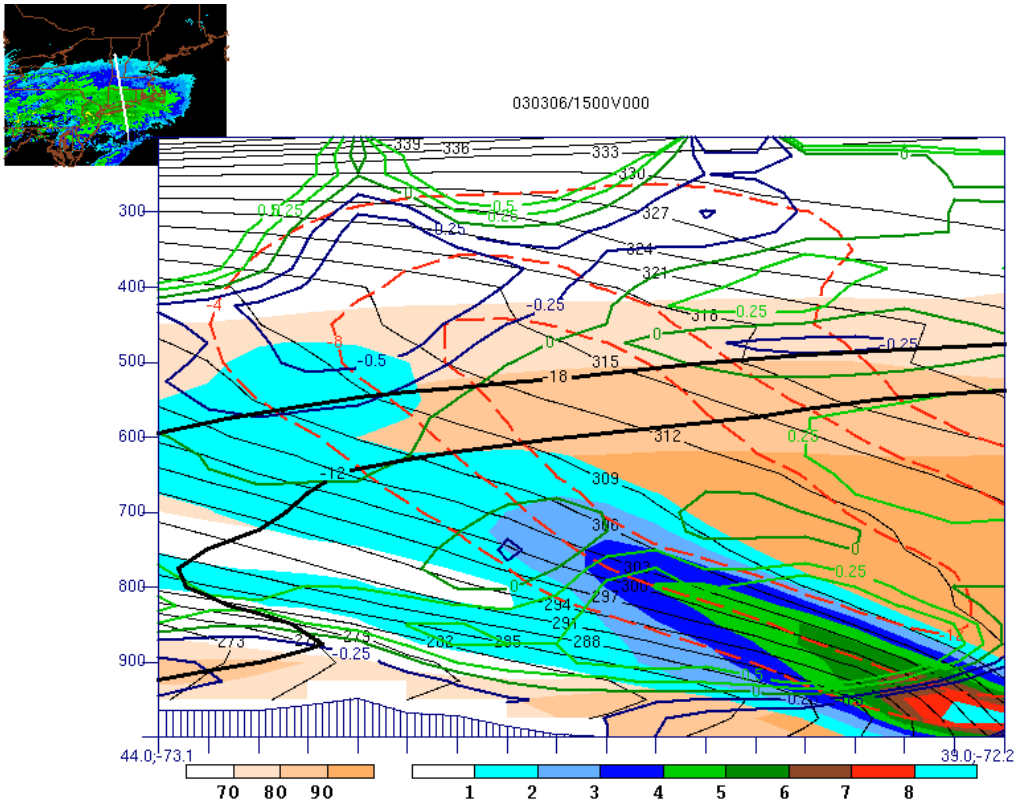

Fig. 3.17. (a–b) Same as Fig. 3.12 except at 1500 UTC 6 Mar 2003.

(a)

(b)

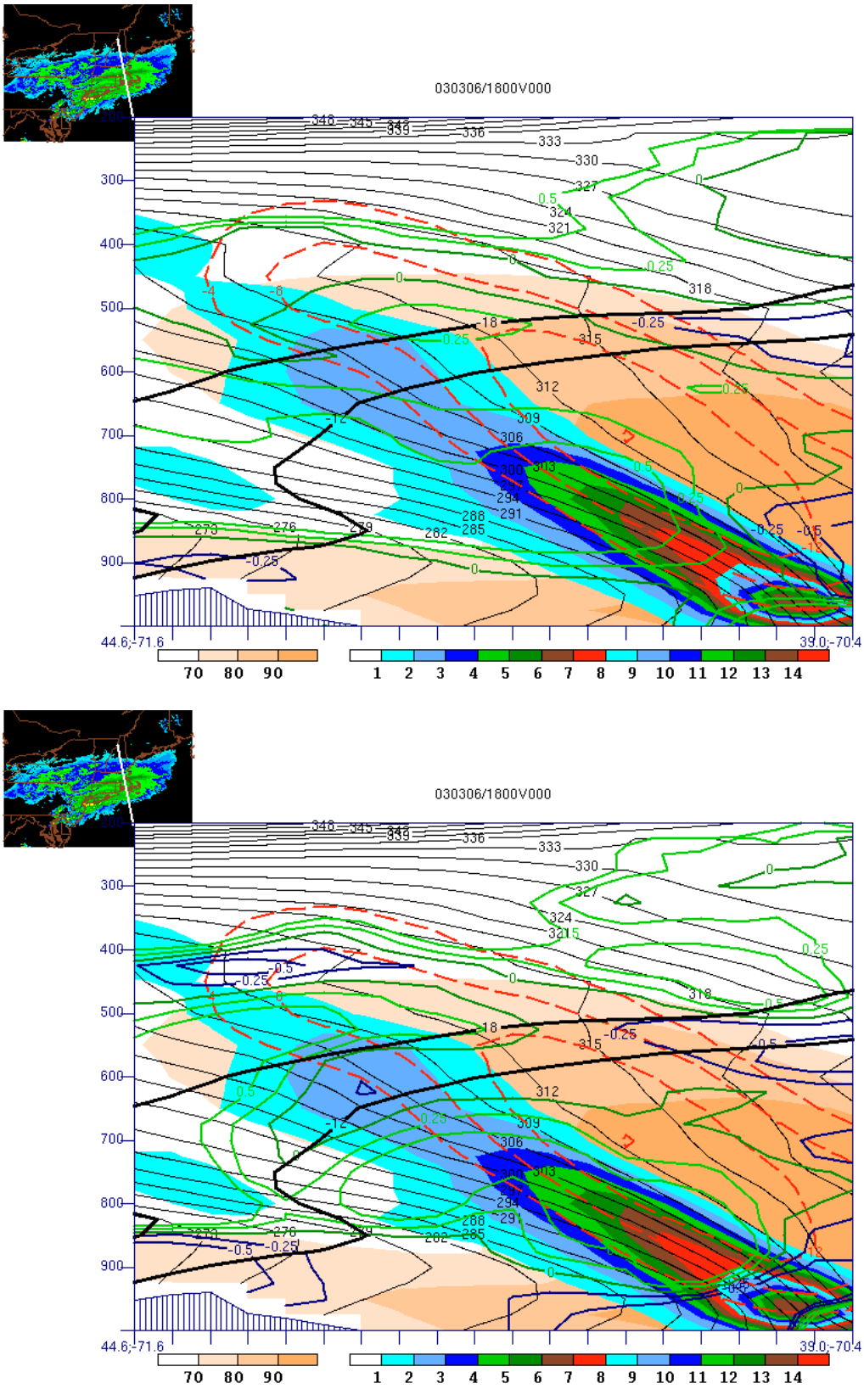

Fig. 3.18. (a–b) Same as Fig. 3.12 except at 1800 UTC 6 Mar 2003.

(a)

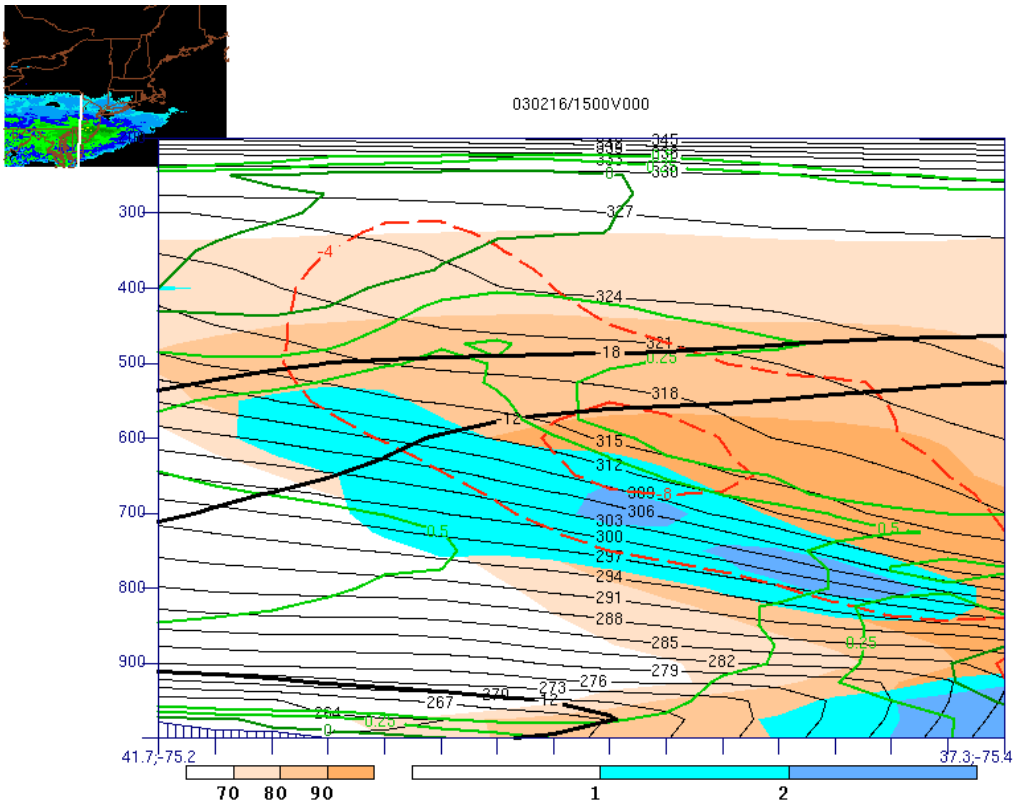

(b)

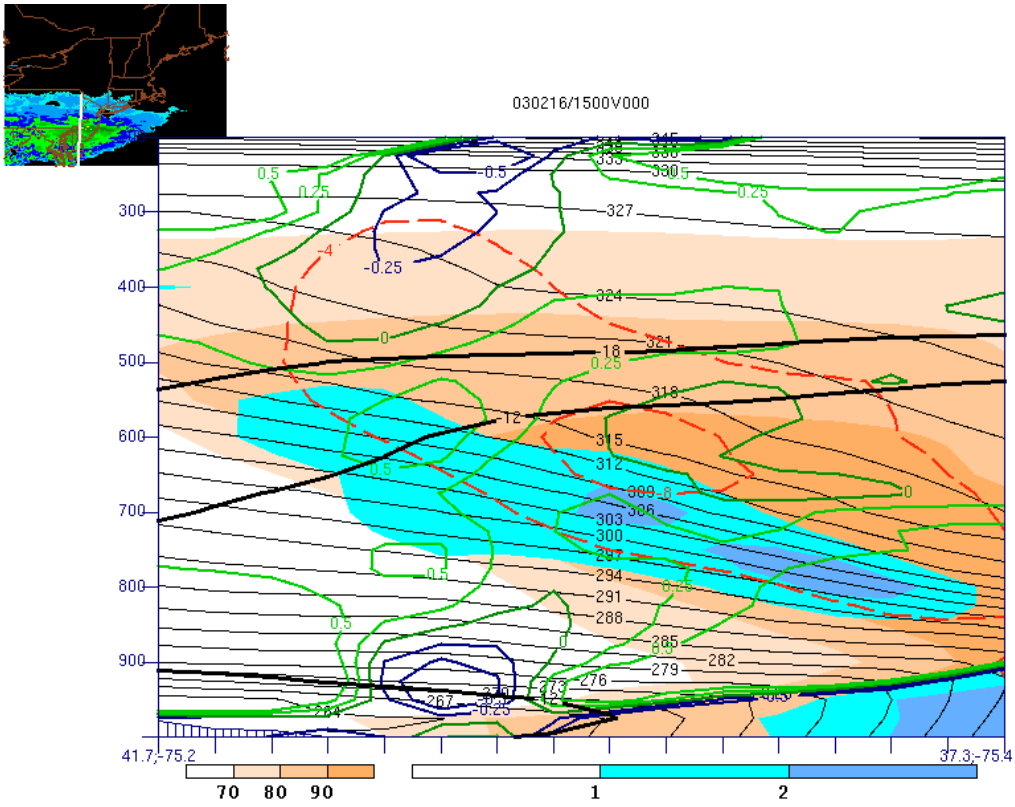

Fig. 3.19. (a–b) Same as Fig. 3.12 except at 1500 UTC 16 Feb 2003.

(a)

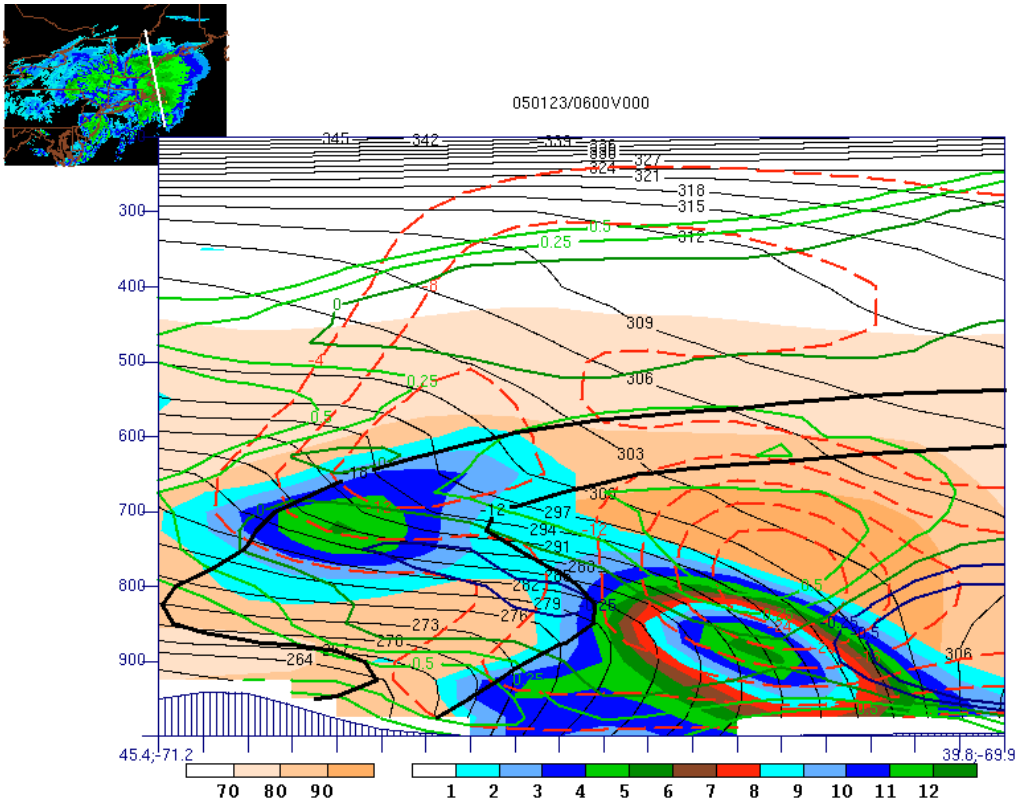

(b)

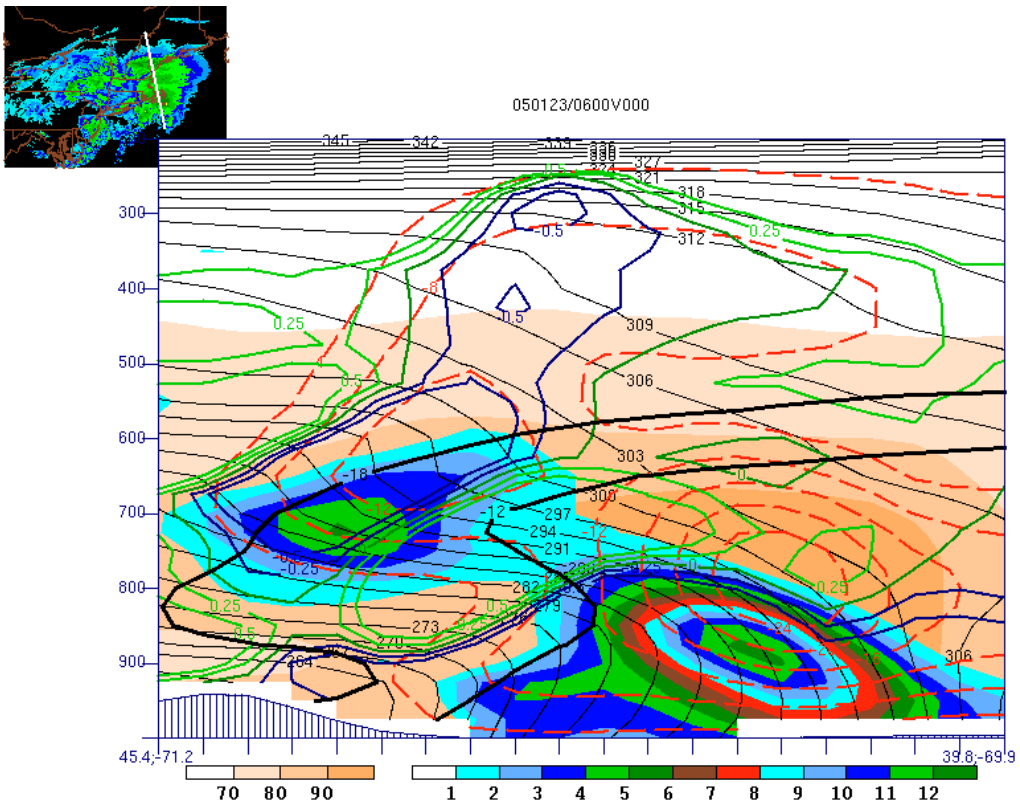

Fig. 3.20. (a–b) Same as Fig. 3.12 except at 0600 UTC 23 Jan 2005.

(a)

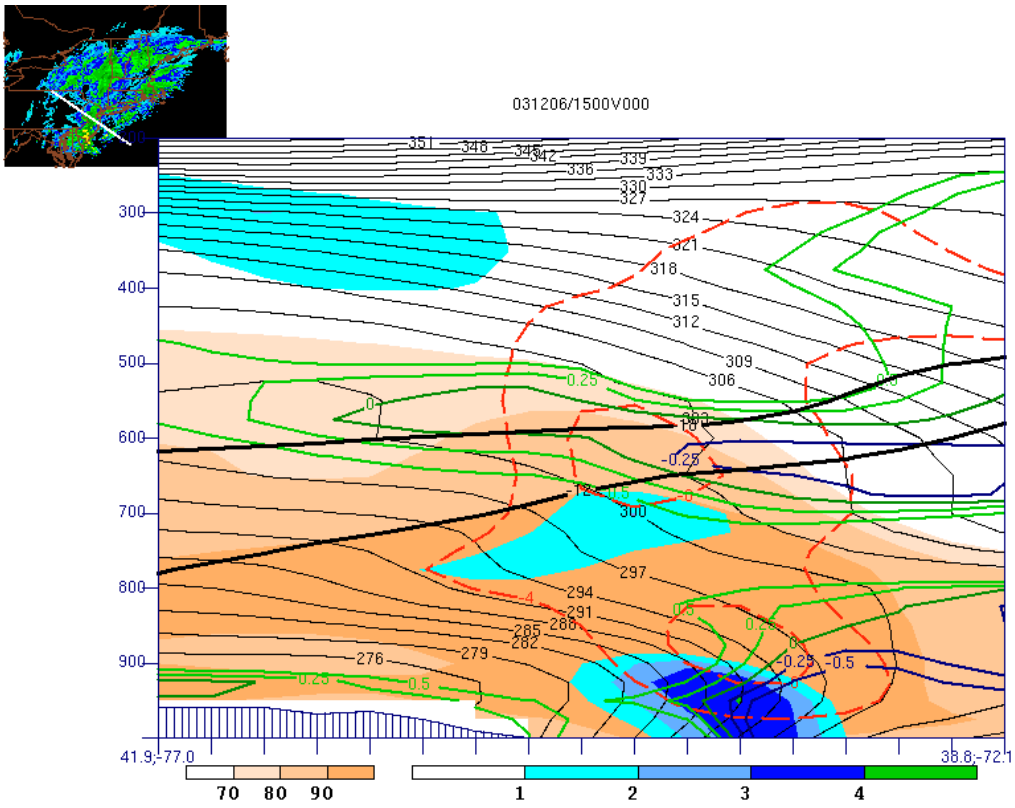

(b)

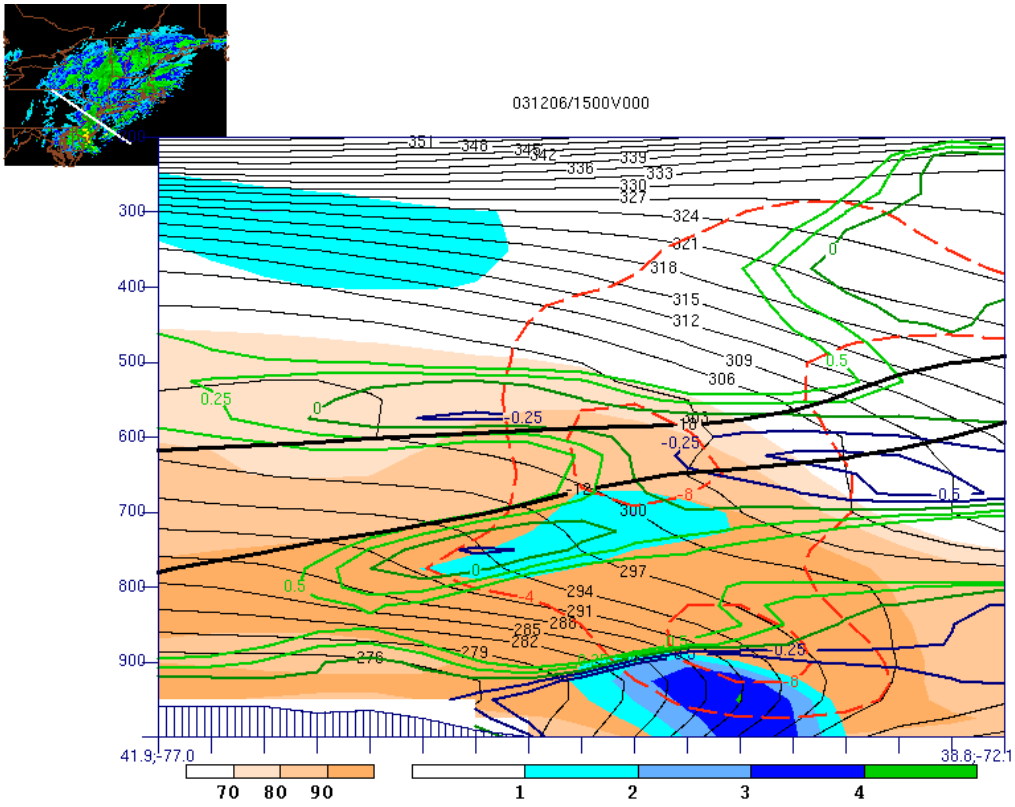

Fig. 3.21. (a–b) Same as Fig. 3.12 except at 1500 UTC 6 Dec 2003.

(a)

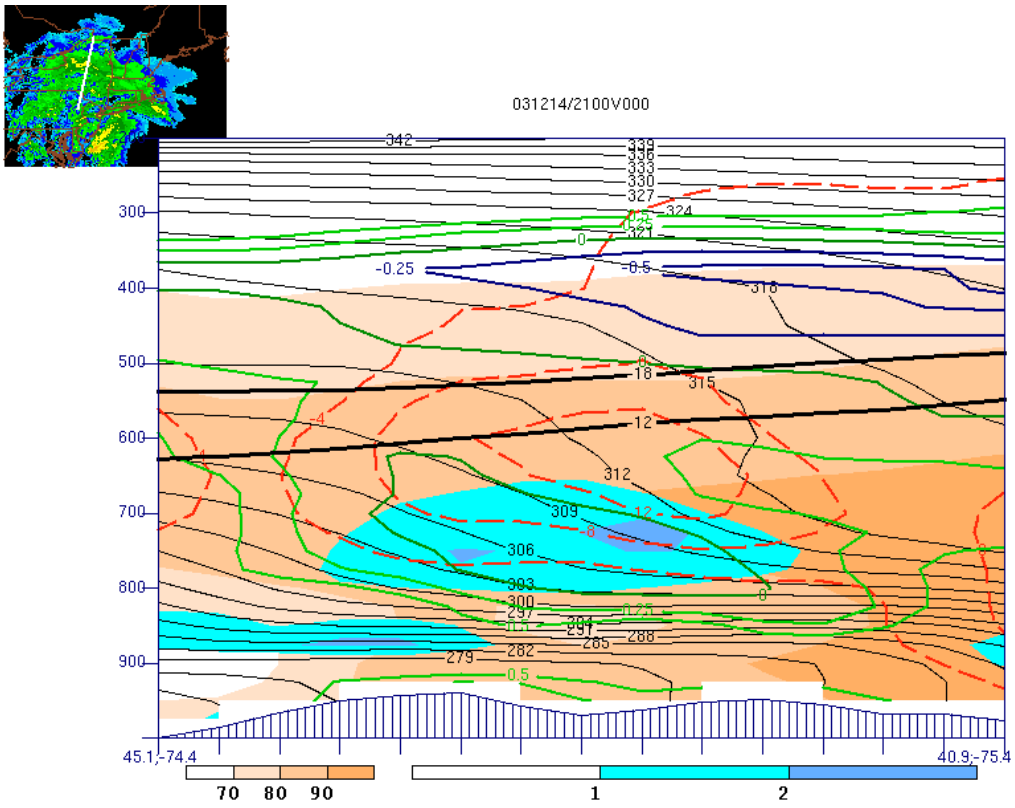

(b)

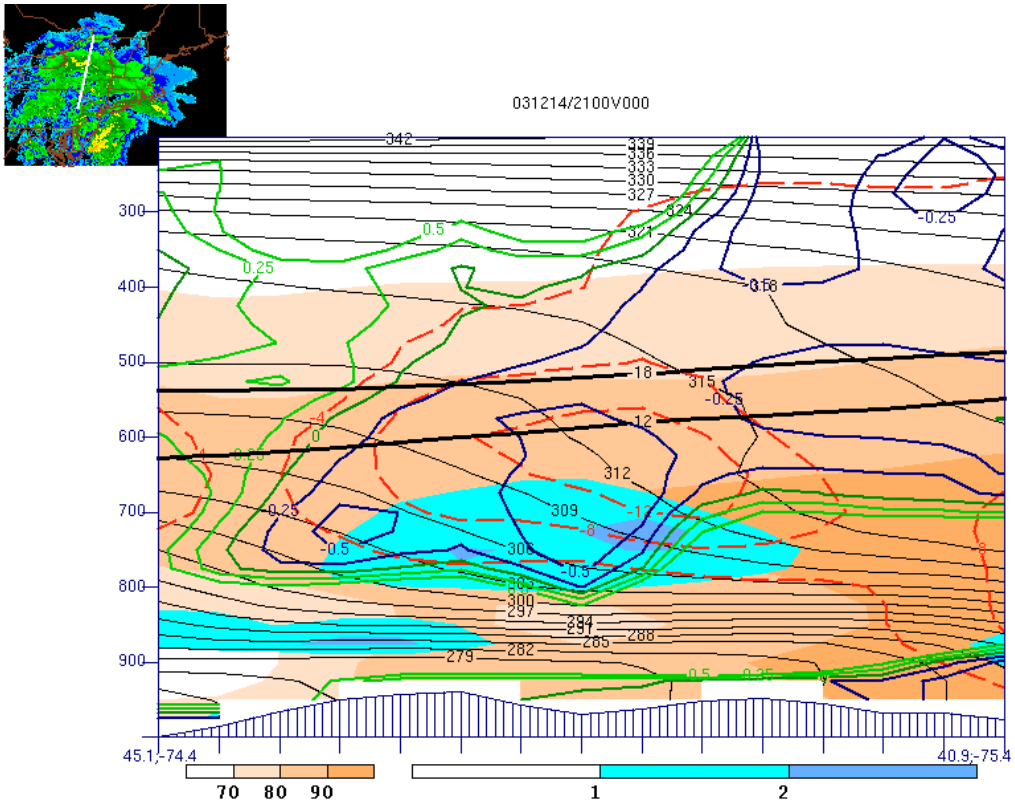

Fig. 3.22. (a–b) Same as Fig. 3.12 except at 2100 UTC 14 Dec 2003.

(a)

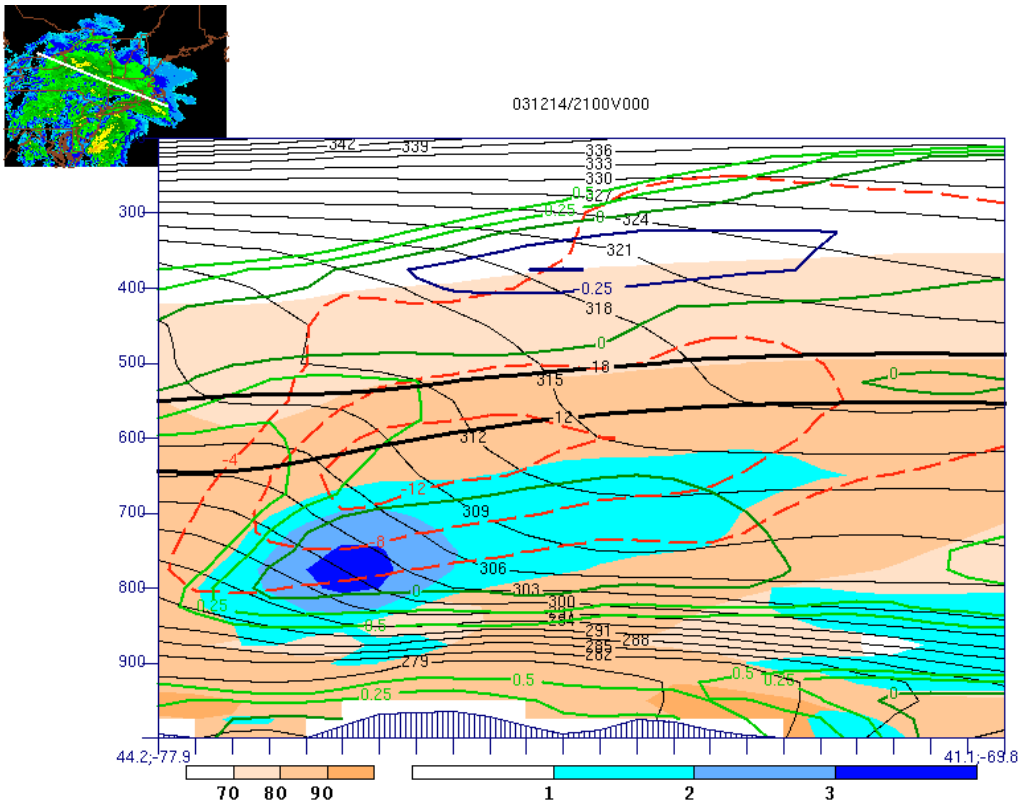

(b)

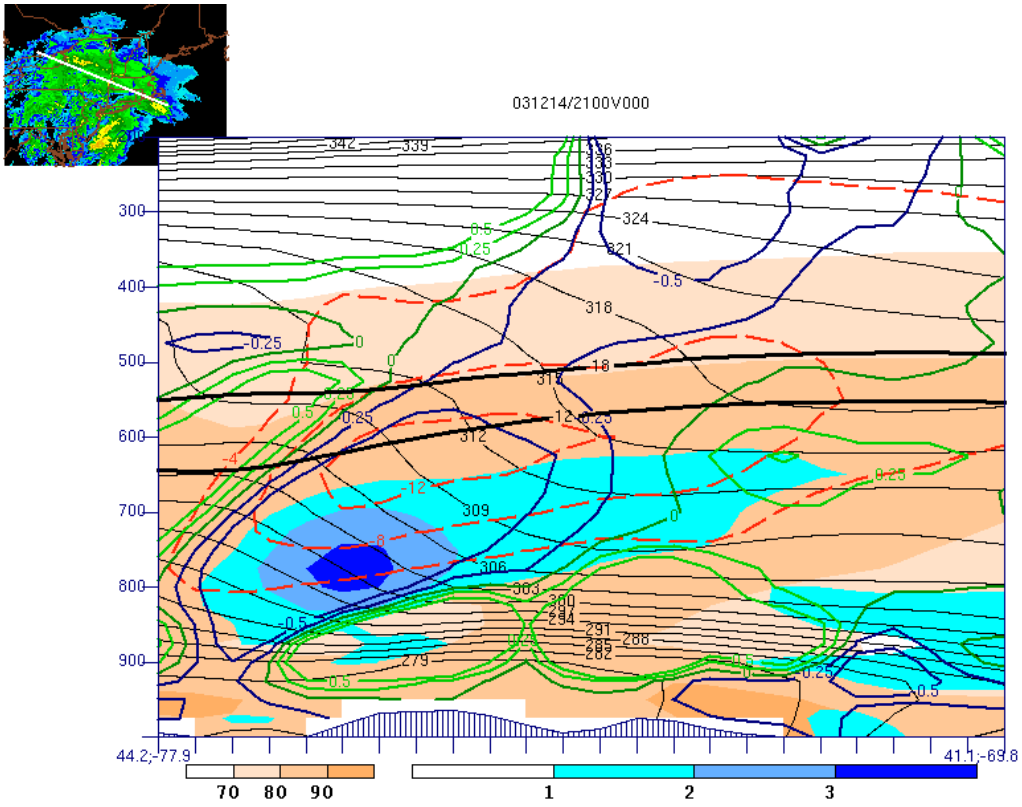

Fig. 3.23. (a–b) Same as Fig. 3.22 except with a different cross section slice.

(a)

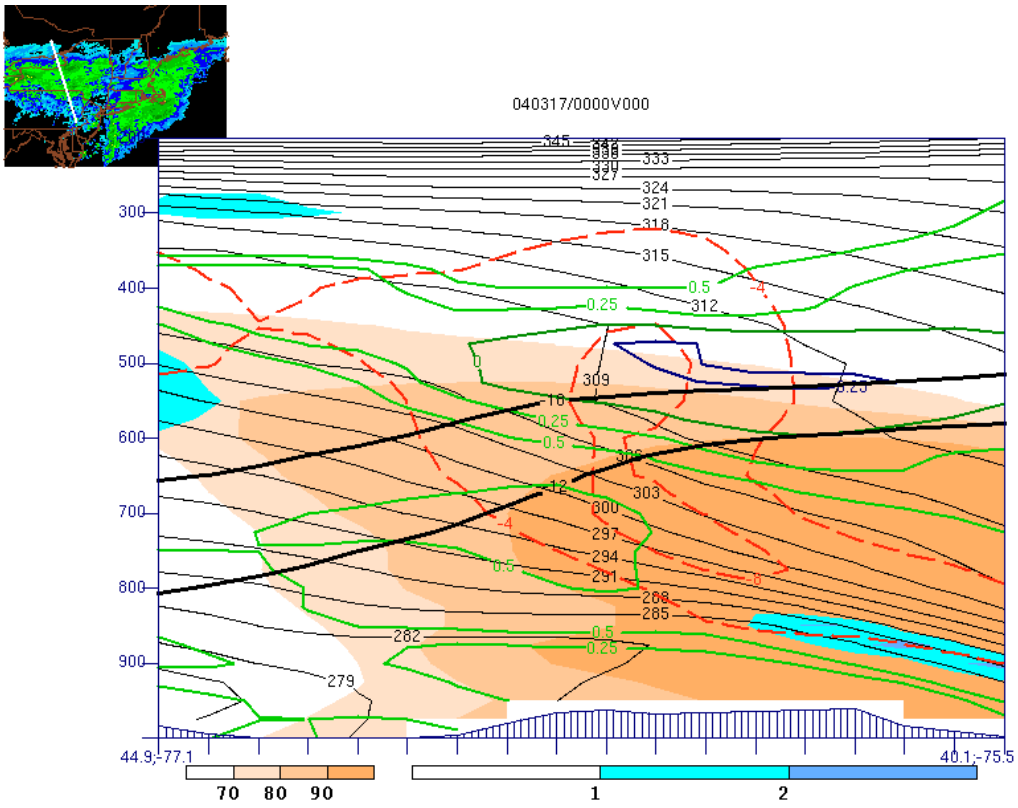

(b)

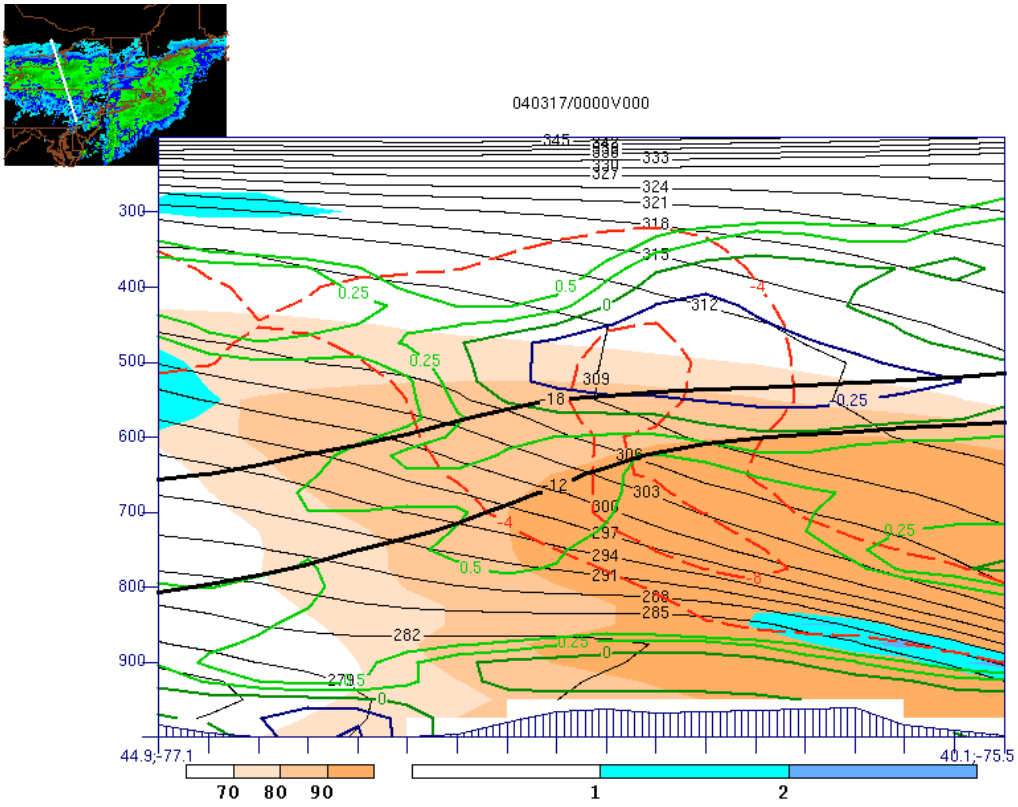

Fig. 3.24. (a–b) Same as Fig. 3.12 except at 0000 UTC 17 Mar 2004.

(a)

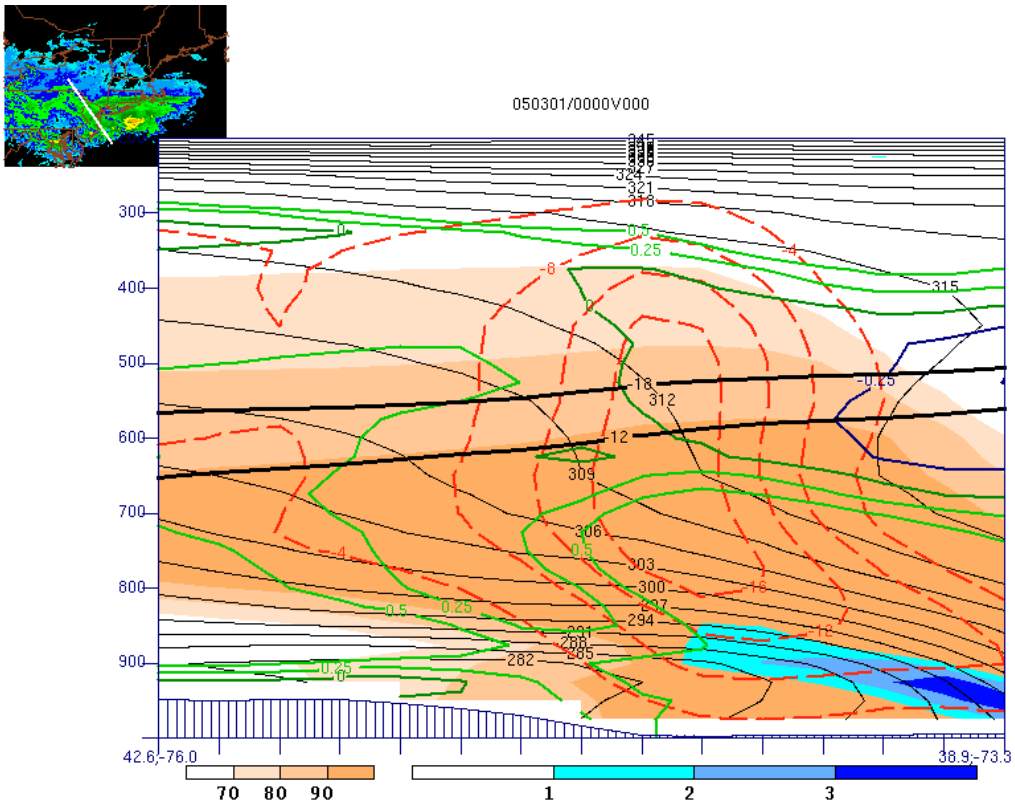

(b)

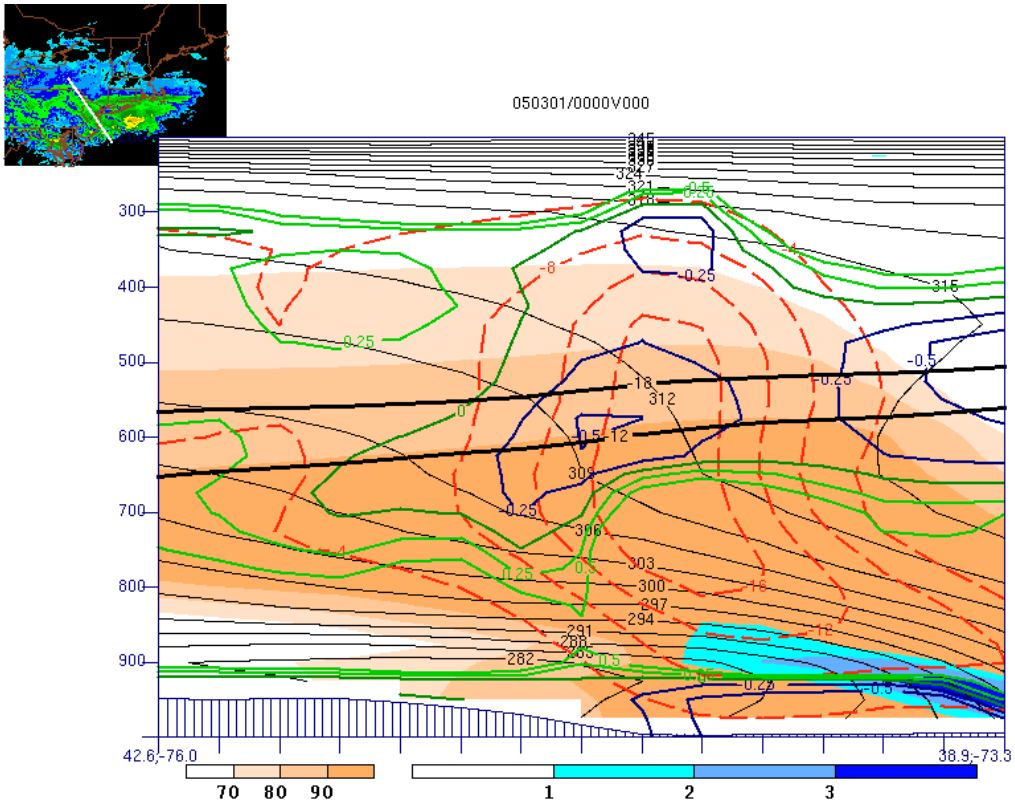

Fig. 3.25. (a–b) Same as Fig. 3.12 except at 0000 UTC 1 Mar 2005.

(a)

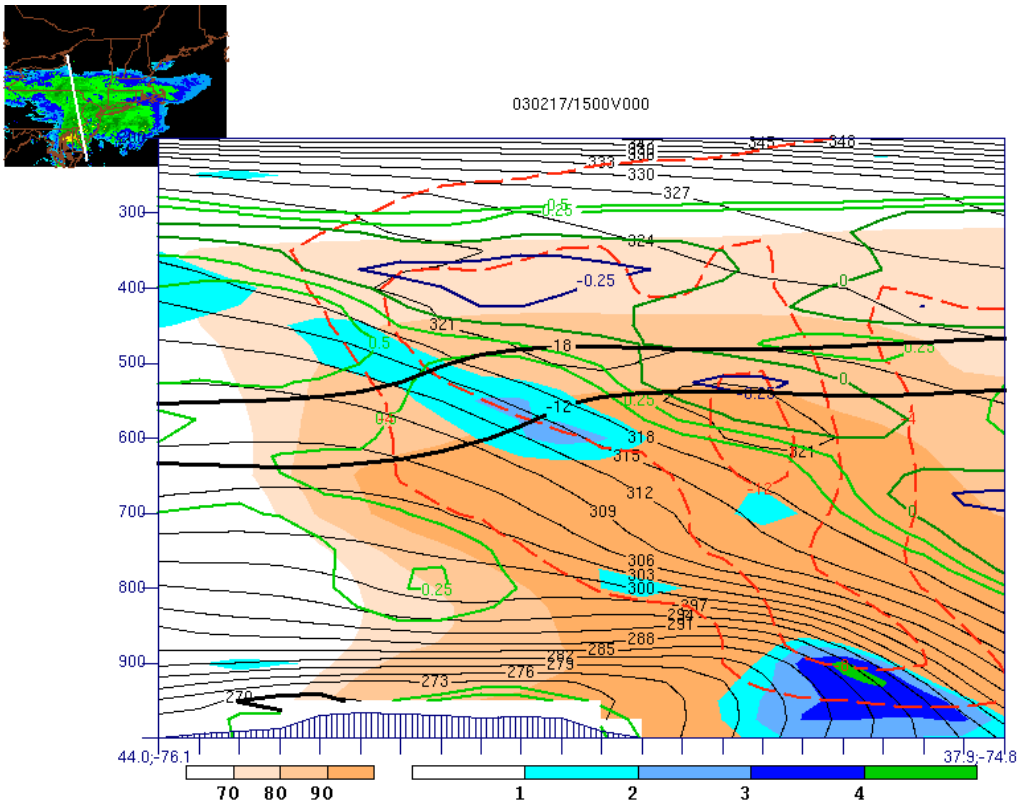

(b)

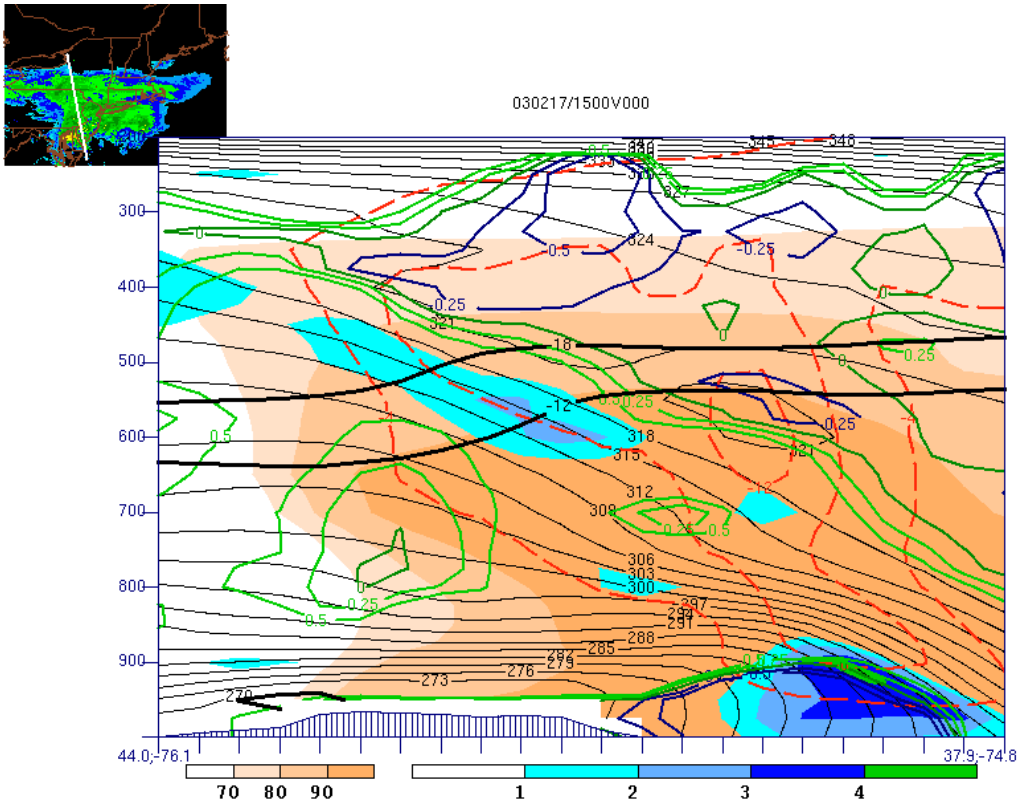

Fig. 3.26. (a–b) Same as Fig. 3.12 except at 1500 UTC 17 Feb 2003.

(a)

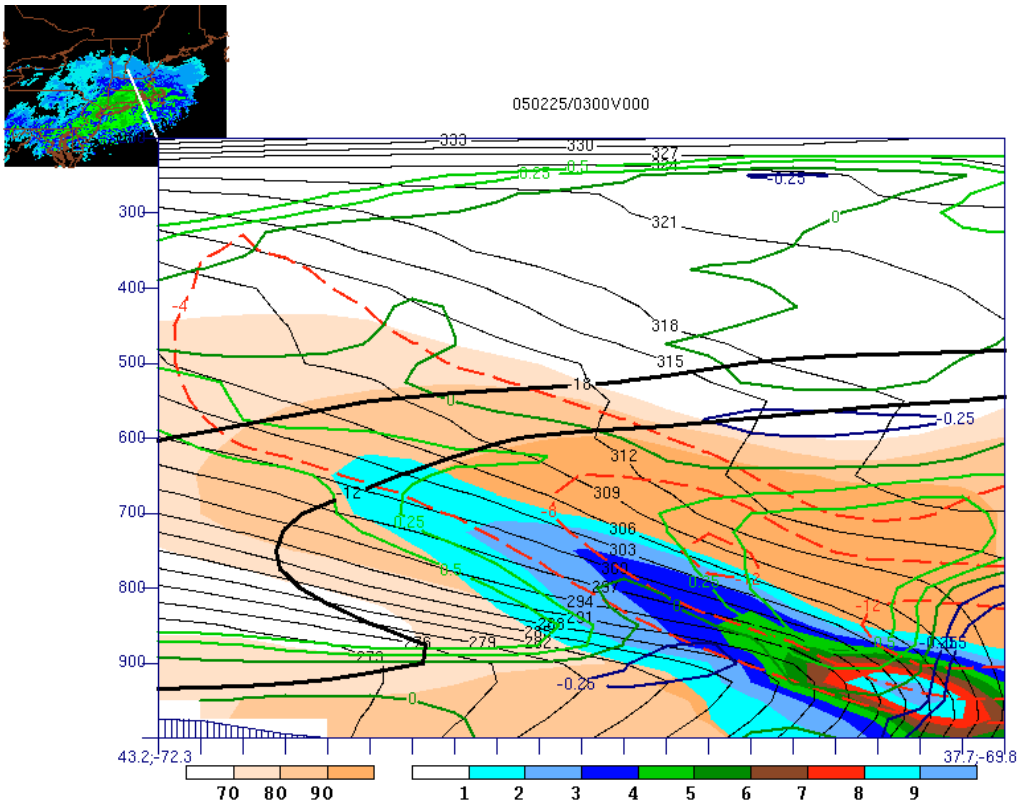

(b)

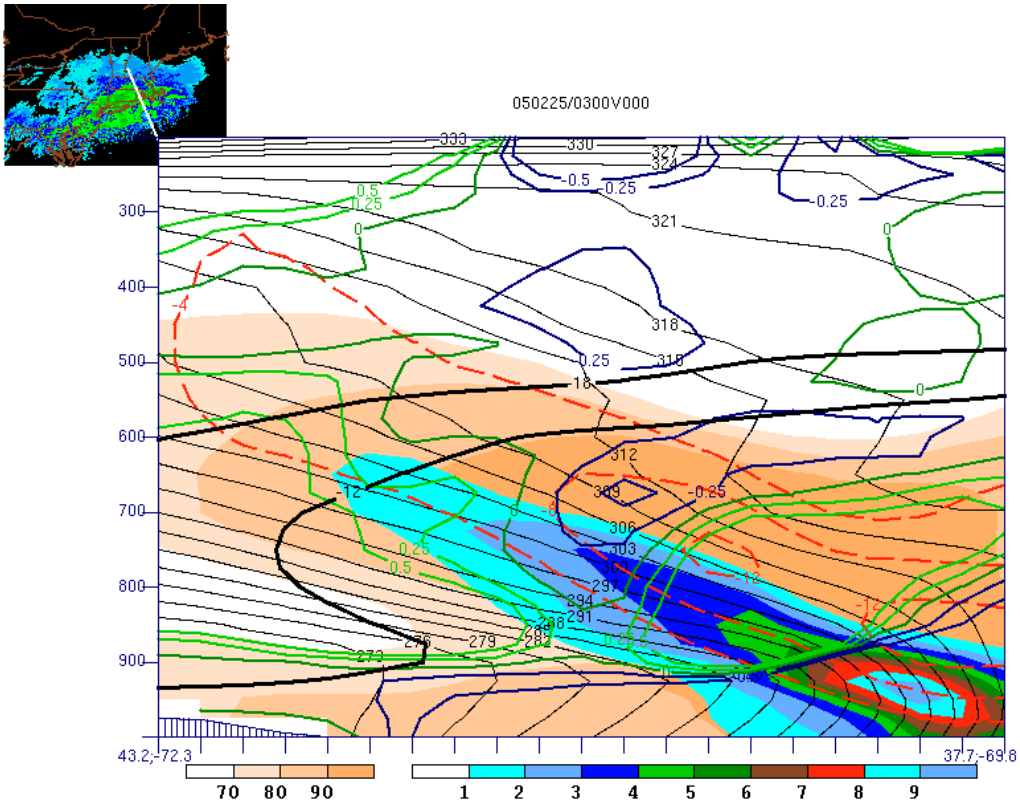

Fig. 3.27. (a–b) Same as Fig. 3.12 except at 0300 UTC 25 Feb 2005.

(a)

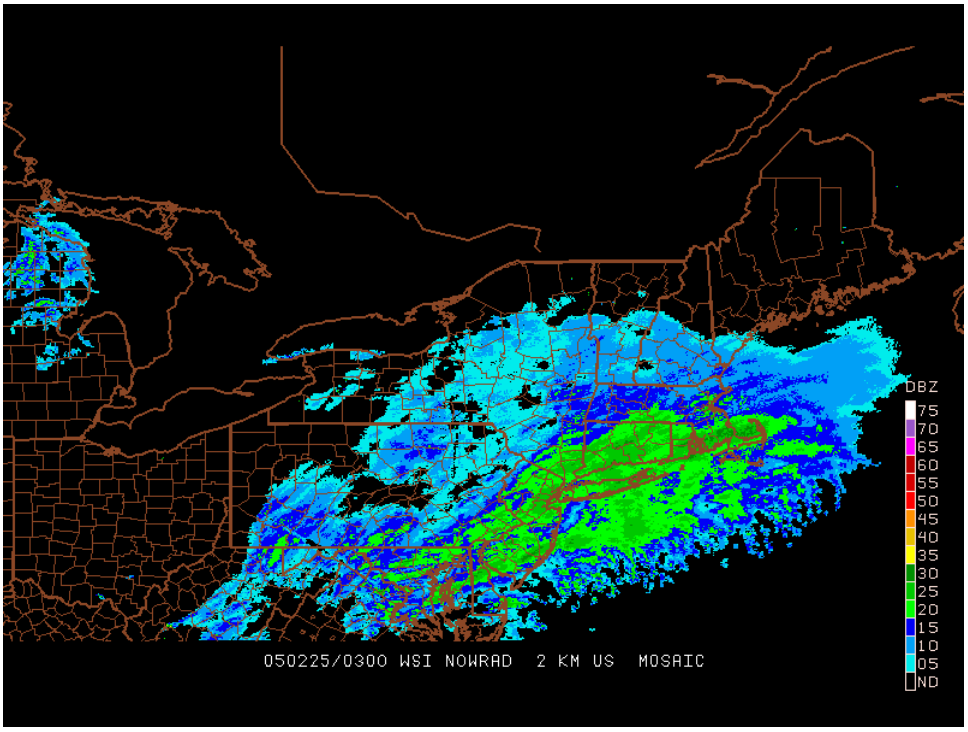

(b)

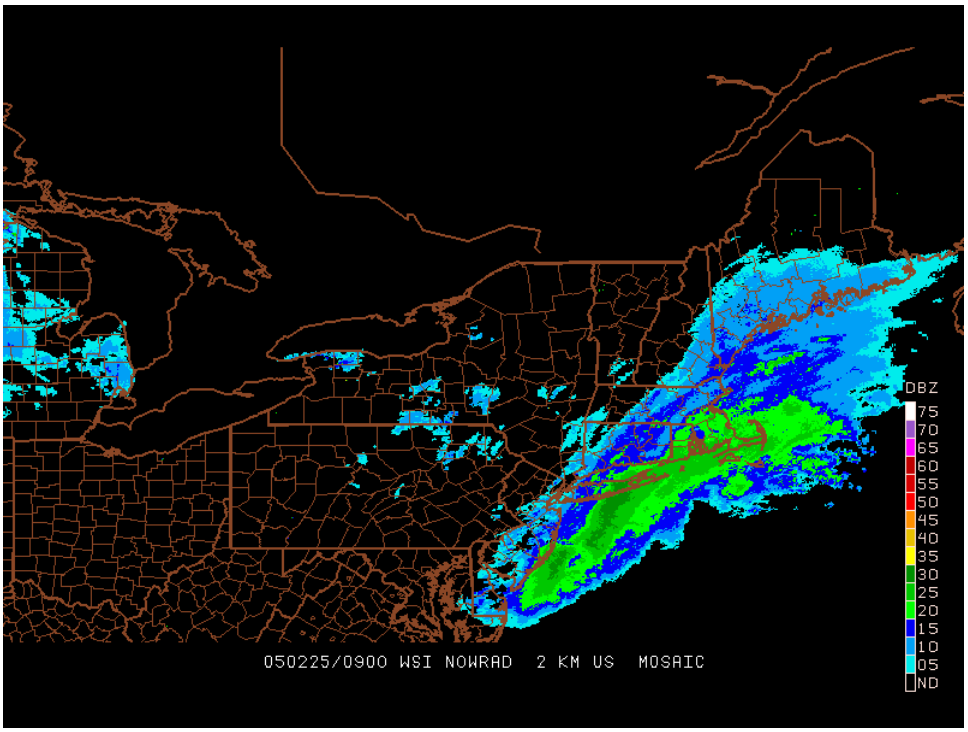

Fig. 3.28. Same as Fig. 3.1 except at (a) 0300 UTC and (b) 0900 UTC 25 Feb 2005

(a)

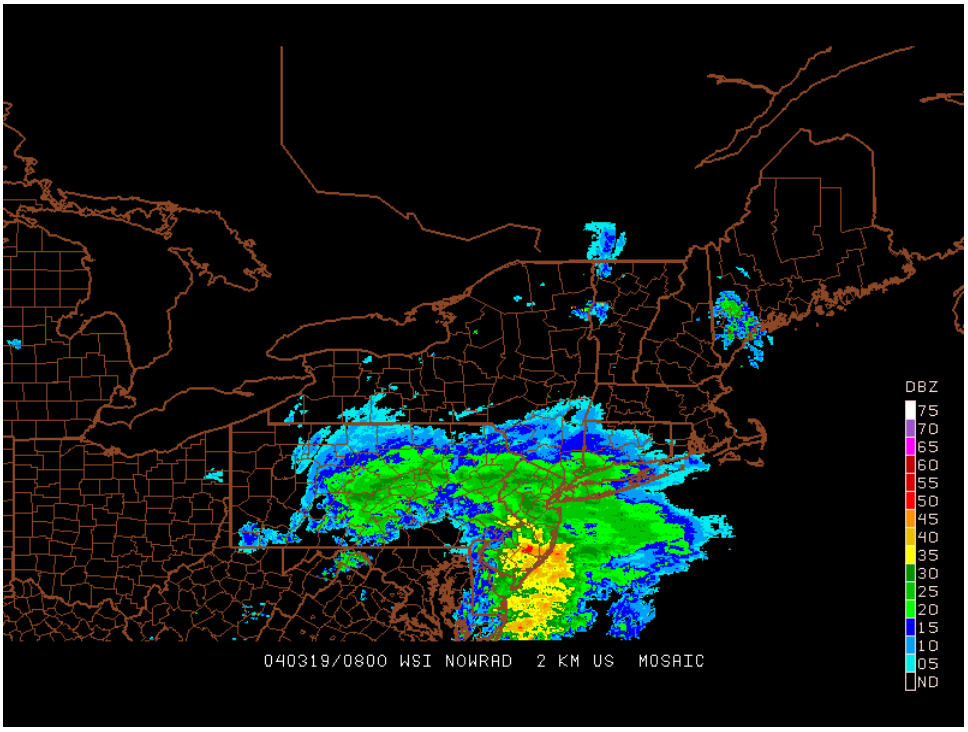

(b)

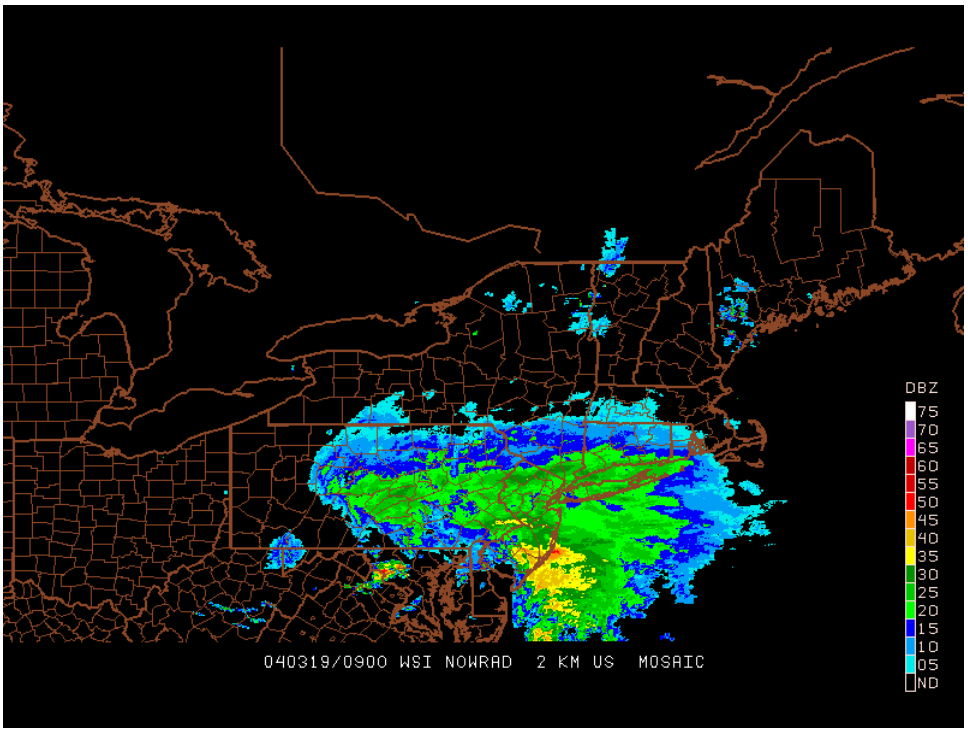

Fig. 3.29. Same as Fig. 3.1 except at (a) 0800 UTC and (b) 0900 UTC 19 Mar 2004.

(a)

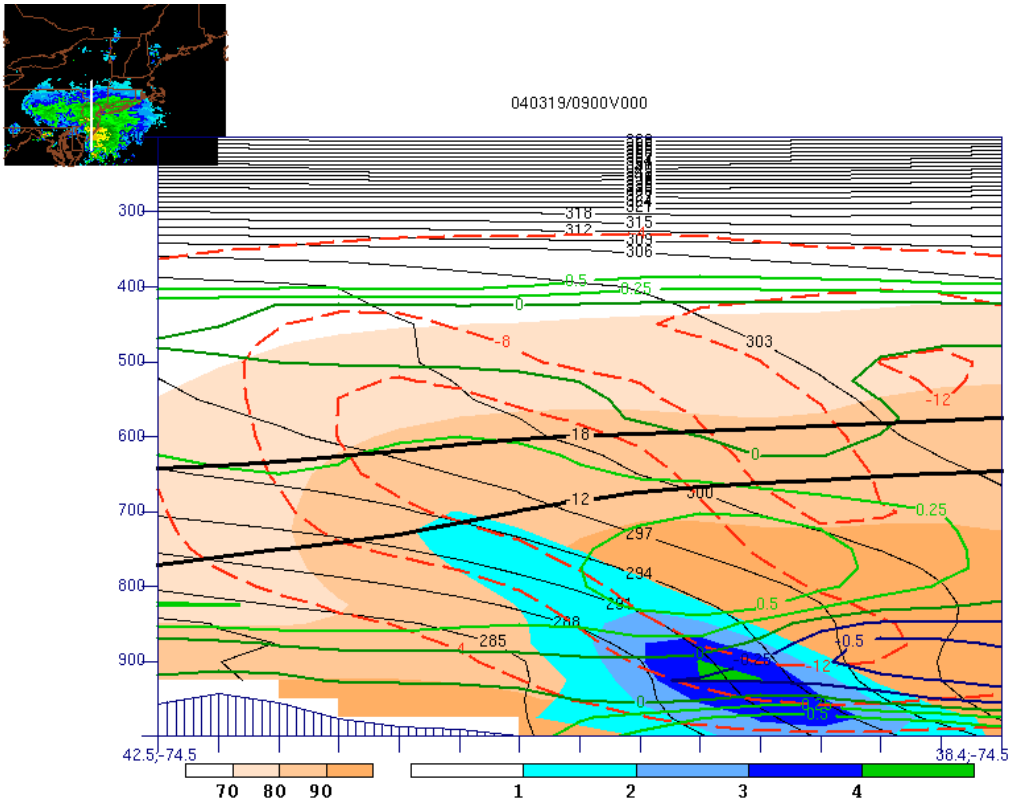

(b)

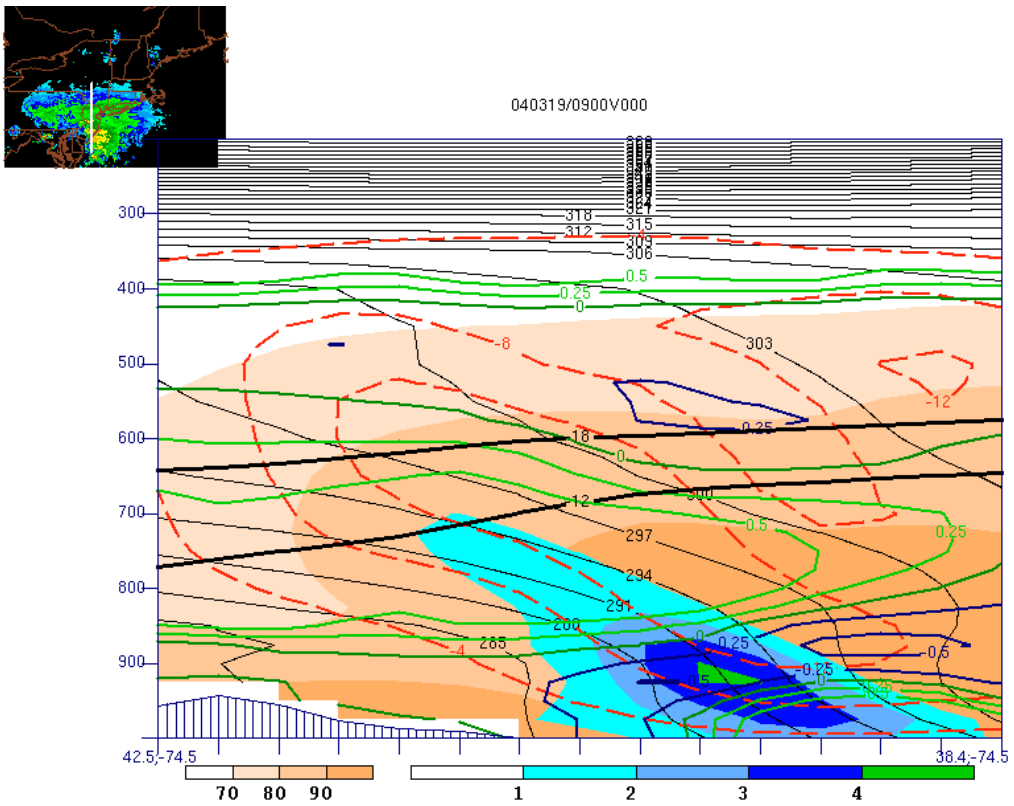

Fig. 3.30. (a–b) Same as Fig. 3.12 except at 0900 UTC 19 Mar 2004.

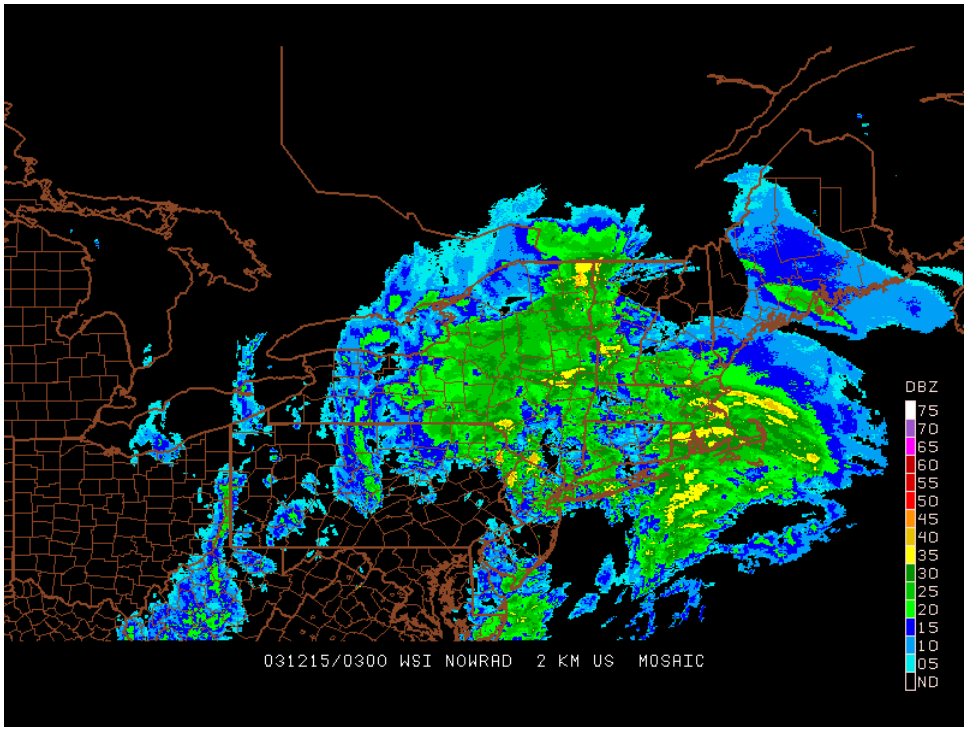

Fig. 3.31. Same as Fig. 3.1 except at 0300 UTC 15 Dec 2003.

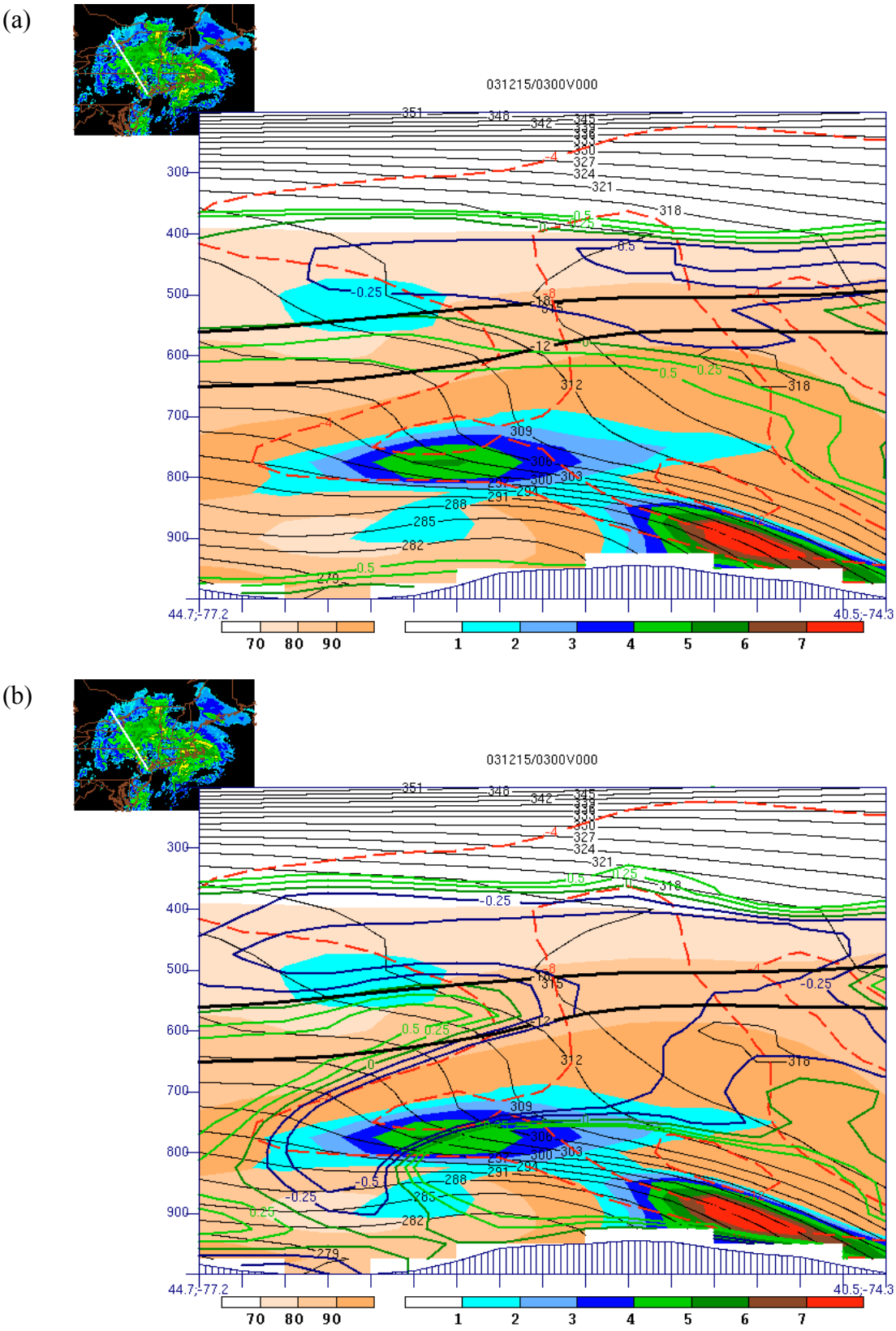

Fig. 3.32. (a–b) Same as Fig. 3.12 except at 0300 UTC 15 Dec 2003.

(a)

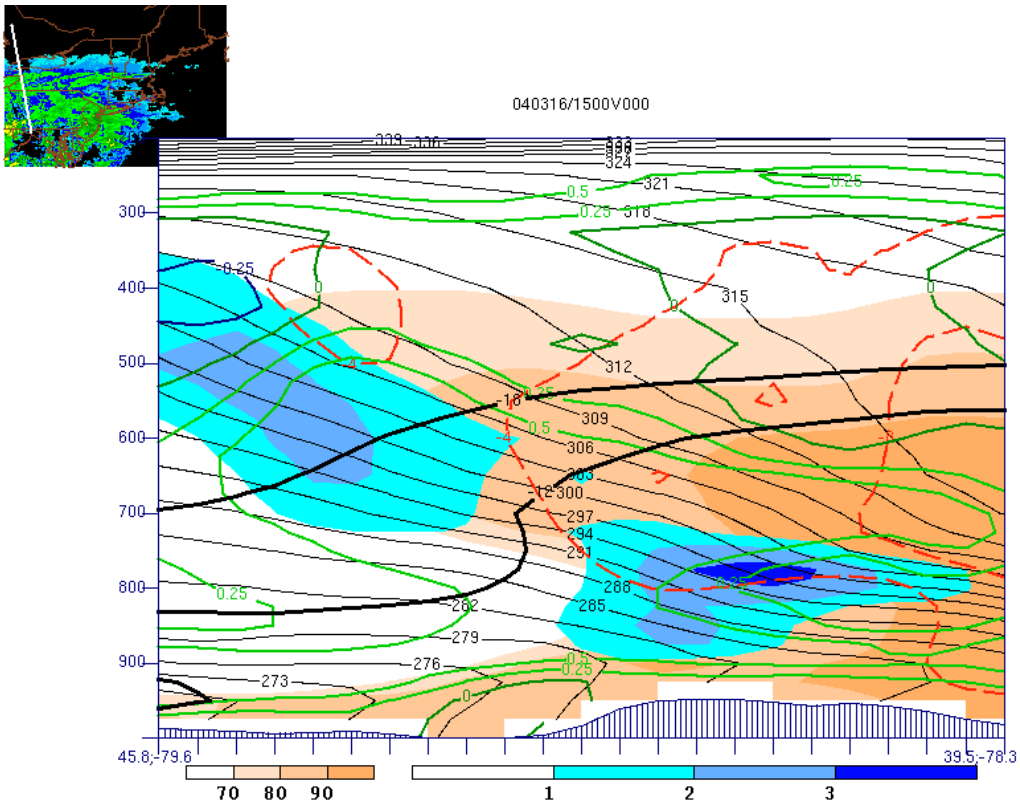

(b)

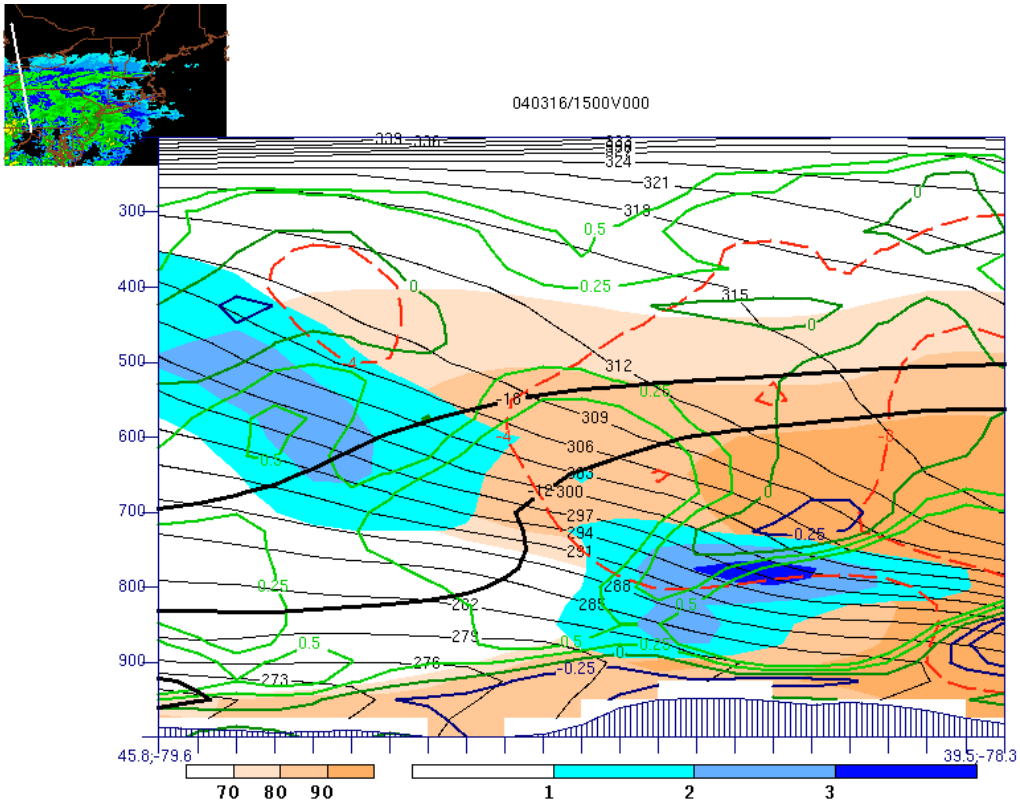

Fig. 3.33. (a–b) Same as Fig. 3.12 except at 1500 UTC 16 Mar 2004.

(a)

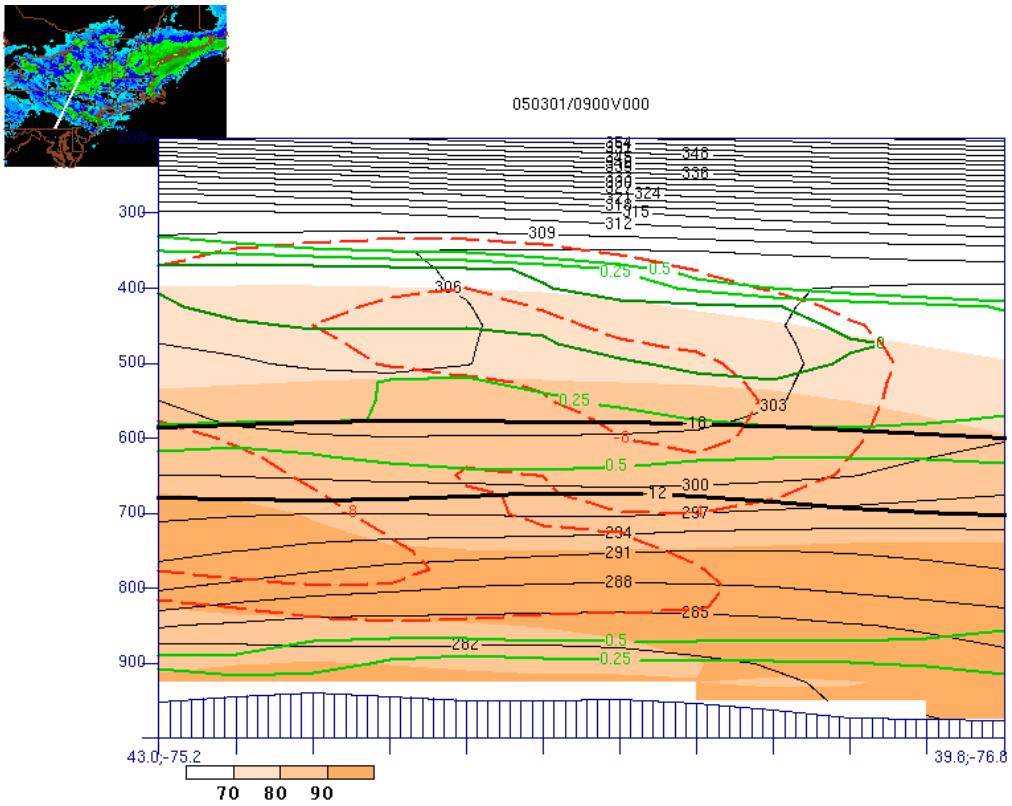

(b)

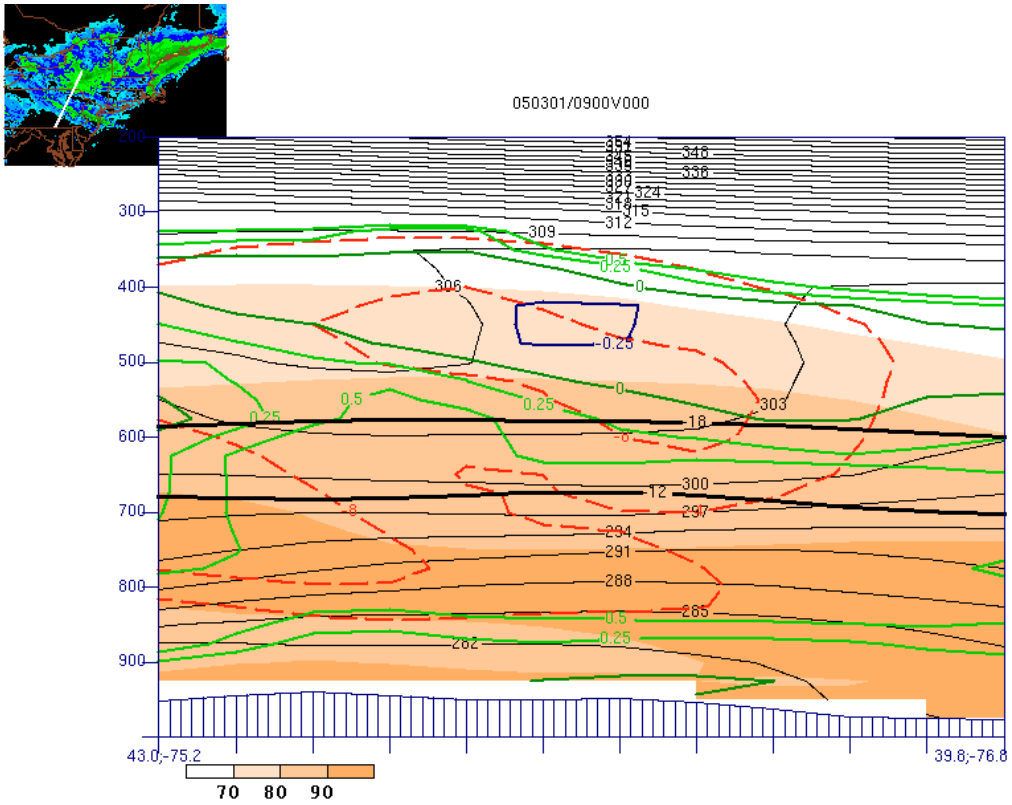

Fig. 3.34. (a–b) Same as Fig. 3.12 except at 0900 UTC 1 Mar 2005.

(a)

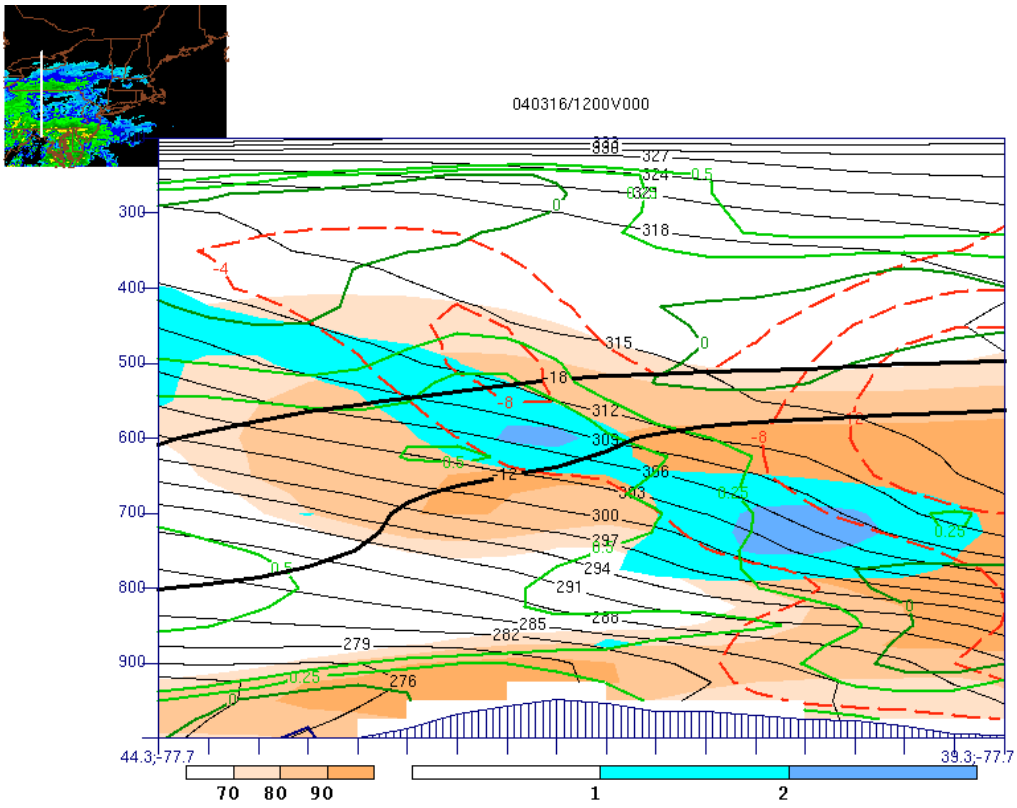

(b)

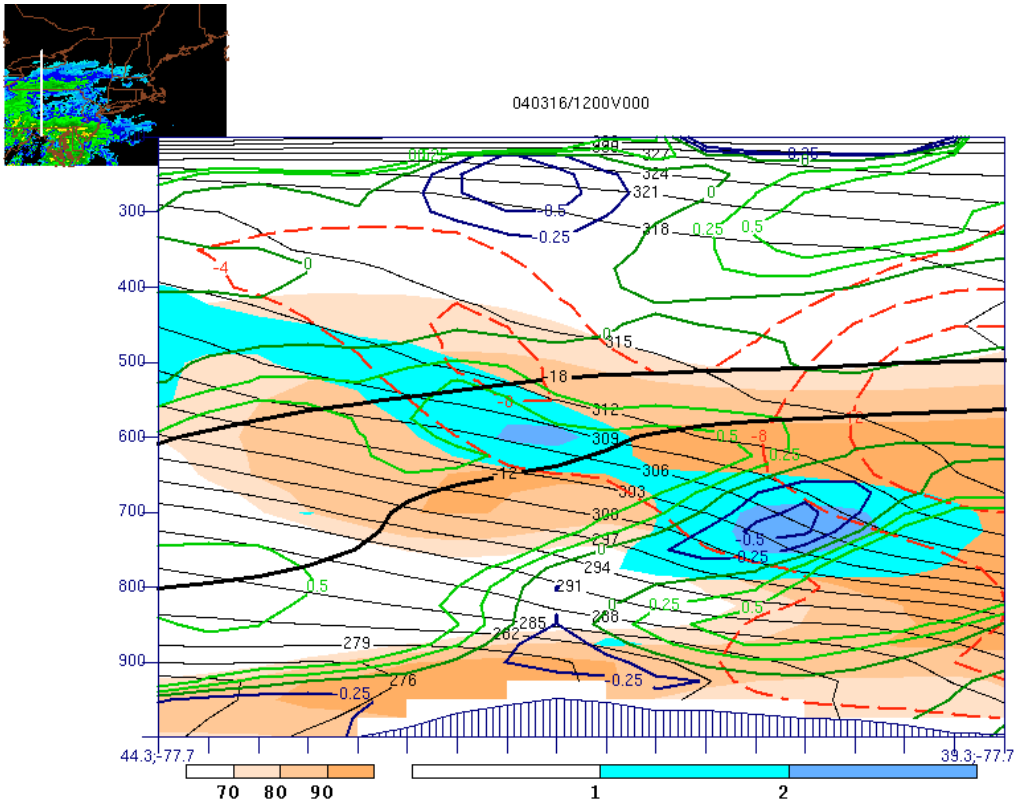

Fig. 3.35. (a–b) Same as Fig. 3.12 except at 1200 UTC 16 Mar 2004.

(a)

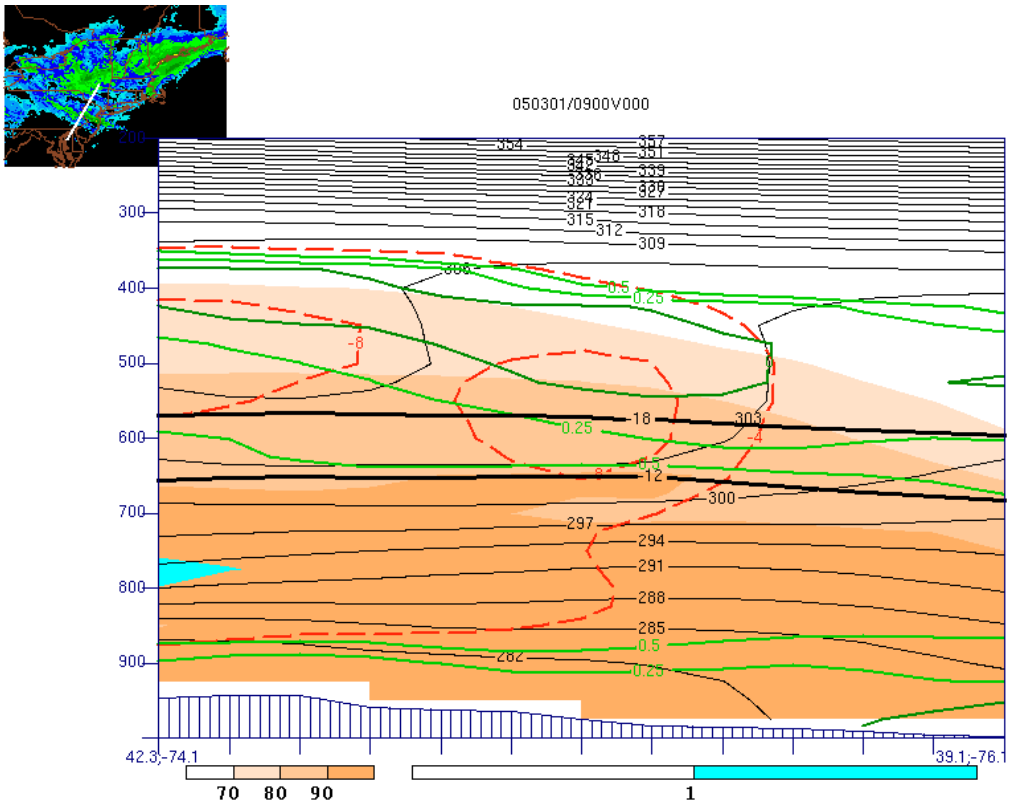

(b)

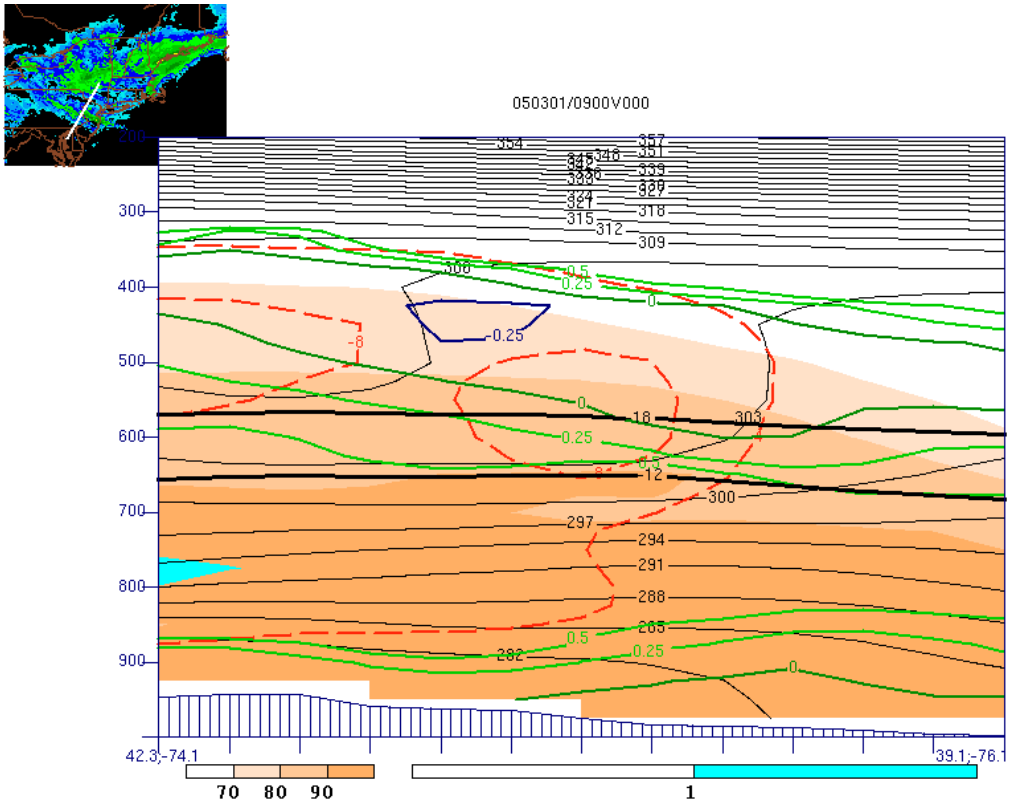

Fig. 3.36. (a–b) Same as Fig. 3.12 except at 0900 UTC 1 Mar 2005.

4. Discussion

4.1 The Modes

4.1.1 Classic Band

The strong frontogenesis characteristic of "classic band" cases produces a strong ageostrophic circulation (Fig. 1.3), while the steep slope of the frontogenesis axis ensures that a significant portion of the circulation is oriented vertically. No other mode has frontogenesis sloping as steeply as that of a "classic band," and a conceptual model in Novak et al. (2004; Fig. 1.6) confirms such a difference in frontogenesis slope between banded and nonbanded cases. Since the frontogenesis in these "classic band" cases is surface-based, strong ascent rooted in the boundary layer delivers ample moisture into the precipitation region. Additionally, the strongest frontogenesis values near the surface are consistent with the strongest temperature gradient being located there, as well as with a frontal zone that weakens with height.

The WMSS and CSI (by the EPV_g^* definition) found on the warm side of the frontal zone focuses the updraft. This situation is consistent with Emanuel's (1985) work that shows a strong, steep updraft ahead of a region of maximum frontogenetical forcing with WMSS on its warm side (Fig. 1.5). Furthermore, Nicosia and Grumm (1999) describe a feedback mechanism between increasing frontogenesis and EPV reduction (see section 1.2.4.3) that would help to sufficiently strengthen the circulation to produce a "classic band." However, the other modes also feature WMSS and CSI on the warm side of their frontal zones.

The EPV_g^* "bull's-eyes" co-located with the surface positions of bands are observed in other modes; yet, if the frontogenesis pattern is indicative of a "classic band,"

then the "bull's-eye" could prove useful in forecasting the location of a band once the environment has been diagnosed to be favorable for one. Even though the reason for the "bull's-eye" cannot be explained at this time, its location could be used to improve a band forecast.

Lastly, the maximum ascent intersects the dendritic growth zone (DGZ) for these cases, which is a favorable situation for high precipitation efficiency and high snow-to-liquid ratio snowfalls. Waldstreicher (2001) discusses a crosshair approach for forecasting snow-to-liquid ratios, where the highest ratios are possible when the DGZ and the maximum vertical velocities intersect. However, while the intersection of these two features is important for heavy snow, the five modes discussed in this study all exhibit this feature, as they are all forms of heavy snow by their very nature. Thus, while this intersection favors heavy snow, it is not a mode-distinguishing feature.

4.1.2 Uniform

It appears that the band-like "uniform" cases are evidence of a time lag between the appearance of a band-like cross section and actual band formation. However, a larger sample size of such cases and null cases is needed to make this statement with more confidence and to understand why such a lag exists. Regardless, the increase in strength and steepness of the frontogenesis as the precipitation region tightens from a "uniform" shield to a "classic band" agrees with theory: the frontogenesis is expected to increase in the presence of reduced symmetric stability and steepen because of the vertical speed shear inherent in these baroclinic regions. Additionally, it appears that the stability does not decrease over time, as would be expected by the frontogenesis–EPV feedback

mechanism (section 1.2.4.3). Instead, the stability remains unchanged (Figs. 3.16 and 3.12) or even increases (Figs. 3.17 and 3.18). Perhaps the instability present prior to band formation is partially consumed as the frontogenesis increases and the precipitation region tightens into a band (D. Nicosia 2006, personal communication).

As for the typical "uniform" cases, weak frontogenesis and flat slopes prevent a band from forming. Weak values indicate an inadequate frontogenetical circulation, while the flat slope restricts vertical motion by precluding much of the frontogenetical circulation from being situated vertically. The latter is important when the frontogenesis is strong but flat, e.g., Fig. 3.14. Here, a strong frontogenetical circulation develops but its orientation is primarily in the horizontal direction, which does not promote significant precipitation production. The large variation in vertical velocity strength for this mode, highlighted by a case with the strongest ascent in this study (Fig. 3.13), demonstrates how strong values of ascent in the absence of strong frontogenesis cannot produce a band. Furthermore, the ascent generated from strong isentropic lift does not appear to be tilted in the plane of the cross section. Rather, this type of lift is hypothesized to be tilted *into* the plane of the cross section, e.g., Case 15 at 2100 UTC 22 Jan 2005 (Fig. 4.1, cf. Fig. 3.13). With the cross section slice no longer perpendicular to the thickness contours, the cross section may better capture the curving warm conveyor belt and its associated upglide ascent.

Besides varying vertical velocity, the "uniform" cases also exhibit varied values and depths of reduced stability. In addition, the CSI observed with both EPV* formulations appears to play no role. As will be discussed in section 4.2, it appears that

the frontogenesis—not the WMSS and CSI—plays the role of mode-distinguisher. However, no CI is present in "uniform" cases, which distinguishes this mode from others.

4.1.3 Transient Band

The primary feature of the "transient band" cross section is an area of frontogenesis decoupled from the surface, i.e., not surface-based. Consequently, the ascent is not strongly rooted in the boundary layer, inhibiting a continous supply of rich boundary layer moisture from entering the precipitation region that is needed to sustain the heavy snow in the bands. This action is especially important for the "evolving band" form of the mode. On the other hand, the "messy band" example (Figs. 3.5 and 3.22) argues against this idea, as it has decoupled frontogenesis but continuous, very heavy snowfall with numerous 35-dB*Z* echoes.

CI appears to play a role, especially in the "broken band" and "messy band" forms. CI leads to mesoscale updrafts and downdrafts, which distort the precipitation pattern through localized enhancements and reductions in reflectivity. "Bull's-eyes" similar to those in the "classic bands" are once again observed; and the "broken band" stacked "bull's eyes," besides indicating the band position, add extra distortion to the precipitation pattern. Although lacking an explanation at this time, the question can be asked as to what role the deep region of CSI plays in the "messy band" case (Fig. 3.22). Furthermore, as mentioned in section 3.4.1.3, an along-band cross section for this case (Fig. 3.23) reveals that the "messy band" is not two-dimensional. However, for a "classic band," an along-band cross section, e.g., Case 5 at 2100 UTC 7 Feb 2003 (Fig. 4.2), reveals comparatively much less variation in stability and frontogenesis along the band.

4.1.4 Bandlets

Three features immediately distinguish a "bandlets" cross section from one of another mode. First, the frontogenesis is almost always surface-based, differentiating the mode from a "transient band." Second, the frontogenesis strength is weak-to-moderate, differentiating the mode from a "classic band." Third, although reduced EPV* fields vary considerably in value, depth, width, and shape, the existence of CI sets the "bandlets" apart from the "classic band" and "uniform" modes.

The CI is key, as it once again causes mesoscale updrafts and downdrafts, manifested by the localized enhancements and reductions in radar reflectivity within a precipitation shield. This pattern may be similar to the seemingly random popcorn, or "airmass," thunderstorms when no organized forcing is present. In addition, cases with deeper regions of CI have messier "bandlets" patterns, possibly due to more upright mesoscale circulations.

The existence of CI leads to a very distinctive ascent pattern known as the "escalator–elevator" (section 3.4.1.4). This pattern of forced frontogenetical ascent ("the escalator") and free upright convection ("the elevator") is observed in four of the nine nonband-like cross sections, e.g., Figs. 3.24 and 3.25. The resolution of the NARR may be responsible for the pattern not being more prevalent. Martin (1998) states that the model resolution precludes him from making a definite statement about the role of CSI release in a band case study because the 40-km resolution of his in-house model is not high enough to resolve instability effects. The same may be true with the similar-resolution, 32-km NARR.

Neiman et al. (1993) observe this phenomenon in range–height indicator (RHI) Doppler radar reflectivity and front-normal wind velocity diagrams (their Fig. 7) taken from NOAA WP-3D research aircraft during the Experiment on Rapidly Intensifying Cyclones over the Atlantic (ERICA) field program (Neiman and Shapiro 1993). In those diagrams, the authors observe slantwise frontal upglide (the "escalator") and mesoconvective updrafts (the "elevator"). Then they summarize their findings with an "escalator–elevator" schematic (Fig. 4.3) proposed by Shapiro et al. (1991), which displays the combination of the two features.

In addition, the Nicosia and Grumm (1999) case from 15 Nov 1995 contains "bandlets" (their Fig. 8) southeast of the focus area of the study. A close look at a cross section through the precipitation region (their Fig. 10b) reveals an area of CI in the southeastern portion of the cross section coincident with the "bandlets." A cross section featuring vertical velocities is not available, so it cannot be said for sure that the frontogenesis below the region of CI acts as the "escalator," transporting air parcels to the "elevator" of the CI region.

The "classic band"-like "bandlets" cross sections are best explained using the same reasoning used for the "classic band"-like "uniform" cross sections. The "broken band"-like cases may a hybrid of pure "broken bands" and pure "bandlets." This situation exposes a problem associated with a subjective classification like the one in this study: which category should these cases be in or should they be unclassifiable? Lastly, these band-like "bandlets" cross sections do still feature CI, which is the key feature of the "bandlets" mode.

4.1.5 Fractured

"Fractured" cross sections are the toughest to decipher. The fragmented frontogenesis evident in these cross sections may indicate that the localized areas of frontogenesis correspond to the enhancements in precipitation and that the breaks between the frontogenesis fragments correspond to the lower dB*Z* spaces in the radar imagery. In addition, the decoupled nature of the frontogenesis may point to the moisture issues discussed earlier, as would the fact that the areas of maximum ascent coincide with regions of 70–80% RH, as opposed to 80–90+% RH for the other modes. This difference may be due to the fact that the ascent maxima are more-elevated in the cross sections for this mode compared to the others. The decreased stability observed in the vicinity of the frontogenesis fragments may be due to the frontogenesis–EPV synergy previously discussed (Nicosia and Grumm 1999). Lastly, it appears that CI may play a role in some of the precipitation enhancements through more-intense mesoscale updrafts. The question arises whether the "fractured" mode is really just "transient bands" (because of the decoupled frontogenesis) and/or a larger-scale form of "bandlets" (because of the CI) but with drier spaces.

4.1.6 Solo Light Snowbands

The discussion of these bands is continued here for pure academic interest even though they are not included in the five modes. It appears that these snowbands are located in more-elevated regions of isentropic lift, and that even though the RH is lower than for the other modes, the frontogenetical forcing in the middle and upper troposphere

is enough to produce precipitation locally, while no precipitation is found adjacent to the band, e.g., Fig. 3.35.

This type of snowband can also form in another way. A single pure CSI band can develop in the absence of frontogenesis (Bennetts and Hoskins 1979), although such a band would not last as long as one supported by frontogenesis (Xu 1992). Such is the case with the short-lived band in Fig. 3.36, where there is CSI (by both EPV* formulations) but no NARR-resolved frontogenesis. Radar imagery (not shown) confirms that this band lasted for just a few hours.

4.2 Distinguishing and Nondistinguishing Features

4.2.1 Distinguishing Features

The cross-section elements that differentiate between the five modes include aspects of frontogenesis, instability, ascent, and relative humidity. In regard to frontogenesis, both its strength and steepness separate "classic bands" from the other modes, as strong, steep frontogenesis favors a stronger, more vertically oriented frontogenetical circulation favorable for bands. Surface-based frontogenesis and associated ascent strongly rooted in the boundary layer distinguish "classic band," "bandlets," and "uniform" modes from "transient band" and "fractured" modes, as these characteristics allow for a continual supply of rich boundary-layer moisture into the precipitation region. Fragmented frontogenesis sets apart "fractured" cases from the others, as it promotes broken areas of precipitation.

In regard to instability, CI differentiates "transient band," "bandlets," and "fractured" modes from the other two, as CI distorts precipitation patterns through

mesoscale circulations with enhanced updrafts and compensating downdrafts. Although CI may exist in "classic band" cross sections, the ascent patterns reveal that the frontogenetical circulations dominate CI-induced circulations. The "escalator–elevator" ascent pattern distinguishes the "bandlets" mode by creating enhancements in radar reflectivity within a precipitation shield. Another distinguishing instability feature is the stacked EPV_g^* "bull's-eyes" that further alter the precipitation pattern in the "broken band" form of "transient bands."

In regard to ascent, the tilt of the vertical velocity contours separates "uniform" cases from the rest, as these cases do not feature noticeably tilted ascent in the plane of the cross section. Lastly, in regard to relative humidity, lower RH in areas of maximum ascent separates "fractured" cases from the other four, as it aids the broken nature of the precipitation by allowing for dry pockets.

4.2.2 Nondistinguishing Features

There are many cross-section features that do not differentiate between the five modes, and several of them are discussed in this section. The ascent magnitude varies significantly within each mode, e.g., "uniform" cases feature ascent from −4 μb s^{-1} to as strong as −24 μb s^{-1}, while no "classic band" cases have ascent < −20 μb s^{-1}. However, it is the author's experience that the 12-km North American Mesoscale (NAM) model produces much stronger ascent values ≤ −40 μb s^{-1} in a very narrow region near bands, along with greater magnitudes of frontogenesis. Similarly, the "escalator–elevator" pattern of ascent and the roles of CSI and CI might be better represented in the higher-

resolution NAM. Thus, different features may act as better mode-distinguishers when higher-resolution models are analyzed.

Neither the intersection of maximum ascent with the DGZ (section 4.1.1) nor the depth of the DGZ (~50–100 hPa in most cases) differentiates the modes. Additionally, neither the intersection of maximum ascent with an EPV* or EPV_g^* "bull's-eye" nor with a region of CI helps to distinguish the modes. Relative humidity patterns offer no assistance, as well. While a tongue of dry air is observed below the frontal zone of the "classic band" cases, this feature is also seen in "bandlets" and "uniform" cases. Also, as mentioned in section 3.3, the large-scale forcing and vertical speed shear do not appear to help differentiate between the modes. A noted exception is that all "fractured" cases have weak 700-hPa closed or almost closed lows, possibly indicative of the breakdown of features that occur underneath such lows.

Probably the most significant nondistinguishing feature is reduced EPV*. All cases contain WMSS and CSI (at least in the EPV_g^* formulation), so it appears that reduced stability is an omnipresent feature of heavy snow events but that it is not a mode-distinguisher. It is nearly impossible to ascertain the role of CSI in this study, as it is hard to observe CSI circulations in the NARR cross sections; higher-resolution models may be necessary for these observations to be made. As stated in section 3.3, no correlation is found between the depths of selected reduced EPV* layers and the mode. In the cross sections, the value of EPV* also does not appear to matter. Likewise, patterns of EPV*, e.g., the shape of the EPV* < 0.25 PVU region, and the locations of reduced EPV* regions relative to frontal zones do not appear to affect the mode, as well.

Similarly, in his study on overrunning precipitation bands in the Southern Plains, Byrd (1989) finds that 60% of nonbanded cases meet the critical Richardson number (Ri < 1) for CSI. In addition, he finds no statistically significant difference in CAPE and SCAPE values between nonbanded, weakly banded, and strongly banded cases.

Evans (2006), in an analysis of a frontogenetically forced spring snowstorm, states that it is his experience that model forecasts of negative EPV* vary considerably from time step to time step and thus advises forecasters not to concentrate too much on exact values of EPV* but rather on the pattern of weakly positive and negative EPV* co-located with strong frontogenesis and saturation.

Schultz et al. (2000) state that assessing the forcing mechanism for ascent should be the primary concern and that the degree of instability merely modulates the response to the forcing. The authors feel that the emphasis on instability may detract forecasters from the real issue of the forcing mechanism. They also discuss a reason for caution when assessing stability in cross sections and soundings. A layer can be absolutely stable but a buoyant air parcel lifted up a moist adiabat from below may still be positively buoyant when lifted through that absolutely stable layer. Thus, *layer* stability can differ greatly from *parcel* stability. Accordingly, lifting from below could yield positive buoyancy in areas not considered to be unstable in this study from merely assessing the EPV* and $\partial \theta_e^* / \partial p > 0$ in cross sections.

4.3 EPV* vs. EPV_g^*

Throughout this thesis, mention has been made of both the full wind and geostrophic wind formulations of saturation equivalent potential vorticity (EPV*) and of

the quandary as to which is more appropriate to plot in cross sections. In this section, an attempt is made to decide how to approach this dilemma.

As seen in many pairs of cross sections in this thesis, EPV_g^* produces a messier stability pattern than does EPV*, e.g., cf. Figs. 3.12a–b, Figs. 3.19a–b, and Figs. 3.20a–b. In addition, EPV_g^* produces negative values in sub-70% RH areas much more often than does EPV*. In general, EPV_g^* is more negative than EPV* throughout the cross sections, indicating greater areas of CSI, although the significance of CSI is unknown at this time. Lastly, EPV_g^* minima "bull's-eyes" are observed to be co-located with surface positions of bands.

Since 1) the value of EPV* and EPV_g^* does not seem to matter, 2) WMSS is a necessary but not distinguishing factor, and 3) CI can be diagnosed with the θ_e^* contours, the full wind version of EPV* is recommended for use because it produces a cleaner cross section. Then, if the frontogenesis pattern indicates a "classic band," the geostrophic version can be used to find the location of the band along the sloping frontal zone. However, if the role of CSI in these cross sections can be established, then the geostrophic version might be better to use from the start because it produces more abundant regions of CSI and because the analysis procedure would then satisfy the thermal wind assumption from theory (Hoskins 1974; Bennetts and Hoskins 1979; see section 1.2.3.5 for a further literature review).

4.4 Recommendations to the Forecaster

Now that all of the results of this research have been discussed, what is a forecaster to do with this information? First, once an area of snow is forecast, the forecaster might create cross sections with EPV* similar to those in this thesis. These cross sections through the precipitation should be perpendicular to the 1000–500 hPa thickness contours at various locations, which can be easily accomplished in the National Weather Service's Advanced Weather Information Processing System (AWIPS) by sliding a cross section slice around the display screen (D. Nicosia 2006, personal communication). It is important to make sure that the slice is long enough to capture the entire area of frontogenesis.

Next, representative cross sections could be compared to the conceptual models in Figs. 4.4a–e to determine which mode or modes are forecast to occur in the precipitation region. An alternative to the conceptual models is the simple flowchart presented in Fig. 4.5 that can be followed to determine the precipitation mode. The forecaster could examine the frontogenesis pattern and look for regions of CI. There is no need to worry about the value of EPV* except that WMSS (0–0.25 PVU) is present. The forecaster could also observe how the cross sections evolve over time, as multiple modes can exist throughout the lifetime of a heavy snow event. Lastly, if the cross sections indicate the possibility of a "classic band," then the cross sections should be recreated using EPV^{*}_{g} instead of EPV* to locate the position of the forecasted band.

(a)

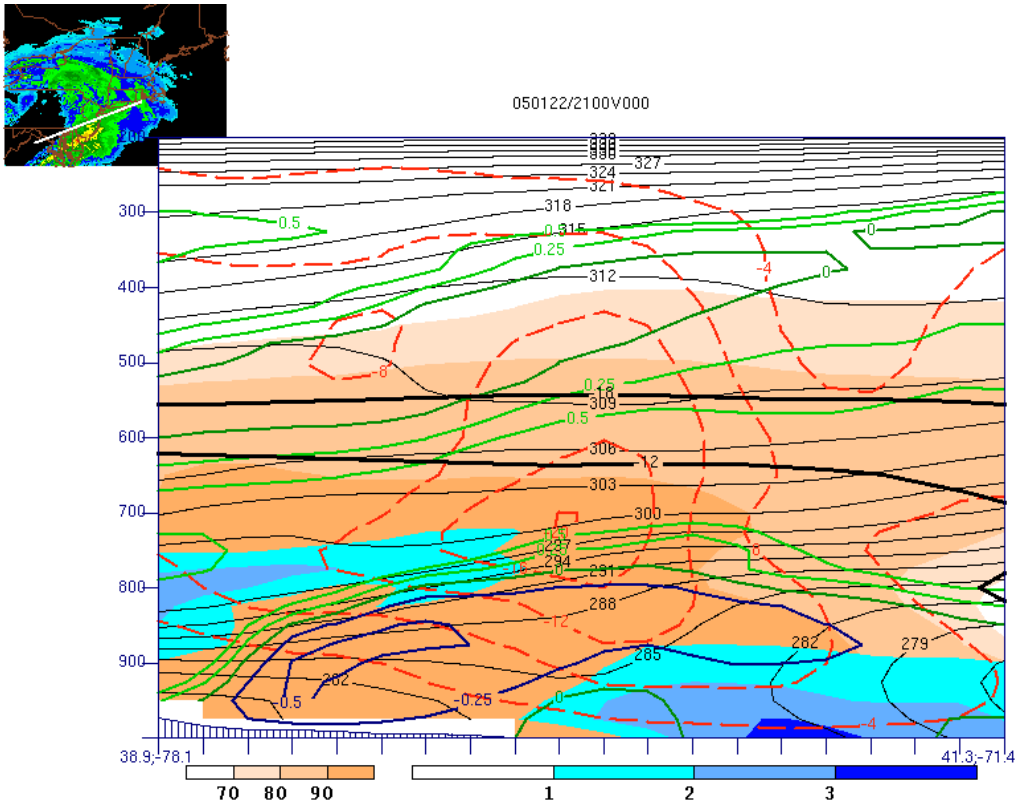

(b)

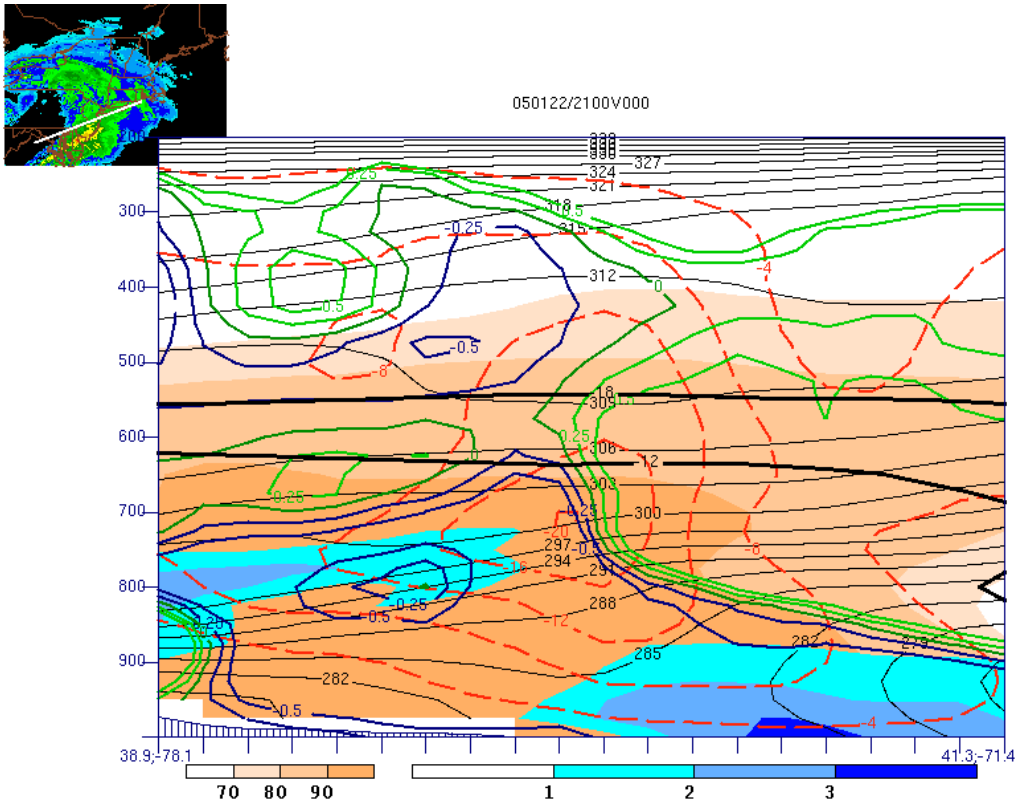

Fig. 4.1. (a–b) Same as Fig. 3.13 except with a different cross section slice.

(a)

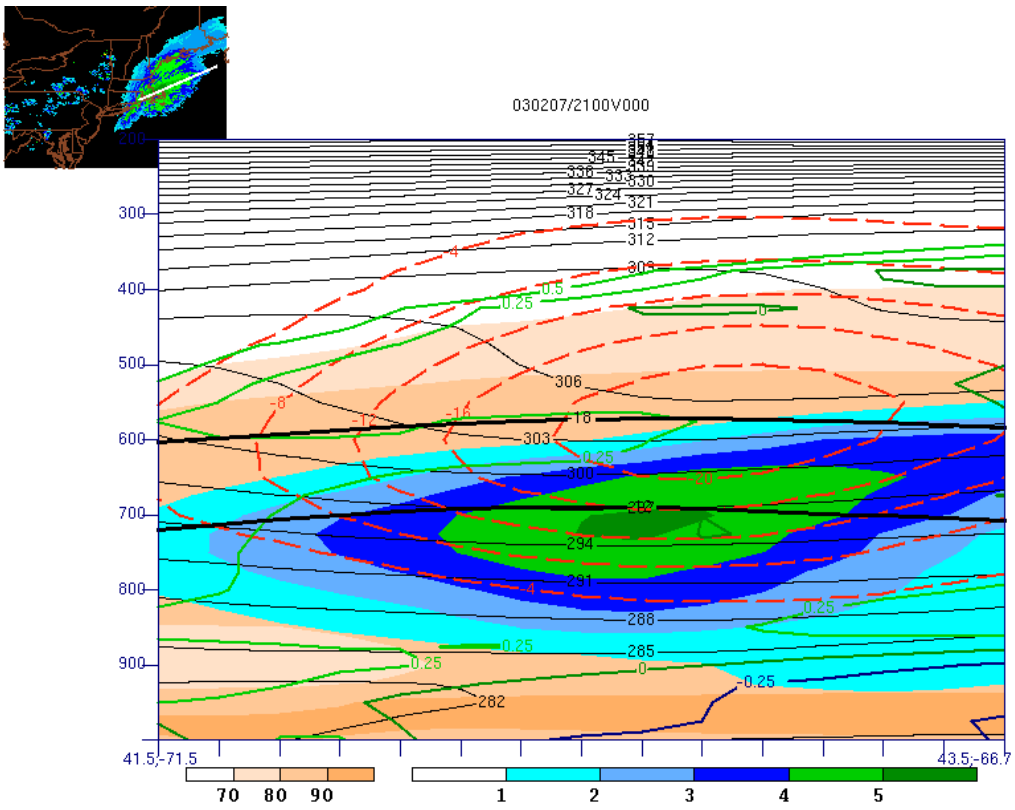

(b)

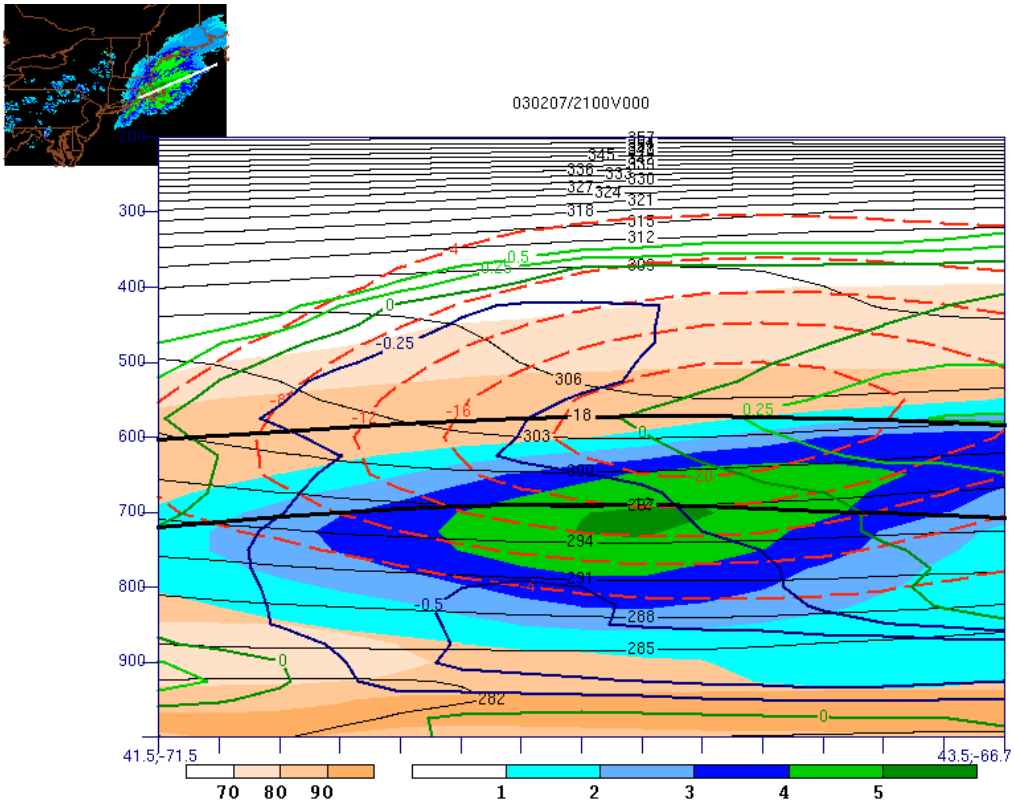

Fig. 4.2. (a–b) Same as Fig. 3.12 except with a different cross section slice.

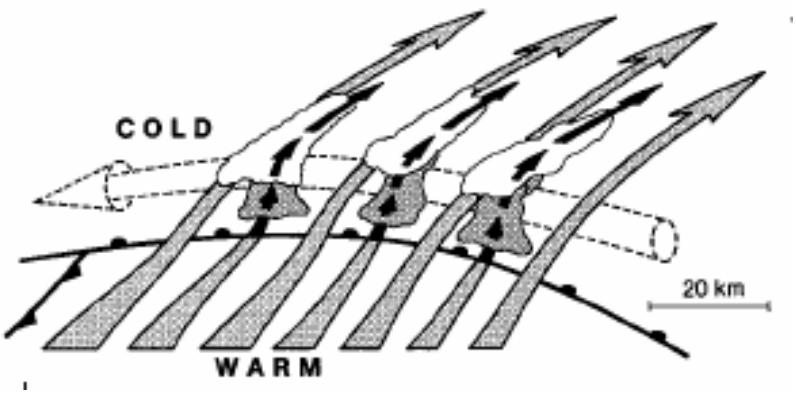

Fig. 4.3. Schematic of the "escalator–elevator" pattern of warm-frontal ascent. The warm conveyor belt (light gray arrows) rises over the cold conveyor belt (tubular dashed arrow). Mesoconvective ascent (the "elevator," black arrows) and accompanying convective clouds (dark gray shading with white anvils) are shown between regions of upglide ascent (the "escalator") [From Neiman et al. (1993)].

(a)

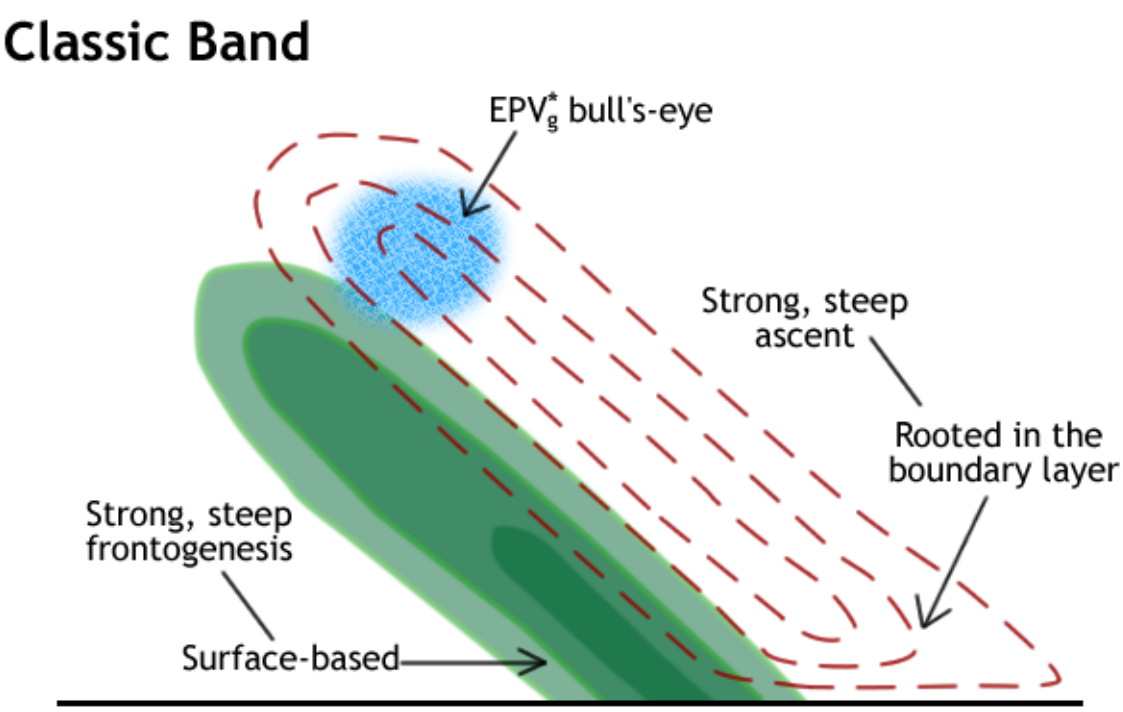

(b)

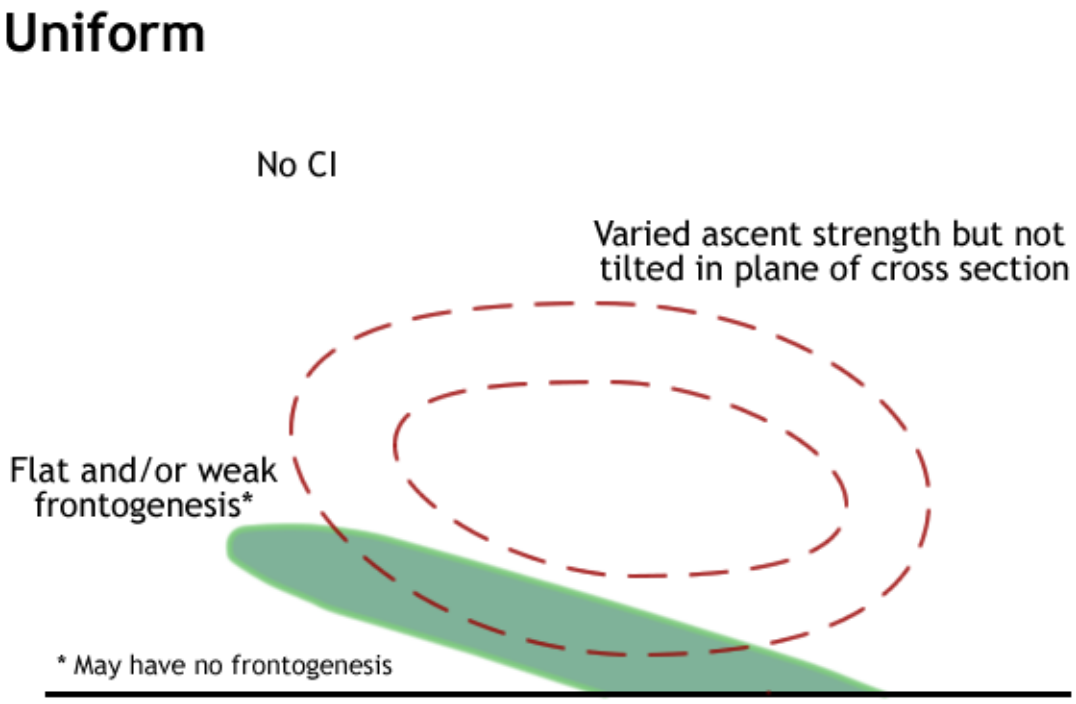

Fig. 4.4. (a–e) Schematic cross sections in the *x*–*p* plane for the five modes. Fields shown are frontogenesis (green shading), ascent (dashed), EPV^*_g bull's-eyes (light blue shading), and CI (purple shading). Cross-section length is approximately 600 km. Cross-section vertical axis is 1000–300 hPa.

(c)

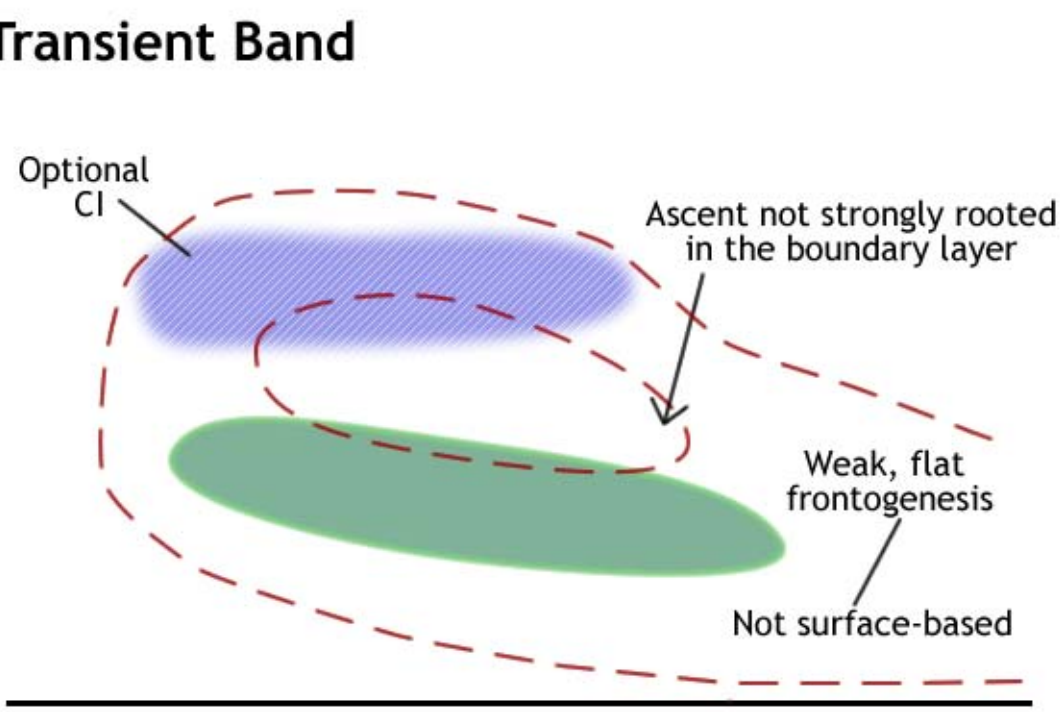

(d)

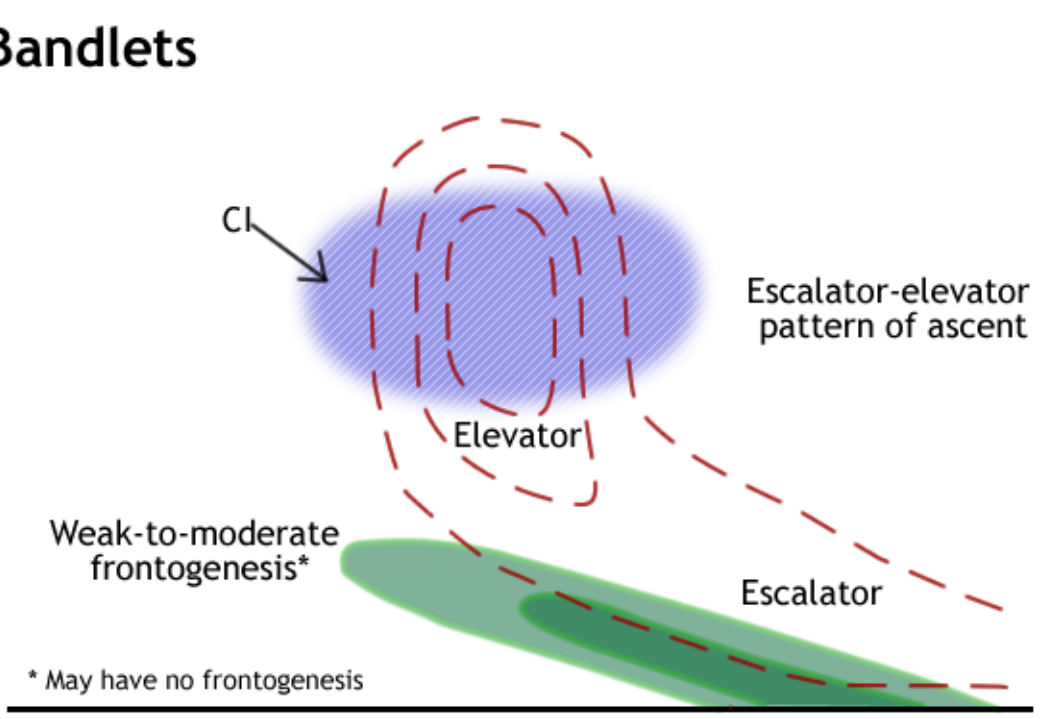

Fig. 4.4. (*Continued*)

(e)

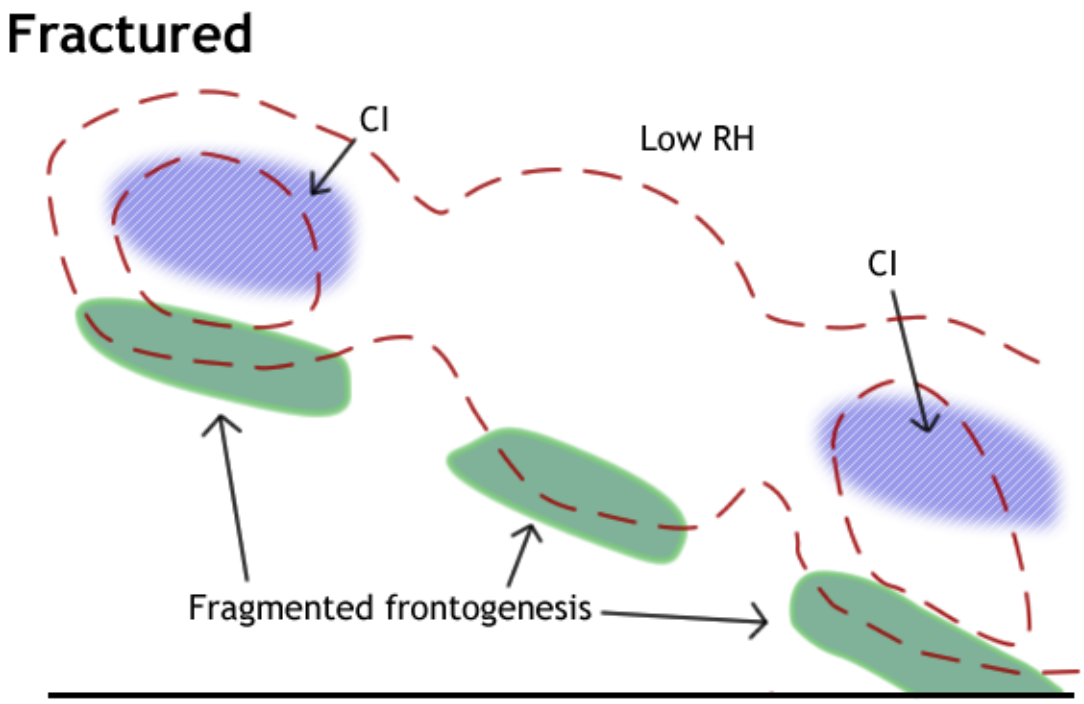

Fig. 4.4. (*Continued*)

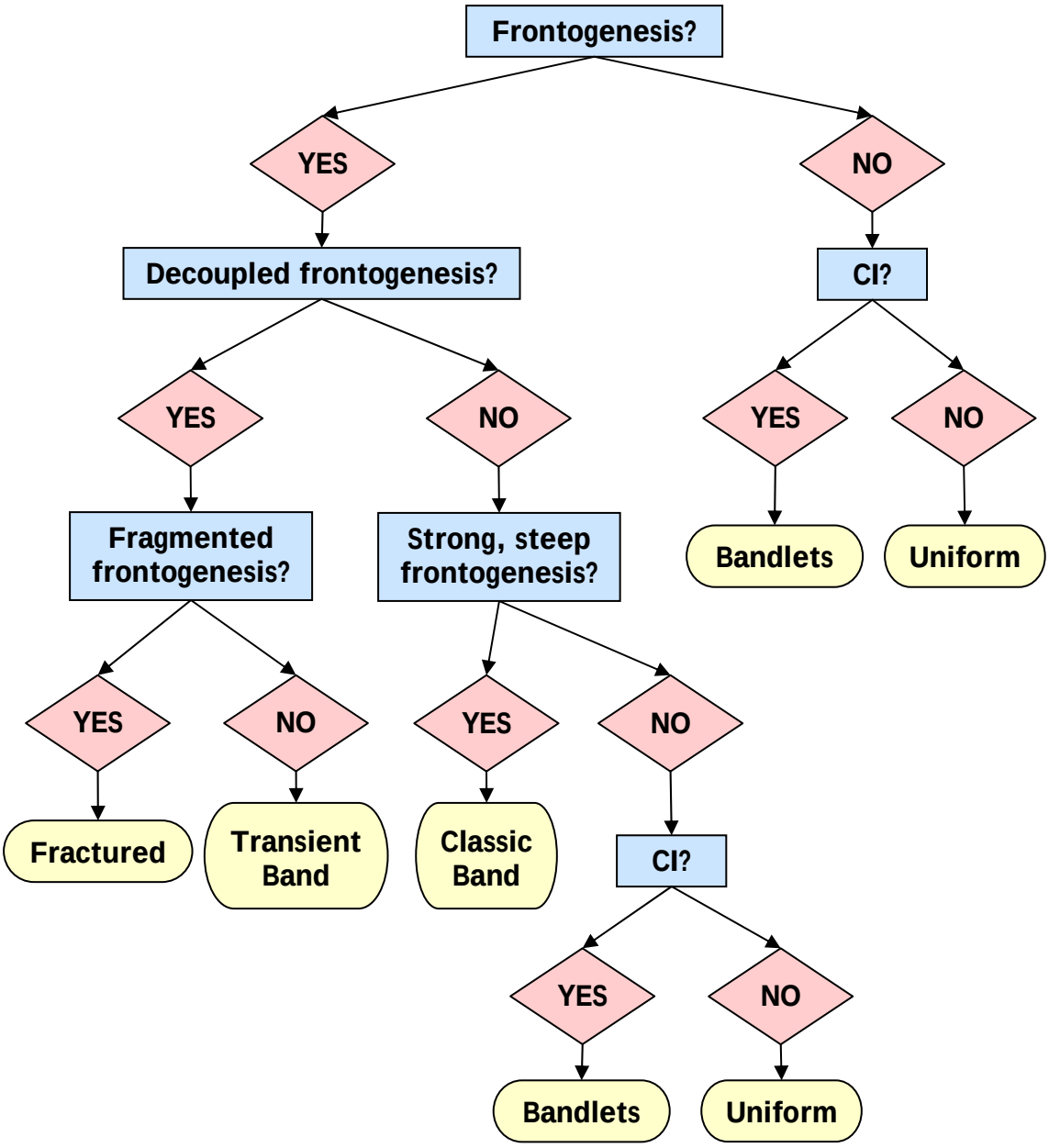

Fig. 4.5. Flowchart for forecasting snow modes during Northeast snowstorms.

5. Conclusions and Future Work

5.1 Conclusions

In this study, 20 northeastern U.S. snowstorm cases are examined in order to ascertain ways of distinguishing the different precipitation modes, or patterns, observed in the cases. Before radar imagery is examined, attempts are made to classify the 20 cases synoptically. Next, an analysis of WSI NOWrad reflectivity mosaics for the 20 cases reveals five precipitation modes: "uniform," "classic band," "transient band," "bandlets," and "fractured." "Uniform" cases feature homogeneous areas of precipitation. "Classic band" cases feature linearly organized, temporally coherent enhanced radar reflectivity areas. "Transient band" cases feature temporally incoherent, quasi-linearly organized enhanced areas of reflectivity. "Bandlets" cases feature small linear or elliptical filaments of enhanced reflectivity within a main precipitation shield. "Fractured" cases feature broken areas of precipitation with very light snows adjacent to heavier snows. This last mode is a low-impact snow, i.e., the "heavy snow" criteria of 15+ cm of snow in 6 h is met, but because of breaks in the snow, roads can be cleared and other precautions can be taken before heavier snows set in again. Lastly, a number of precipitation patterns are deemed unclassifiable (section 3.2.2; Table III) due to their hybrid or singular patterns.

To find parameters that could distinguish the modes, a plan-view approach is first taken in hopes of finding a more streamlined alternative to cross-section analyses, which are time-consuming during real-time forecasting. Using the 32-km North American Regional Reanalysis (NARR), several quantities are plotted in plan view, e.g., a ratio of QG forcings, the maximum vertical speed shear, and the depth of reduced saturation

equivalent potential vorticity (EPV*) layers satisfying EPV*, relative humidity, and ascent criteria (section 2.2.4). Unfortunately, no correlation is found between the numerous plan-view parameters and the modes.

Due to the lack of success with the plan-view approach, a cross-section analysis is undertaken. NARR cross sections are created perpendicular to thickness contours for multiple slices at numerous times throughout the heavy snow periods. The cross sections feature the four main ingredients—lift, instability, moisture, and microphysics—discussed in Chapter 1. Frontogenesis and vertical velocity represent lift; EPV* (calculated using both the full wind and geostrophic wind formulations) and θ_e^* assess the stability; relative humidity measures the moisture; and the −12°C and −18°C isotherms designate the bounds of the dendritic growth zone, which is important for the final ingredient, microphysics. From these cross sections, 40 representative members are selected for further analysis.

The results of the cross-section analysis are summarized by the conceptual models (Figs. 4.4a–e) in the previous chapter. "Uniform" cases feature flat and/or weak frontogenesis, limiting the vertical extent and intensity of the associated frontogenetical circulation. Strong lift can occur without frontogenesis, but it is not tilted in the plane of the cross section. Additionally, no CI is present to disturb the homogeneous precipitation shield. "Classic bands" feature strong, steep, surface-based frontogenesis, which induces strong, steep ascent rooted in the boundary layer. An EPV_g^* "bull's-eye" along a sloping frontal zone fortuitously reveals the surface position of a band. "Transient bands" feature frontogenesis decoupled from the surface, resulting in ascent not based in the boundary layer. This configuration inhibits the continuous supply of rich boundary-layer moisture

from entering the precipitation region. CI can further alter the precipitation pattern through the addition of mesoconvective circulations with enhanced updrafts and downdrafts. "Bandlets" cases feature the "escalator–elevator" pattern of ascent where frontogenetically forced slantwise ascent (the "escalator") transports air parcels to the level of free convection of a region of upright convection (the "elevator") associated with CI. Lastly, "fractured" cases feature fragmented areas of frontogenesis with coupled areas of reduced stability and enhanced ascent, possibly corresponding to the regions of enhanced radar reflectivity.

Overall, it appears that distinguishing these five precipitation modes can be reduced to aspects of the ingredients of lift and instability. An examination of frontogenesis and the existence of CI readily reveals the precipitation modes (see flowchart, Fig. 4.5). Most noticeably absent from this discussion is the role of varying degrees of reduced EPV*. It appears that the value, depth, and pattern of weak moist symmetric stability (WMSS) and negative EPV* play no role in determining the mode, except that their mere existence favors heavy snowfall, as revealed by the reduced EPV* in all of the cases in this study.

The operational knowledge base of mesoscale precipitation structures is now enhanced by this research through an ingredients-based discussion of five modes of precipitation during northeastern U.S. snowstorms. An examination of forecasted frontogenesis characteristics and conditional instability can now be applied not only to the prediction of previously studied banded structures but also to the prediction of even smaller-scale convective patterns, i.e., "bandlets," and to the prediction of low-impact "fractured" snows. Forecasters might also be able to utilize the included set of

conceptual models and flowchart to exploit the results of this research to improve their snowstorm forecasts.

5.2 Future Work

While the results of this research can now be applied in a real-time setting, there are still a number of issues that demand explanation or require further exploration:

1) The "fractured" mode should be further investigated to see if it is really just a hybrid of "transient bands" and a larger-scale form of "bandlets" but with drier spaces.
2) The hypothesis that decoupled frontogenesis disturbs the pipeline of moisture into a precipitation region needs to be further explored.
3) It is observed that some "uniform" and "bandlets" examples that have "classic band"-like cross sections develop into "classic bands" 3–9 h later. Thus, a possible time lag between a "classic band" cross section and a "classic band" appearing in radar imagery needs to be investigated.
4) The reasons for the existence of EPV_g^* "bull's-eyes" that are co-located with the surface position of bands needs to be studied.
5) The role of orography is essentially ignored in this study and may need to be looked at as a precipitation-organizing mechanism.
6) It would be interesting to redo this study with a much higher-resolution dataset to find out if the effects of CSI and CI can be better resolved. Also, the frontogenesis and instability characteristics discussed in this thesis

could be applied to a high-resolution model to see if the resulting forecasted precipitation modes agree with the findings of this thesis.

REFERENCES

Bennetts, D. A., and B. J. Hoskins, 1979: Conditional symmetric instability—A possible explanation for frontal rainbands. *Quart. J. Roy. Meteor. Soc.,* **105,** 945–962.

———, and J. C. Sharp, 1982: The relevance of conditional symmetric instability to the prediction of mesoscale frontal rainbands. *Quart. J. Roy. Meteor. Soc.,* **108,** 595–602.

Bluestein, H. B., 1992: *Synoptic-Dynamic Meteorology in Midlatitudes.* Vol. 1, *Principles of Kinematics and Dynamics.* Oxford University Press, 431 pp.

———, 1993: *Synoptic-Dynamic Meteorology in Midlatitudes*. Vol. 2, *Observations and Theory of Weather Systems*. Oxford University Press, 594 pp.

Bohren, C. F., and B. A. Albrecht, 1998: *Atmospheric Thermodynamics,* Oxford University Press, 416 pp.

Byrd, G. P., 1989: A composite analysis of winter season overrunning precipitation bands over the Southern Plains of the United States. *J. Atmos. Sci.,* **46,** 1119–1132.

Carbone, R. E., J. D. Tuttle, D. A. Ahijevych, and S. B. Trier, 2002: Inferences of predictability associated with warm season precipitation episodes. *J. Atmos. Sci.,* **59,** 2033–2056.

Carlson, T. N., 1998: *Mid-Latitude Weather Systems,* Amer. Meteor. Soc., 507 pp.

Charney, J. G., and A. Eliassen, 1964: On the growth of the hurricane depression. *J. Atmos. Sci.,* **21,** 68–75.

Clark, J. H. E., R. P. James, and R. H. Grumm, 2002: A reexamination of the mechanisms responsible for banded precipitation. *Mon. Wea. Rev.,* **12,** 3074–3086.

Colman, B. R., 1990: Thunderstorms above frontal surfaces in environments without positive CAPE. Part II: Organization and instability mechanisms. *Mon. Wea. Rev.*, **118,** 1123–1144.

desJardins, M. L., K. F. Brill, and S. S. Schotz, 1991: Use of GEMPAK on UNIX workstations. *Proc. Seventh Int. Conf. On Interactive Information and Processing Systems for Meteorology, Oceanography, and Hydrology,* New Orleans, LA, Amer. Meteor. Soc., 449–453.

Doswell, C. A., III, 1987: The distinction between large-scale and mesoscale contribution to severe convection: A case study example. *Wea. Forecasting,* **2,** 3–16.

Emanuel, K. A., 1985: Frontal circulations in the presence of small moist symmetric instability. *J. Atmos. Sci.*, **42,** 1062–1071.

Evans, M., 2006: An analysis of a frontogenetically forced early-spring snowstorm. *Bull. Amer. Meteor.,* **87,** 27–32.

Gray, S. L., and A. J. Thorpe, 2001: Parcel theory in three dimensions and the calculations of SCAPE. *Mon. Wea. Rev.,* **129,** 1656–1672.

Hane, C.E., 1986: Extratropical squall lines and rainbands. *Mesoscale Meteorology and Forecasting*, P.S. Ray, Ed., Amer. Meteor. Soc., 359–389.

Hoskins, B. J., 1974: The role of potential vorticity in symmetric stability and instability. *Quart. J. Roy. Meteor. Soc.,* **100,** 480–482.

———, I. Draghici, and H. Davies, 1978: A new look at the ω-equation. *Quart. J. Roy. Meteor. Soc*., **104,** 31–38.

Jascourt, S. D., S. S. Lindstrom, C. J. Seman, and D. D. Houghton, 1988: An observation of banded convective development in the presence of weak symmetric stability. *Mon. Wea. Rev.,* **116,** 175–191.

Jurewicz, M. L., Sr., and M. S. Evans, 2004: A comparison of two banded, heavy snowstorms with very different synoptic settings. *Wea. Forecasting,* **19,** 1011–1028.

Kalnay, E., and Coauthors, 1996: The NCEP/NCAR 40-year reanalysis project. *Bull. Amer. Meteor. Soc.*, **77,** 437–471.

Kistler, R., and Coauthors, 2001: The NCEP/NCAR 50-Year reanalysis: Monthly means CD-ROM and documentation. *Bull. Amer. Meteor. Soc.,* **82,** 247–267.

Kocin, P. J., and L.W. Uccellini, 2004: *Overview*. Vol. 1. *Northeast Snowstorms*. No. 54, Amer. Meteor. Soc., 296 pp.

Loughe, A. F., C. Lai, and D. Keyser, 1995: A technique for diagnosing three-dimensional ageostrophic circulations in baroclinic disturbances on limited-area domains. *Mon. Wea. Rev.,* **123,** 1476–1504.

Martin, J. E., 1998: The structure and evolution of a continental winter cyclone. Part II: Frontal forcing of an extreme snow event. *Mon. Wea. Rev.,* **126,** 329–348.

McCann, D. W., 1995: Three-dimensional computations of equivalent potential vorticity. *Wea. Forecasting,* **10,** 798–802.

McNulty, R. P., 1978: On upper tropospheric kinematics and severe weather occurrence. *Mon. Wea. Rev.,* **106,** 662–672.

Mesinger, F., and Coauthors, 2006: North American Regional Reanalysis. *Bull. Amer. Meteor. Soc.,* **87,** 343–360.

Miller, J. E., 1948: On the concept of frontogenesis. *J. Atmos. Sci.,* **5,** 169–171.

Moore, J. T., and T. E. Lambert, 1993: The use of equivalent potential vorticity to diagnose regions of conditional symmetric instability. *Wea. Forecasting,* **8,** 301–308.

Neiman, P. J., and M. A. Shapiro, 1993: The life cycle of an extratropical marine cyclone. Part I: Frontal-cyclone evolution and thermodynamic air-sea interaction. *Mon. Wea. Rev.,* **121,** 2153–2176.

———, ———, and L. S. Fedor, 1993: The life cycle of an extratropical marine cyclone. Part II: Mesoscale structure and diagnostics. *Mon. Wea. Rev.,* **121,** 2177–2199.

Nicosia, D. J., and R. H. Grumm, 1999: Mesoscale band formation in three major northeastern United States snowstorms. *Wea. Forecasting,* **14,** 346–368.

Novak, D. R., L. F. Bosart, D. Keyser, and J. S. Waldstreicher, 2004: An observational study of cold season-banded precipitation in northeast U.S. cyclones. *Wea. Forecasting,* **19,** 993–1010.

———, J. S. Waldstreicher, L. F. Bosart, D. Keyser, 2006: A forecast strategy for anticipating cold season mesoscale band formation within eastern U.S. cyclones. *Wea. Forecasting,* **21,** 3–23.

O'Handley, C., and L. F. Bosart, 1989: Subsynoptic-scale structure in a major synoptic-scale cyclone. *Mon. Wea. Rev.,* **117,** 607–630.

Orlanski, I., 1975: A rational subdivision of scales for atmospheric processes. *Bull. Amer. Meteor. Soc.,* **56,** 527–530.

Persson, P. O. G., and T. T. Warner, 1995: The nonlinear evolution of idealized, unforced, conditional symmetric instability: A numerical study. *J. Atmos. Sci.,* **52,** 3449–3474.

Petterssen, S., 1956: *Weather Analysis and Forecasting.* Vol. 1, McGraw-Hill, 428 pp.

Power, B. A., P. W. Summers, and J. d'Auignon, 1964: Snow crystal forms and riming effects as related to snowfall density and general storm conditions. *J. Atmos. Sci.,* **21,** 300–305.

Reuter, G. W., and N. Aktary, 1995: Convective and symmetric instabilities and their effects on precipitation: Seasonal variations in central Alberta during 1990 and 1991. *Mon. Wea. Rev.,* **123,** 153–162.

Roebber, P. J., S. L. Bruening, D. M. Schultz, and J. V. Cortinas Jr., 2003: Improving snowfall forecasting by diagnosing snow density. *Wea. Forecasting,* **18,** 264–287.

Sanders, F., and L. F. Bosart, 1985: Mesoscale structure in the Megalopolitan snowstorm of 11–12 February 1983. Part I: Frontogenetical forcing and symmetric instability. *J. Atmos. Sci.,* **42,** 1050–1061.

Schultz, D. M., D. Keyser, L. F. Bosart, 1998: The effect of large-scale flow on the low-level frontal structure and evolution in midlatitude cyclones. *Mon. Wea. Rev.,* **126,** 1767–1791.

———, and P. N. Schumacher, 1999: The use and misuse of conditional symmetric instability. *Mon. Wea. Rev.,* **127,** 2709–2732.

———, ———, and C. A. Doswell III, 2000: The intricacies of instabilities. *Mon. Wea. Rev.,* **128,** 4143–4148.

Seltzer, M. A., R. E. Passarelli, and K. A. Emanuel, 1985: The possible role of symmetric instability in the formation of precipitation bands. *J. Atmos. Sci.,* **42,** 2207–2219.

Shapiro, M. A., E. G. Donall, P. J. Neiman, L.S. Fedor, and F. Gonzalez, 1991: Refinements in the conceptual models of extratropical cyclones. Preprints, *First International Winter Storm Symp.,* New Orleans, LA, Amer. Meteor. Soc., 6–13.

Shutts, G. J., 1990: SCAPE Charts from Numerical Weather Prediction Model Fields. *Mon. Wea. Rev.,* **12**, 2745–2751.

Thorpe, A. J., and K. A. Emanuel, 1985: Frontogenesis in the presence of small stability to slantwise convection. *J. Atmos. Sci.,* **42,** 1809–1824.

Waldstreicher, J.S., 2001: The importance of snow microphysics for large snowfalls. Preprints, 3rd Northeast Region Operational Workshop, Albany, NY, NOAA/NWS, 17.

Weisman, M. L., and J. B. Klemp, 1982: The dependence on numerically simulated convective storms on vertical wind shear and buoyancy. *Mon. Wea. Rev.,* **6,** 504–520.

Wetzel, S. W., and J. E. Martin, 2001: An operational ingredients-based methodology for forecasting midlatitude winter season precipitation. *Wea. Forecasting.,* **16,** 156–167.

Xu, Q., 1986: Conditional symmetric instability and mesoscale rainbands. *Quart. J. Roy. Meteor. Soc.,* **112,** 315–334.

———, 1992: Formation and evolution of frontal rainbands and geostrophic potential vorticity anomalies. *J. Atmos. Sci.,* **49,** 629–648.